EXPERIMENTAL INVESTIGATION OF ROTORDYNAMIC INSTABILITIES CAUSED BY ROTOR BLADE-TIP EXCITATION FORCES

by

Douglas H. Loose

B.S. Mechanical Engineering,
The Pennsylvania State University (May 1987)

SUBMITTED TO THE DEPARTMENT OF AERONAUTICS AND ASTRONAUTICS
IN PARTIAL FULLFILMENT OF THE REQUIREMENTS FOR
THE DEGREE OF

MASTER OF SCIENCE IN
AERONAUTICS AND ASTRONAUTICS

at the

MASSACHUSETTS INSTITUTE OF TECHNOLOGY

August 1989

Signature of Author_____
Department of Aeronautics and Astronautics
August 1989

Certified by_____
Dr. Belgacem Jery
Assistant Professor of Aeronautics and Astronautics
Thesis supervisor

Approved by_____
Professor Harold Y. Wachman
Chairman, Department Graduate Committee

EXPERIMENTAL INVESTIGATION OF ROTORDYNAMIC INSTABILITIES CAUSED BY ROTOR BLADE-TIP EXCITATION FORCES

by

Douglas H. Loose

Submitted to the Department of Aeronautics and Astronautics in August 1989,
in partial fulfillment of the requirements for the degree of
Master of Science in Aeronautics and Astronautics

ABSTRACT

A facility was designed and constructed to experimentally investigate lateral destabilizing aeroelastic forces in turbines which are generated when the rotor is not concentric with the casing, with emphasis on the cross-coupled force. The facility is a closed loop with Freon-12 as the working gas. The test turbine is a 1:1 replica of the Space Shuttle main engine fuel turbopump first stage. Through a specially designed bearing support the rotor can be moved laterally, statically or dynamically, while the casing remains stationary, thus simulating an eccentric or whirling rotor.

The test turbine is heavily instrumented to enable detailed measurements of the effects of rotor eccentricity. The lateral forces acting on the rotor are measured through the use of a unique rotating dynamometer. The dynamometer is attached directly to the rotor and has the capability of measuring all components of force and moment acting on the rotor. The turbine casing is designed with numerous provisions for pressure and temperature measurements, the highest concentration being in the rotor blade-tip region, to enable detailed flow measurements. The turbine casing is also rotatable so that azimuthal distribution of flow variables may be obtained.

Lateral rotor force measurements were made at various operating conditions and amounts of rotor offset. The cross-coupled forces measured were directly proportional to the amount of eccentricity with the constant of proportionality ranging from 0 to 1.9 depending on the turbine operating point. Azimuthal distributions of the static pressure at the blade-tip region were measured for various amounts of rotor offset. The pressure was found to vary sinusoidally with amplitude directly proportional to the amount of eccentricity.

Thesis supervisor: Dr. Belgacem Jery.
Assistant Professor of Aeronautics and Astronautics.

ACKNOWLEDGEMENTS

The efforts of many people went into the design, construction and running of the Alford force test facility and without their help the facility would not be where it is today. To the following people I would like express my thanks:

Professors Belgacem Jery and Manual Martinez-Sanchez for their guidance and advice throughout every phase of the project.

Mr. Roy Andrew, Mr. Victor Dubrowski and Mr. Jim Nash for their technical support in the lab.

Mr. Seung-Jin Song for working long hours and weekends to get things done (and good luck in his continuance of this project).

Dr. Kiran Magiawala, Mr. Yuan Qiu and Mr. Bob Gauthier for their help in design and construction.

Mr. Victor Filipenco and Mr. Knox Millsaps for their helpful technical advice and for "giving a hand" in the lab.

And finally to all family and friends for their support.

This project was funded by NASA, George C. Marshall Flight Center under contract number NAS8-35018. Also, my personal support during the project was through an AFRAPT Traineeship in conjunction with Pratt & Whitney Aircraft, W. Palm Beach, FL.

TABLE OF CONTENTS

LIST OF FIGURES

LIST OF TABLES

NOMENCLATURE

Symbols

A_1, A_2	Constant in differential equation solution
[B]	Six-by-six dynamometer calibration matrix
c	Rotor damping coefficient
C_{xx}, C_{yy}, C_{xy}, C_{yx}	Damping coefficients of rotor due to fluid effects
d_n, d_l	Stator and rotor seal diameter, respectively
D_m, d_m	Mean rotor diameter
e	Rotor eccentricity
f	Lateral rotor force per radian
F	Resultant steady lateral rotor force vector
$\overline{F}$	Magnitude of resultant steady lateral rotor force
F_1, F_2	Total lateral rotor force measured in rotating reference frame
F_x, F_y	Total lateral rotor force measured in inertial reference frame
$\overline{F}_x$, $\overline{F}_y$	Average total lateral rotor force measured in inertial frame
F_x^P, F_y^P	Lateral rotor force due to azimuthal static pressure variations
F_{id}	Total ideal azimuthal force (torque/radius)
{f}	Six-component generalized rotor force vector
H	Rotor blade height
k	Rotor shaft stiffness
K_{xx}, K_{yy}, K_{xy}, K_{yx}	Stiffness coefficients of rotor due to fluid effects
k_2	Thomas' excitation coefficient ($k_{2d} + k_{2s}$)
k_{2d}	Excitation coefficient due to blade-tip clearance variation
k_{2s}	Excitation coefficient due to azimuthal pressure variation
k', k"	Excitation coefficient correlation experimental factors
l', l"	Blade heights of stator and rotor, respectively
M_{air}	Molecular weight of air
M_{Freon}	Molecular weight of Freon-12
m	Mass of rotor shaft

n	Numerical factor, integer between 1 and 32
P	Azimuthal static pressure
R	Radius
R_i	Rotor hub radius
R_o	Rotor outer radius
s	Blade-tip clearance of concentric turbine
$[S]$	Six-by-six dynamometer strain gauge bridge slope matrix
t	Time
T	Total rotor torque
$\{V\}$	Six-component dynamometer strain gauge bridge voltage vector
X	Inertial coordinate axis parallel to eccentricity axis
Y	Inertial coordinate axis perpendicular to eccentricity axis
y_{air}	Mole fraction of air in the flow loop
y_{Freon}	Mole fraction of Freon-12 in the flow loop
z', z''	Number of seal strips on stator and rotor
α	Factor dependant on turbine geometry and operating point
α_1	Stator leaving angle
β	Alford factor ($2k_2$)
β_2	Rotor leaving angle
δ	Local rotor blade-tip clearance
δ_m	Mean or concentric turbine blade-tip clearance
ϕ	Angle between X-axis and F_1-axis at $t = 0$
η	Local efficiency
η_m	Mean or concentric turbine efficiency
η_o	Ideal or zero blade-tip clearance efficiency
λ	Complex eigenvalue in differential equation solution ($\sigma + i\omega_d$)
θ	Angle in inertial reference frame measured from positive X-axis
σ	Damping exponent
τ	Local rotor torque per radian
τ_m	Mean or concentric turbine torque per radian
ω_d	Damped natural frequency (rad/s)
ω_r	Rotor rotational frequency (rad/s)

ψ	Angle measured from F_1 axis position at $t = 0$ ($\omega_r t$)
ζ	Damping ratio

Subscripts

m	Mean or concentric turbine value
x	Direction parallel to eccentricity axis
y	Direction perpendicular to eccentricity axis

CHAPTER 1

INTRODUCTION

1.1 Statement of the Problem

One trend in the design of turbomachinery today is increasing power density (see figure 1.1). Designers today are constantly faced with the challenge to design higher powered turbomachines while making them as light and compact as possible. This is especially true in many aerospace applications where performance often depends on high power and low weight. One characteristic of this trend, however, is the increased problem of rotordynamic instabilities. Unfortunately, in many cases the designer has no way of foreseeing these problems and they are therefore not discovered until prototype or even final testing.

A recent example is the Space Shuttle main engine (SSME) high pressure fuel turbopump (HPFTP) and high pressure oxidizer turbopump (HPOTP). The HPOTP produces nearly 22,000 kW (29,500 hp) at 30,400 rpm while the HPFTP produces an incredible 57,525 kW (77,142 hp) at 37,076 rpm at full power level (FPL) both through two 0.28 m (11 in.) diameter stages. Each of the 63 rotor blades per stage of the HPFTP absorbs 457 kW (612 hp) which makes the HPFTP power-to-weight undoubtedly the highest of any turbomachine ever built. Both of these high power density turbomachines suffered from vibration problems which were not discovered until initial engine tests. Development was delayed for six months at an estimated cost of $500,000 a day [4].

Rotordynamic instabilities are usually in the form of rotor whirl which is the precession of a rotating shaft about the bearing centerline at unacceptable amplitudes. The whirling frequency generally is is nonsynchronous with the rotor speed, but is close to one critical speed. These instabilities are often what sets the upper operating limits of turbomachines.

Once a turbomachine encounters a rotordynamic instability it must be slowed down immediately, otherwise noise, vibration, excessive loads and alternating stresses, loss of performance, bearing and seal damage or possibly catastrophic failure could occur.

In practice, all turbomachines operate with some amount of rotor whirl. It is when the whirl becomes excessive that it becomes a problem. If the shaft is displaced slightly from equilibrium and the resulting forces cause it to move further away from equilibrium the system is unstable. This instability occurs very suddenly, most commonly when the rotor is operating at a speed somewhere between its first and second critical speeds. As the speed of the turbomachine is increased the amplitude of the instability increases rapidly. However, the frequency of the instability does not increase with rotor speed as a forced vibration would, but rather it is constant with and independent of rotor speed and in practice is often near the first critical speed of the shaft. This is termed subsynchronous whirl since the whirl frequency is lower than the shaft rotation frequency. If the whirling frequency is higher than the shaft rotation frequency it is supersynchronous and if the two frequencies are equal the whirl is said to be synchronous. A typical plot of forced and subsynchronous vibration response is shown in figure 1.2.

The primary source of rotordynamic instabilities is not rotor unbalance, since the centrifugal force of the unbalance rotates at shaft speed. Rather, most destabilizing excitations in turbomachinery originate from fluid interactions with the bearings, seals and rotor.

One convention which should be mentioned is the terminology for whirl direction. If the precession is in the same direction as rotor rotation it is referred to as forward whirl. If it is in the opposite direction of rotor rotation it is referred to as backward whirl.

1.2 Rotordynamic Instability

1.2.1 Mechanisms of Rotordynamic Instability

There are several destabilizing mechanisms which can potentially cause rotordynamic instability. Most of these mechanisms are understood quite well qualitatively, however attempts to quantify them have had limited success.

The main emphasis of this thesis is to experimentally quantify one of these destabilizing force mechanisms known as the Alford force (or Thomas force in European designation) which will be discussed in some detail in chapter two. The concept of the Alford force was introduced by H.J. Thomas [17] in Germany and independently by J.S. Alford [1] in the U.S. The Alford force is often thought to be the dominant destabilizing mechanism in axial flow turbomachinery. However, other mechanisms commonly coexist with the Alford force and should be mentioned briefly.

Hysteretic whirl is caused by a phase shift between the neutral stress axis and the neutral strain axis as a deflected shaft rotates. The resultant force has a component normal to the deflection in a direction which induces forward whirl and is therefore destabilizing. The tendency for hysteretic whirl is largely dependant on the hysteretic characteristic of the rotor which can be reduced by incorporating certain design considerations such as minimizing the number of separate elements which are held together by shrink fits [4].

Dry friction whip is caused by the rubbing of two unlubricated surfaces such as an inadvertent contact of a labyrinth seal. The frictional force between the two parts can contribute to excitation at speeds above the lowest critical. Therefore, contact between unlubricated surfaces must be avoided. Modern design and manufacturing procedures have nearly eliminated this destabilizing mechanism [4].

Hydrodynamic bearing whirl is caused by pressure forces generated by a deflected shaft rotating in a viscous fluid. The resultant pressure force will tend to further shaft deflection and induce forward whirl. And, under certain conditions of low damping the excitation force may

give rise to instability Modern bearing design has greatly reduced, but not eliminated this mechanism as a problem.[13].

Seal forces can also affect the stability of a system. A deflected shaft will cause a seal passage to have a non-uniform width and if the approaching fluid has some swirl, not equal to the surface speed of the seal, pressure perturbations will occur which can generate a resultant destabilizing force This destabilizing force is also affected by nominal pressure difference and seal clearance [2].

Again, the main emphasis of this thesis is the Alford force. Briefly, this destabilizing mechanism is due to a rotor not being perfectly concentric with the casing (see figure 1.3). A rotor which is slightly off-center will have a circumferential variation in blade-tip clearances. It is argued that the blades with smaller tip clearance will be locally more efficient because of less losses than blades with larger tip clearance. The blade forces will vary in approximately the same way as the local efficiency. The variation in blade forces results in a force acting on the rotor in a direction perpendicular to the direction the rotor is offset from the casing center line. The resultant force also acts in the direction of rotor rotation, therefore forward whirl is induced. The Alford force will be discussed in greater detail in chapter 2.

1.2.2 Stability Model

In order to determine the importance of lateral forces on the stability of a rotor it is necessary to model the system taking into account all important lateral forces. Using the analysis given by Vance [19] for a disk supported by a massless elastic shaft with stiffness k, the force components due to fluid effects can be written as,

$$F_x = -K_{xx}\, e_x - K_{xy}\, e_y - C_{xx}\, \dot{e}_x - C_{xy}\, \dot{e}_y$$

$$F_y = -K_{yx}\, e_x - K_{yy}\, e_y - C_{yx}\, \dot{e}_x - C_{yy}\, \dot{e}_y$$

where K_{ii} and C_{ii} are the direct stiffness and damping coefficients, respectively, which relate forces and displacements which are in the same direction. K_{ij} and C_{ij} are the cross-coupling stiffness and damping coefficients which relate a force in one direction to a displacement in the other.

It should be noted that the above equations for lateral force are simplified by not including any mass coefficients. In a paper by Childs and Moyer [3] it is shown that results of this model are greatly improved if mass terms are added. They calculated natural frequencies for the Space Shuttle main engine HPOTP using data from experiments at the California Institute of Technology [8]. They showed that if the mass terms were not included the calculated second natural frequency was (i) highly damped and (ii) predicted at a 20% higher frequency compared to calculations which included a mass term. It is their recommendation that the mass terms be included for all rotordynamic calculations.

Another simplification in the above model is that no non-linear terms are present. It will be shown in Chapter 5 that the direct and cross-coupled stiffness terms are quite linear, however often non-linear damping is present and may need to be included in the analysis.

Using the simplified model, the equations of motion can now be written in matrix form as,

$$\begin{bmatrix} m & 0 \\ 0 & m \end{bmatrix} \begin{Bmatrix} \ddot{e}_x \\ \ddot{e}_y \end{Bmatrix} + \begin{bmatrix} C_{xx} & C_{xy} \\ C_{yx} & C_{yy} \end{bmatrix} \begin{Bmatrix} \dot{e}_x \\ \dot{e}_y \end{Bmatrix} + \begin{bmatrix} k + K_{xx} & K_{xy} \\ K_{yx} & k + K_{yy} \end{bmatrix} \begin{Bmatrix} e_x \\ e_y \end{Bmatrix} = \begin{Bmatrix} 0 \\ 0 \end{Bmatrix}$$

where m is the apparent mass (mass of the rotor plus any fluid which is moved with the rotor) and k is the shaft stiffness.

The equations of motion are linear, homogeneous, coupled and have constant coefficients. Their general solution can be written as,

$$\begin{Bmatrix} e_x \\ e_y \end{Bmatrix} = \begin{Bmatrix} A_1 \\ A_2 \end{Bmatrix} \exp(\lambda t)$$

where λ is a complex eigenvalue and A_1, A_2 are determined by initial conditions. λ is expressed as $\lambda = \sigma + i\omega_d$ where σ is the damping exponent and ω_d is the damped natural frequency. The damping exponent, σ, is what determines the stability of the system, i.e. if $\sigma > 0$ the system will be unstable. Figure 1.4 shows how the damping exponent, σ, varies with cross-coupled stiffness for three values of the damping ratio, ζ, which is defined as,

$$\zeta = \frac{c}{2\sqrt{k\,m}}$$

where c is the sum of internal rotor damping and external fluid damping. Figure 1.4 demonstrates that unless a turbomachine has sufficient intrinsic damping or fluid damping an instability due to the cross-coupled stiffness, K_{xy}, instability will occur. It is for this reason that understanding the mechanisms of cross-coupled forces is so important.

1.3 Objectives

The objective of this thesis is to present the design of a facility which has been constructed and will enable detailed study of the Alford force and the flow parameters associated with it, and to present the operating characteristics of the facility including the measurement of the Alford forces generated for various degrees of rotor offset.

It has already been demonstrated in the case of the Space Shuttle HPFTP and HPOTP that as the power density of turbomachines increases, the problem of rotordynamic instabilities also increases. Although the Alford force may be an important factor in causing rotordynamic instability its concepts at this time are not well understood. The theoretical work of H.J. Thomas and J.S. Alford was published and accepted over 25 years ago. However, experimental verification has been limited. Designers today have very limited resources to help

them determine the effects the Alford force will have on the stability of the turbomachine while it is still on the drafting board. It is without question that there is a need to better understand the Alford force and its effect on rotordynamic instability.

It is for this purpose that a facility has been designed and constructed to study in detail the Alford force. The facility realistically models present operating turbomachines and allows measurement of forces generated due to rotor offset and also detailed flow mapping of the blade-tip and other pertinent regions. It is anticipated that experimental data from this facility will be used to better understand and accurately quantify Alford's and Thomas' concepts and that the results will be significant enough to allow development of a reliable method for designing and evaluating turbomachines with respect to the effects of the Alford force.

FACTORS INFLUENCING DESIGN CHANGE IN TURBOMACHINERY FOR ROCKET ENGINE APPLICATIONS

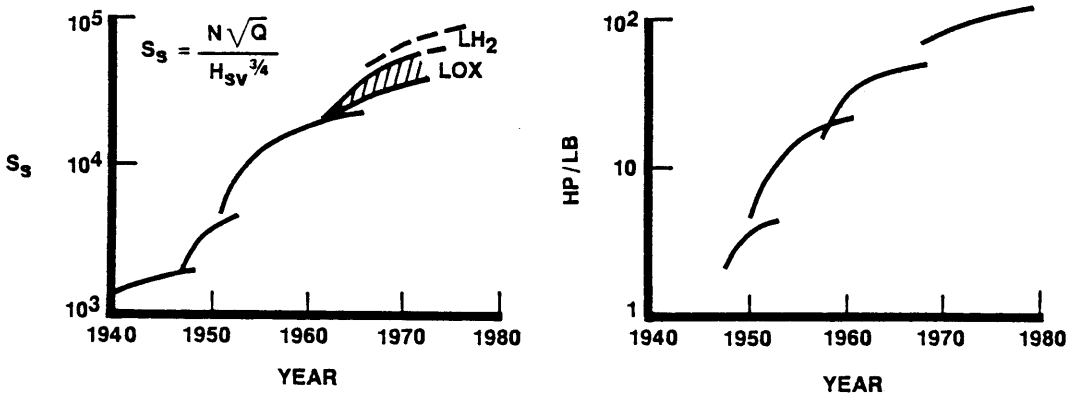

- TREND TOWARD HIGH P_C (SMALLER ENGINE/LB THRUST) PUSHED TURBOPUMP PRESSURES UPWARD
- ABILITY TO DEVELOP HIGH S_S ALLOWED HIGH SHAFT SPEED, SMALLER PUMPS
- HYDROGEN TECHNOLOGY REQUIRED EXTREME DEVELOPED HEAD

Fig. 1.1 Trend of increasing power density in modern turbomachines
Data source: Rocketdyne Division, Rockwell International

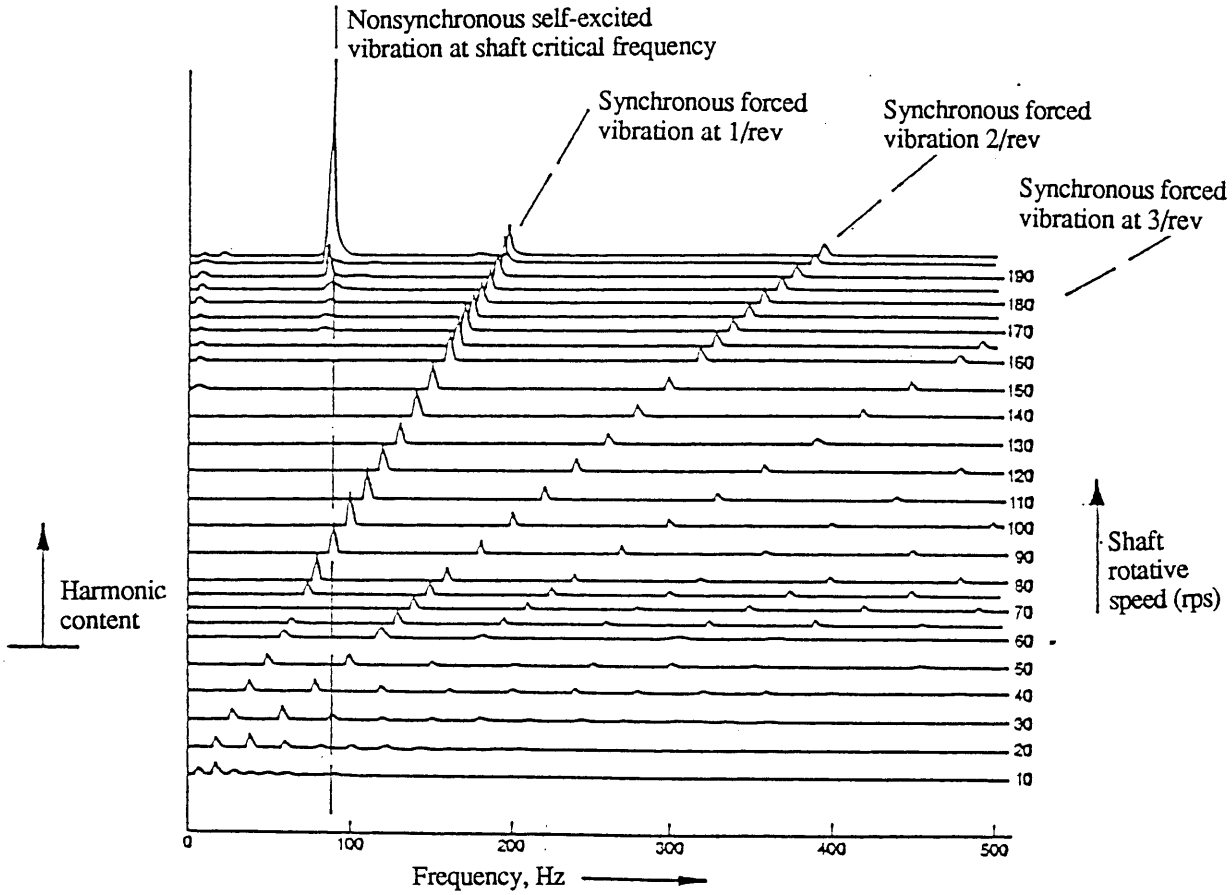

Fig. 1.2 Typical cascade plot showing forced and subsynchronous vibration response [5]

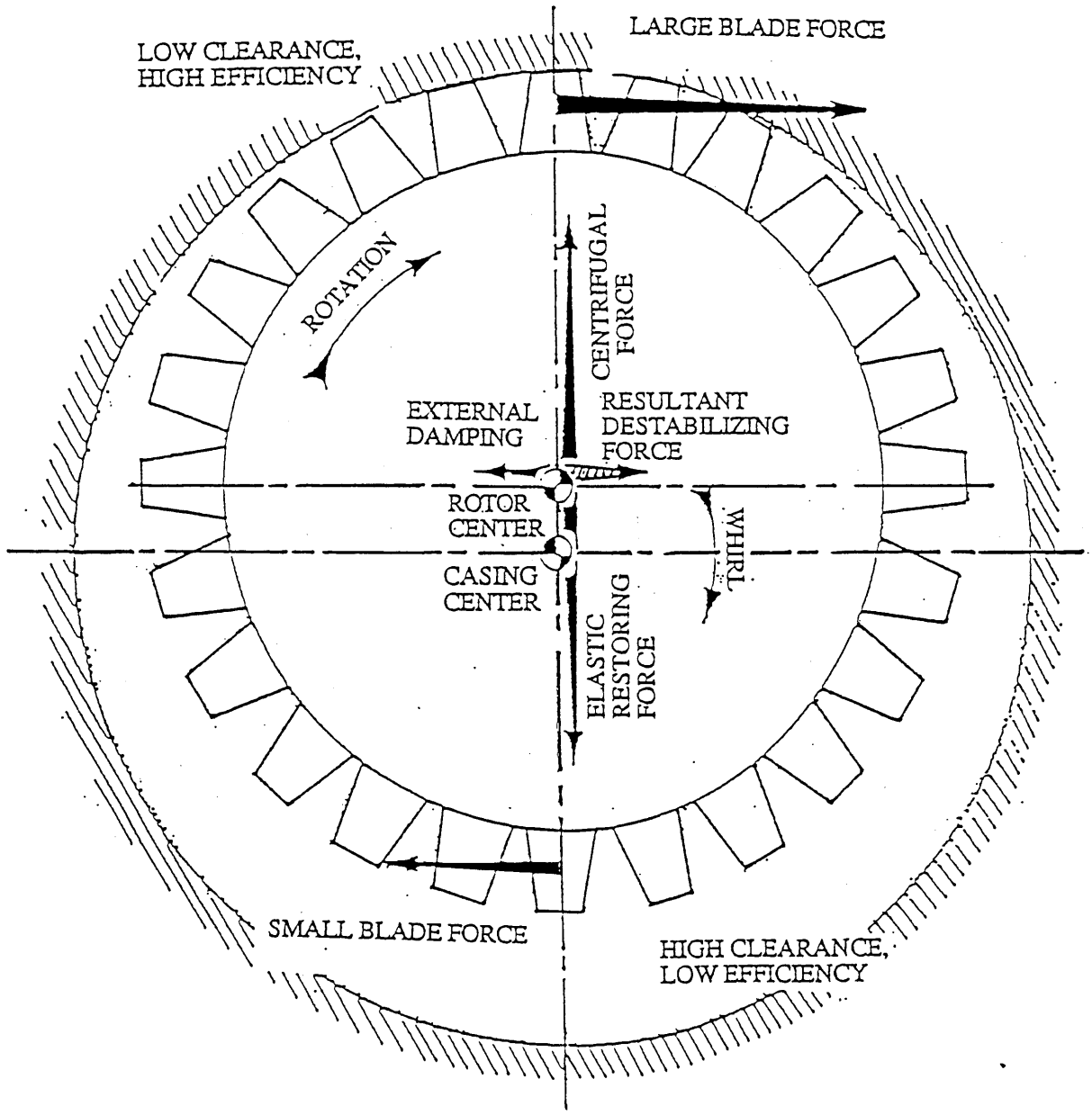

Fig. 1.3 Alford force destabilizing mechanism [5]

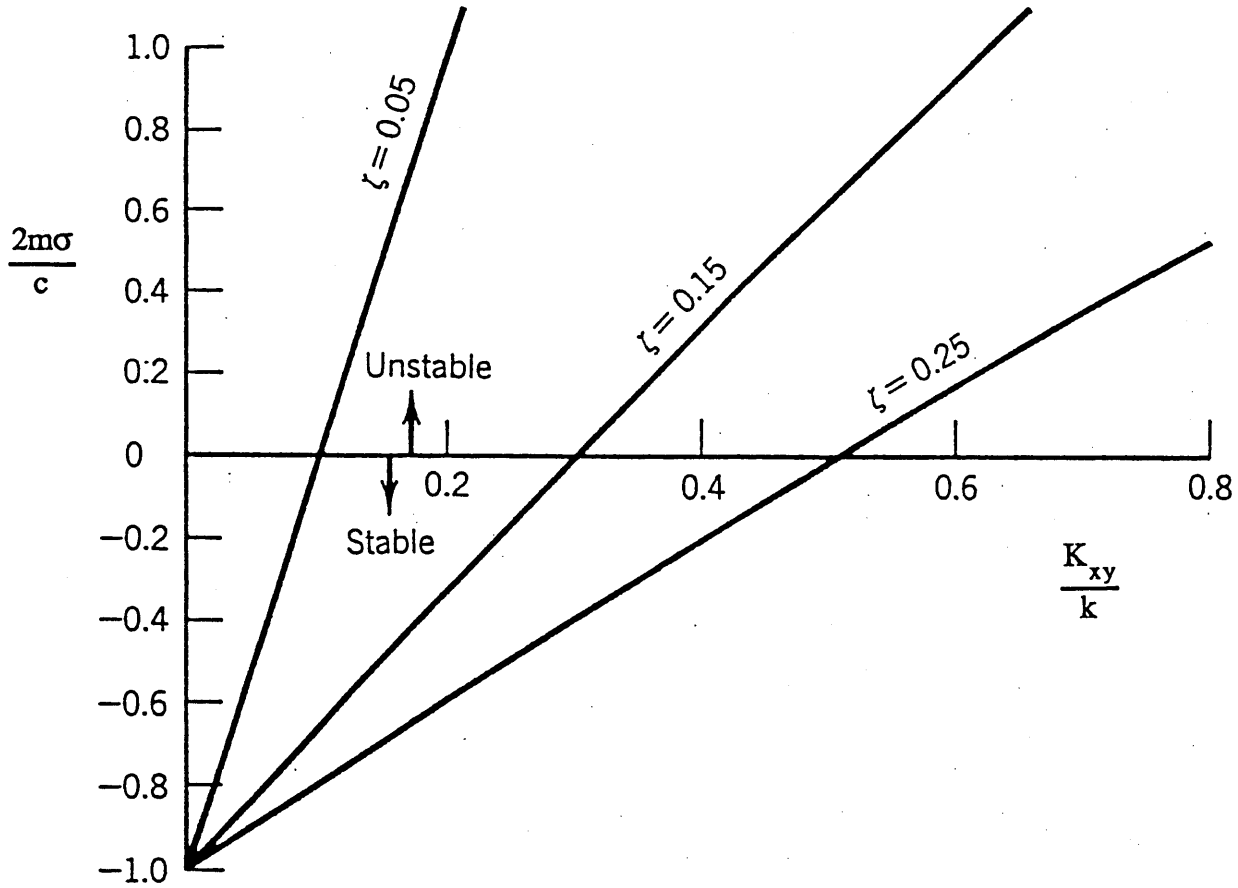

Fig. 1.4 Effect of cross-coupled stiffness K_{xy} on whirl stability

CHAPTER 2

THE ALFORD FORCE

2.1 Pioneering Work

As stated earlier, the main emphasis of the work in this thesis is the Alford force (equivalent to Thomas force in European designation). This mechanism was proposed by H.J. Thomas [17] in 1958 to explain aerodynamic instabilities in high power steam turbines and independently by J.S. Alford [1] in 1965 to explain similar phenomena in gas turbine engines.

The essence of their arguments is as follows: Ideally, a turbine rotor is perfectly concentric with the turbine casing. In practice, however, this is never the case. Many factors such as vibration, for instance, can cause a rotor to be slightly off-centered. The blade-tip clearances of an off-centered rotor will not be uniform around the circumference of the turbine. Blades with a smaller tip clearance will have less losses and therefore be more efficient than blades with a larger tip clearance. Greater blade efficiency means more fluid energy is available to do work on the blade and therefore it is expected that blades with smaller tip clearance will have a larger tangential force than blades with larger tip clearance. The local blade forces acting together will result in a lateral force on the rotor in a direction perpendicular to the rotor eccentricity. This resultant force also acts in the direction of rotor rotation so a forward whirl will be induced.

The Alford force, unlike other sources of self-excited vibration, is proportional to the turbine loading [1]. With the trend today for high power density turbines the Alford force is possibly one of the most important destabilizing force mechanisms. Unfortunately, little data currently exist on this mechanism limiting the capability of the designer to fully account for this instability mechanism.

2.1.1 Thomas Model

Thomas' model uses the variation in mass flow loss through the blade-tip gap to calculate the destabilizing force. The local tangential blade force is assumed to be proportional to the blade-tip clearance since the mass flow through the blade-tip gap does no useful work. Assuming the rotor is statically offset a distance e_x, the resultant lateral destabilizing force acting on the rotor in a direction perpendicular to the eccentricity can be expressed as [11],

$$F_y = F_{id}\, k_2 \frac{e_x}{H}$$

where F_{id} is the ideal total tangential blade force (tangential force of the turbine at zero blade-tip clearance), H is the blade height and k_2 is known as the "excitation coefficient". The excitation coefficient, k_2, is equal to the sum of a clearance variation coefficient, k_{2s}, and a pressure variation coefficient, k_{2d}, and its value ranges from zero to around 3 depending on turbine design and operating point [18]. An empirical correlation for k_{2s} is given by Urlichs [18] as,

$$k_{2s} = \frac{1}{2}\left[\frac{k'}{\sqrt{z'}\sin\alpha_1}\frac{d_n}{d_m}\frac{l''}{l'} + \frac{k''}{\sqrt{z''}\sin\beta_2}\frac{d_l}{d_m}\right]$$

α_1 and β_2 are the stator and rotor leaving angles, z" and z' are the number of seal strips of the stator and rotor, d_n and d_l are the seal diameters of the stator and rotor, d_m is the mean blade diameter, k' and k" are dimensionless experimental coefficients which depend on the turbine operating point and l' and l" are the blade heights of the stator and rotor.

2.1.2 Alford Model

Somewhat different from Thomas' model, Alford's uses the concept of local efficiency of a turbine to calculate the destabilizing force. His argument is as follows: It is known from experimental data of concentric turbines that the efficiency is approximately a linear function of the blade-tip clearance,

$$\eta_m = \eta_0 \left(1 - \alpha \frac{s}{H}\right)$$

where η_m is the efficiency for a concentric turbine with a blade-tip clearance, s. η_0 is the ideal or zero blade-tip clearance efficiency, α is a numerical factor which is dependent on turbine geometry and operating point and H is the blade height. It is assumed that the local efficiency also behaves in this manner. For a turbine which is off-centered by a value e_x (see figure 2.1) the local blade-tip clearance at a position θ is approximately,

$$\delta(\theta) = \delta_m - e_x \cos\theta$$

where δ_m is the average or concentric blade-tip clearance and θ is measured from the point of smallest gap. The local efficiency is a function of the local blade-tip clearance, $\delta(\theta)$, the variation being proportional to the ratio of eccentricity to blade height and can be written as,

$$\eta(\theta) = \eta_m \left(1 + \beta \frac{e_x}{H} \cos\theta\right)$$

where η_m is the average or concentric efficiency corresponding to a concentric turbine with blade-tip clearance δ_m and β is a numerical factor which is again dependent on turbine geometry and operating point.

For a constant speed turbine with constant inlet and exit conditions the local tangential blade force (and hence the local rotor torque) is directly proportional to the local efficiency. Therefore, the local torque per radian can be expressed as,

$$\tau(\theta) = \tau_m \left(1 + \beta \frac{e_x}{H} \cos\theta\right)$$

where τ_m is the average or concentric torque per radian. The component of lateral force per radian in the direction perpendicular to the eccentricity, e_x, is then,

$$f_y(\theta) = \frac{\tau(\theta)}{R} \cos\theta = \frac{\tau_m}{R} \left(1 + \beta \frac{e_x}{H} \cos\theta\right) \cos\theta$$

The total force perpendicular to the eccentricity will then be,

$$F_y = \int_0^{2\pi} f_y(\theta)\, d\theta = \frac{\tau_m}{R} \int_0^{2\pi} \left(1 + \beta \frac{e_x}{H} \cos\theta\right) \cos\theta\, d\theta$$

$$= \pi \beta \frac{\tau_m}{R} \frac{e_x}{H}$$

The total rotor torque is,

$$T = \int_0^{2\pi} \tau(\theta)\, d\theta = \int_0^{2\pi} \tau_m \left(1 + \beta \frac{e_x}{H} \cos\theta\right) d\theta$$

$$= 2\pi \tau_m$$

Substituting into the equation for the total force perpendicular to the eccentricity gives,

$$F_y = \frac{\beta}{2} \frac{T}{R} \frac{e_x}{H}$$

In terms of the total ideal tangential force which is,

$$F_{id} = \frac{T}{R}$$

the component of the total lateral force in the direction perpendicular to the eccentricity is [11],

$$F_y = F_{id} \frac{\beta}{2} \frac{e_x}{H}$$

β is known as the Alford factor and is dependent on turbine geometry and operating point. $\beta/2$ is equivalent to Thomas' excitation coefficient, k_2,which was stated earlier to range from zero to around 3.

One questionable assumption in Alford's calculation of blade-tip force is his assumption of uniform upstream and downstream flow fields. In sub-sonic flow any flow perturbations which may exist due to rotor blade-tip clearance variation are able to travel upstream thus disturbing the turbine inlet flow. The inlet flow would then be non-uniform and may affect the rotor forces. In fact, it has been found by Qiu and Martinez-Sanchez [16] that the flow field perturbations do significantly affect prediction of the blade-tip force and cannot always be ignored when calculating destabilizing blade-tip forces.

2.2 Past Experimental Work

Although the concepts of Thomas and Alford have been around for over a quarter of a century, experimental verification of blade-tip force calculations has been limited. Some early, very limited work was done in Germany by E. Pollmann [15]. Pollmann first pointed out that inlet swirl was important in seal force calculations. More quantitative work in this area was

performed by Thomas' co-workers K. Urlich and R. Wohlrab, in Germany, whose work will be reviewed. Experimental investigation in the U.S. has been limited to the work of J.M. Vance and F.J. Laudadio

2.2.1 Review of Work by K. Urlichs

Karl Urlichs' work, completed in 1975, was one of the two major research efforts on clearance excitation forces done at the Munich Technical University under H.J. Thomas. His work is an attempt to refine the analytical work done by Thomas and to experimentally investigate clearance excitation forces. The emphasis of his work was on the behavior of rotor shroud seals, however some attention was given to unshrouded turbine blades.

The main emphasis of his theoretical work was to model the flow in eccentric non-contact gas seals. Simply put, he wrote the conservation equations of mass, momentum and energy through the seal passage using several empirical coefficients for friction, flow turning, etc. The solutions which were found iteratively generally give good predictions for flow patterns in eccentric seals. His calculations showed that the excitation forces increase with increasing pressure gradient and also with increases in the amount of swirl at the seal inlet

Of more interest to the context of this thesis is his experimental work. His facility was open loop with air at near atmospheric pressure as the working fluid. The rotor used was 0.32 m (12.6 in) in diameter with a blade height of 0.02 m (0.8 in) and blade chord of 0.015 m (0.59 in). It had impulse blading and both shrouded and unshrouded turbines were tested. The shrouded version had shroud seals with either 2 or 3 seal strips. The rotor was supported by bearings mounted on a frame which was restrained laterally by stiff loadcells. Axial support of the rotor was provided by thrust relief cables. The maximum mass flow was about 0.4 kg/sec (0.03 slug/s) which gave a turbine power of up to 4 kW (5.4 hp) at a pressure drop of 20 kPa (2.9 psi). This limited the Reynold's no. to under 10^5 which does not realistically model present day high performance turbines. The turbine power was absorbed by a

dynamometer brake. Rotor eccentricities were achieved by laterally offsetting the turbine casing, which could only be done statically.

Urlich put a lot of effort into making detailed measurements of pressure variations around the rotor and stator seals. With U-tube manometers he was able to measure pressures with a resolution on the order of 100 Pa (0.02 psi) which proved to be adequate. He found that most pressure patterns were roughly sinusoidal with amplitude of approximately 600 Pa (0.09 psi) per $1x10^{-4}$ m (4 mils) offset, the maximum pressure occurring slightly before the point of narrowest blade-tip clearance.

For the unshrouded turbine the general trends, such as linearity for cross force magnitude were generally correct as predicted by the simple Alford or Thomas model. k_2 was found to range from 1 to 3 for different operating conditions. Two trends found which are not predicted by the Alford model were (i) an increase in k_2 with increasing stator to rotor axial spacing and (ii) a decrease in k_2 with increasing nominal rotor blade-tip clearance.

2.2.2 Review of Work by R. Wohlrab

The second major research effort under H.J.Thomas at the Munich Technical University was done by Raimund Wohlrab [21] who also completed his work in 1975. This facility was closed loop with air pressurized up to 600 kPa (90 psi) as the operating fluid. The maximum mass flow rate was 8 kg/sec (0.55 slug/sec) which produced up to 400 kW (540 hp) of power at 5500 rpm. The turbine operated at more realistic Reynold's no., around 5×10^5 based on rotor exit conditions.

Wohlrab tested three different rotors, all with seal shrouds; two 50% reaction, each with different blading, and an impulse turbine. He also tested a three stage turbine which used the same rotor as one of the 50% reaction turbines used in the single stage tests. The rotor mean radius was 0.46 m (18 in) and the blade height was 0.04 m (1.6 in). The rotor was supported axially by thrust relief cables and laterally by two pairs of loadcells which were perpendicular to each other. Both rotor and stator casings were able to independently move laterally and

axially to vary both blade-tip clearance and rotor to stator axial clearance, respectively. The independent movement of the casings allowed separation of stator and rotor effects.

Lateral rotor forces were measured for a wide variety of operating conditions. However, little effort was put into measuring pressure patterns at the shroud seals. The results were somewhat mixed. He found k_2 to be somewhat less than predicted for 50% reaction turbine with small blading, scattered but closer to predicted for 50% reaction turbine with larger blading and 2-3 times larger than predicted for impulse turbine.

The facility was also able to perform dynamic tests. The frequency of rotor vibration was limited to values lower than would be expected in actual turbomachines, but it was a first attempt at measuring the effects of time varying blade-tip clearance.

2.2.3 Review of Work by J.M. Vance and F.J. Laudadio

The only experimental work relating to the Alford force in the U.S. was done by J.M. Vance and F.J. Laudadio [20] in 1984. Their experimental rig consisted of a small, 0.15 m (6 in) O.D., high speed, axial flow fan in an open loop air system. Torque was less than 0.1 Nm (0.9 in lb) at a maximum speed of 7000 rpm. The speed of the rotor could be varied independently from torque by changes in the motor current and inlet velocity. Blade-tip clearance variations were achieved by offsetting the rotor casing. The rotor bearings were supported by relatively flexible springs which allowed the small cross force of less than 0.01 kg (0.02 lb) to produce a measurable rotor deflection. The rotor deflection was measured with a proximity probe which was calibrated to give the lateral force in grams.

The lateral force was measured for many combinations of speed, torque and eccentricity, however no measurements were made of inlet velocity or pressures. The work verified that the Alford force varies linearly with both rotor offset and torque which is as predicted by Alford's formula. They also found that no Alford force appears until a certain non-zero torque value was reached. This does not agree with Alford's formula which says the y-intercept of the

lateral force vs. torque is zero. Values for β were calculated and found to be dependent on both torque and speed and ranged from 0.5 to 2.5 (k_2 from 0.25 to 1.25).

Significant findings have been made by the three experimental efforts mentioned above. The existence of a lateral force caused by rotor eccentricity has been verified and found to agree relatively closely with Alford's simple, linear formula. However, in order for a designer to confidently use the Alford force to accurately predict stability thresholds more experimental measurements on realistic models of full scale turbomachinery are necessary.

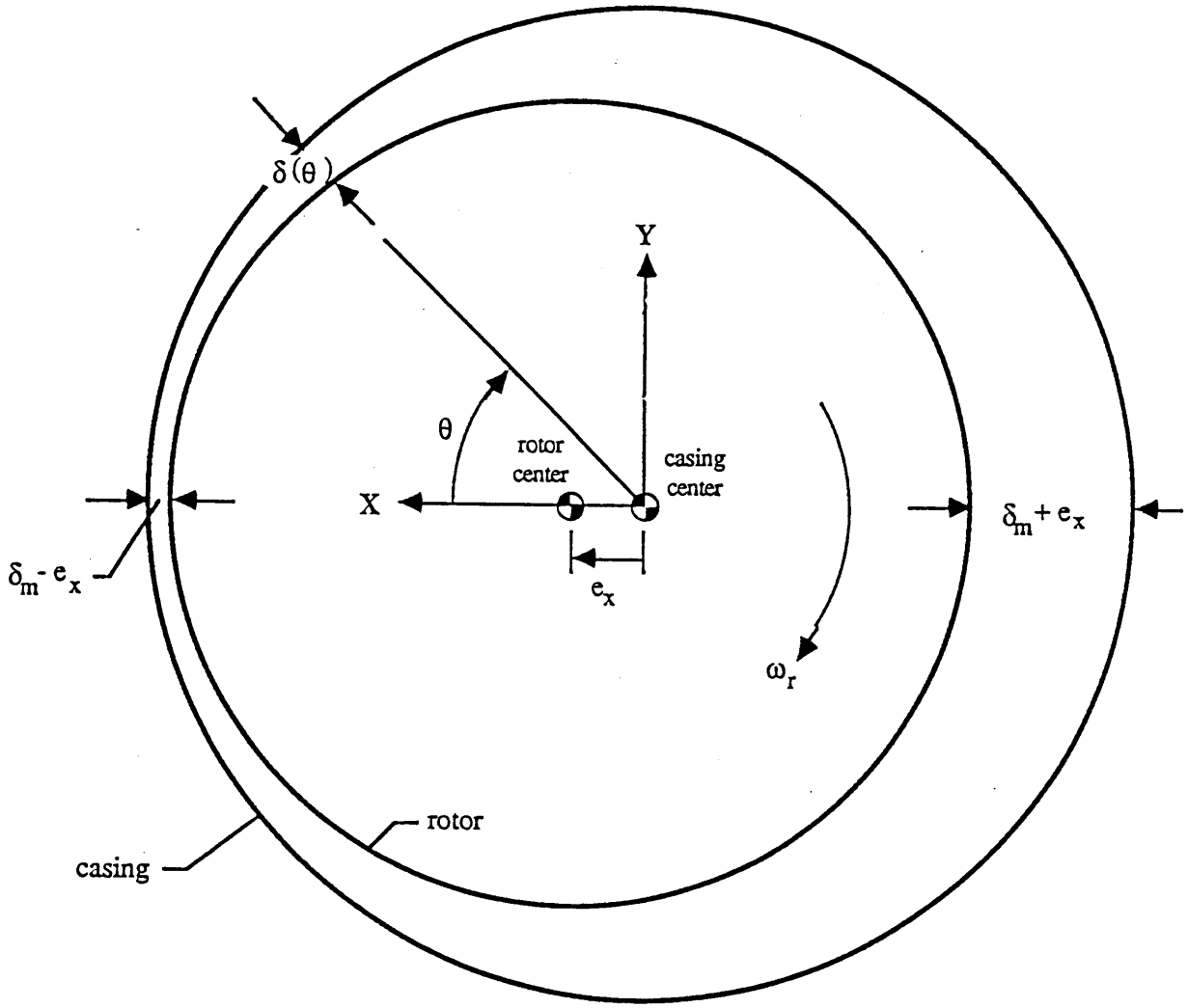

Fig. 2.1 Geometry for Alford's model

CHAPTER 3

THE EXPERIMENTAL FACILITY

In order to better understand the Alford force and its effect on turbomachine stability it was determined that a thorough experimental investigation was necessary. To this end, an Alford force test facility was designed and built which enables detailed study of the Alford force and the flow parameters associated with it. The facility is comprised of three main sections; the turbine test section, the flow loop and the transmission and power absorption system. This chapter presents the design features of these and the measurement capabilities of the facility. An overall view of the facility is shown in figures 3.1 and 3.2.

It should be mentioned that, in general, turbine blade-tip clearance excitation forces and seal forces act together. In some cases the destabilizing forces from these two mechanisms will cancel each other while in others will add to each other making prediction of instability onset more complicated than if each was acting alone. For this reason a second facility was designed and built at M.I.T. by Millsaps [12] to study in detail the forces generated by a whirling labyrinth seal. Also, later builds of the Alford force test facility may include a shrouded rotor to study effect of rotor offset on shroud seals.

At this point it is also appropriate to mention that the major portion of the overall flow loop and test turbine design was done by Jery, Qiu, Martinez-Sanchez and Greitzer [9]. The author's involvement was mainly in the construction of the facility, instrumentation and data acquisition set-up and calibration, system debugging and facility shake-down and the preliminary measurements which are presented in this thesis.

3.1 Turbine Test Section Design

The objective of this facility is to accurately measure lateral forces acting on a turbine rotor due to small lateral displacements of the rotor away from its concentric position and to measure the associated flow perturbations. It is desired to measure the effects of both static and dynamic rotor displacements. To accomplish this objective a turbine test section which allows the turbine rotor to be laterally displaced while the turbine casing remains stationary was designed and constructed. It is heavily instrumented to allow rotor force and flow field measurements. Drawings of the turbine test section and its components are shown in figures 3.3 through 3.7.

In an effort to test a turbine which would be representative of turbines used in aerospace applications today it was necessary to design the test turbine with realistic flow and work coefficients and Reynolds and Mach numbers. Since flow and work coefficients are fixed by geometrical ratios and flow angles, realistic coefficients were achieved by replicating an existing turbine. Since our interest is the Space Shuttle main engine HPFTP and HPOTP the test turbine used is modeled after these turbines. The first series of tests and all of the tests done for this thesis were done with a full scale replica of the unshrouded HPFTP turbine first stage. Later, a shroud may be added to this rotor to enable study of shroud seals in the same facility. Adding a shroud to the existing rotor has the advantages of lower cost and easier integration to the existing facility.

Replicating existing turbines has an additional practical advantage in that the aerodynamic blading design has already been done. This made the rotor design much simpler since blade profile drawings and coordinates were already available. Pertinent design parameters of the HPFTP first stage and Alford force test facility turbines are presented in Table 3.1.

The Mach numbers in the SSME fuel turbopump are low enough (0.414 maximum) so that they play only a minor role in its performance. Therefore, the test turbine was designed to have relatively low Mach numbers, no more than 0.5.

Achieving realistic Reynolds numbers (Re) is more difficult since representative turbines typically operate at values above 10^6 (the HPFTP for example operates at $5.6x10^6$ based on rotor leaving conditions). Achieving Re in this range in laboratory tests is generally difficult. For example, it was stated earlier that Urlichs was limited to Re below 10^5 in his tests and even Wohlrab with a much larger facility was limited to $5x10^5$.

It is known that Reynolds number effects become less important at high Re when fully turbulent flow is established. Below the turbulent regime it is difficult to predict how other factors such as blade aspect ratio, solidity and others affect performance. For this reason it is desirable to operate at relatively high Re, above the transition region.

In order to achieve the desired value of Re it was concluded that an air facility would be impractical. It was therefore decided to use Freon-12 gas as the operating fluid instead of air. This required a closed loop facility which will be described in more detail in the next section. The density of Freon (for the remainder of this thesis simply "Freon" will be used to refer to "Freon-12") is about four times that of air while its viscosity is about 30% lower which enables operation at a Re of about 9×10^5 based on design rotor leaving conditions. It was stated earlier that the SSME fuel turbopump operates at a Re of about 5.6×10^6 based on rotor leaving conditions. Even though the Re of the test turbine is still below that of the SSME fuel turbopump it is well above the laminar to turbulent transition region which typically occurs at Re below $2x10^5$. Another advantage of using Freon is that for the same size turbine operating at at fixed pressure, temperature and Mach number the turbine power is only about one-third of what it would be if operating in air. This reduces the necessary size of most other components of the loop, such as the compressor and power absorption system, which in general simplifies design and construction and reduces cost. One disadvantage of using Freon is the fact that many materials are not compatible for use in a Freon environment. This proved to be somewhat of a nuisance in that all components that are in contact with the operating fluid, such as o-rings, gaskets, tubing and pressure transducers, for instance, had to be Freon compatible.

Even so, using Freon in a closed loop system allows building a reasonably sized facility which operates at realistic Re.

In order to measure the forces acting on the rotor, the rotor is attached to the drive shaft directly through a rotating dynamometer (see fig. 3.4a, item 9). Because the dynamometer is attached directly to the rotor, the forces measured are those strictly acting on the rotor. Problems in measurements which can be caused by extraneous forces such as transmission noise has nearly been eliminated. Also, because the dynamometer is rotating, measurement of the steady forces which we are attempting to measure will result in an unsteady signal. This eliminates the errors due to transducer electrical drift which occur in steady measurements.

The dynamometer simply consists of four stainless steel equally sized, equally spaced square posts (see fig. 3.7) which run parallel to the rotor axis at a radius of 5.3 cm (2.1 inches). The posts are instrumented with nine sets of full Wheatstone bridge semi-conductor strain gage sets which allows measurement of all six components of force and moment acting on the rotor. The bridges require four sets of 10 conductor instrumentation wires which run through the hollow center of the drive shaft. To seal the wires at the lower end of the shaft, the hollow shaft center was filled with wax. The instrumentation of the dynamometer and its calibration will be explained in more detail in chapter 4. A detailed description of the procedure used for the mechanical design of the rotating dynamometer is given by Jery [8].

Because the dynamometer measures only the unsteady part of each force and moment component, some alternate measurement of the steady torque is necessary. This is done with two 45 degree axis full Wheatstone bridge foil strain gage sets. One set is located directly below the dynamometer which senses the torque most directly (see fig. 3.4a, item 15). A second set is attached near the top of the lower shaft (see fig. 3.5, item 14).

The turbine drive shaft is supported by bearings which are held in a stainless steel bearing housing (see fig. 3.4b). The bearings are lubricated with a special Freon resistant grease, KRYTOX ®, obtained from Du Pont. The bearing housing is supported solely by four rigid struts, which are perpendicular to the rotor axis. The struts extend radially outward from the

bearing housing through linear bearings in the test section case. This allows the struts to move in the turbine radial direction while being supported firmly in the turbine axial direction. Because the struts are connected to the bearing housing which supports the rotor drive shaft, the turbine rotor is able to move laterally while the turbine casing remains stationary.

It was decided to offset the rotor instead of the casing for two major reasons. First, because the facility is a closed loop facility all components which are in contact with the working gas must be sealed. Designing a sealed casing which is still able to move laterally proved to be quite complicated. Secondly, moving the casing would necessitate having gaps on the outer diameter of the flow path. This could potentially cause flow disturbances in the blade-tip region.

The upper and lower struts on each side of the casing are rigidly connected by steel bars. A cam mechanism is used to control the displacement of one of the bars (see fig. 3.4b). Through an adjustment mechanism, the cam can be adjusted to have a displacement amplitude from zero to 0.32 mm (12.5 mils). This allows the rotor to be positioned anywhere between -0.32 mm to +0.32 mm (-12.5 to + 12.5 mils) away from its concentric position. The cam is turned by a Superior Electric stepper motor which is controlled by the computer. It allows the rotor to be moved and held at a desired lateral offset to investigate static offset effects or to be moved continuously in a sinusoidal motion at up to 10 Hz frequency to study the effects of low frequency time varying eccentricity. The struts are sealed with standard PolyPak seals manufactured by Parker Packing.

An alternate method of offsetting the rotor and the method used for the data in this thesis is to place shims under one connecting bar at the top and bottom struts while the retaining nuts on the other side are tightened. Stainless steel shims were used allowing rotor offsets up to a maximum of 0.51 mm (20.0 mils). The data for this thesis, however, were all taken at a maximum eccentricity of only 0.33 mm (13 mils) to assure no blade-tip rub would occur. The advantage of this method is that the rotor is held in place rigidly rather than by a relatively soft spring. Of course, only static rotor offsets can be achieved.

In an effort to measure the effects of stator-to-rotor clearance on the generated lateral force, it is also possible to vary the stator-to-rotor axial clearance. The stator can be positioned in one of three different axial locations. The stator is held in place by screws which go through the turbine case to threaded holes in the stator blades (see fig. 3.4a, item 16). Three rings of holes through the casing each separated by 5 mm (0.2 in) are provided to position and hold the stator. The screws used to secure the stator are special sealing screws which have an o-ring underneath the screw head. The unused holes are sealed in a similar manner.

The test section casing is heavily instrumented with static pressure taps and various provisions for pressure and hot-wire probes. The instrumentation map is shown in figures 4.9 through 4.11 and will be discussed in more detail in Chapter 4. A unique feature of the test section casing is that the entire casing is rotatable (see fig. 3.4a). This allows continuous measurement of pressures and flow angles in the azimuthal direction. The casing is supported by three bearings and is sealed by PolyPack rotatable seals. A chain which wraps around and is pinned to the casing is driven by a pinion sprocket behind the test section. The sprocket is driven through a 50:1 gear reducer by a stepper motor. An adjustable release clutch connects the motor and gearbox in case the torque required to turn the casing becomes excessive. The casing can be rotated a maximum of ±90° at a speed of around 5 rpm. Because provisions for pressure measurement at each axial location are provided 180° apart the entire azimuthal range can be covered. Mechanical stops are built in to prevent over rotation in either direction.

Pressure tubes are connected to the 0.51 mm (0.020 in) static taps by specially fabricated brass fittings. These consist of 1/4 inch Polyflow fittings which are soldered to 1/8 inch brass tubes. The brass tubes are "epoxied" to the static tap holes in the test section casing. This provides a simple connection of the static taps to pressure tubes which can be connected to the Scanivalve for pressure measurement.

Bently Nevada, model 7200, non-contacting, eddy current proximity probes are used to measure the amount of turbine offset. The probes are mounted in the test section casing by threaded plastic plugs. These are required because the metal casing would cause an

interference if the probes were mounted directly through the steel casing. The probes look directly at the rotor blade-tips. It was felt that sensing the blade-tips directly rather than the shaft surface would be the most reliable way to determine the rotor position relative to the casing. However, it was not known beforehand how well this arrangement would perform since the probe can only "see" the small blade-tip surface as it passes by at high speed. The blade surface which the proximity probe senses is about 2.8 mm (0.11 in) long while the manufacturer recommends no less than three times the probe diameter (in our case 3 x 5 mm or 15 mm). The performance of this arrangement was tested by looking at the proximeter output signal with an oscilloscope while the rotor was spun with the DC motor. The signal proved to be exceptionally good at all rotor speeds.

An optical encoder is attached to the drive shaft to provide a measurement of rotor angular position as it spins (see fig. 3.4b, item 13). The encoder, manufactured by BEI Motion Systems Company, model number 5VN670HBZ, outputs a 4096 pulse per revolution TTL[1] signal and a once per revolution TTL pulse output for zero reference. The optical encoder is used for a tachometer input as well as to clock and trigger the data acquisition as will be explained in the next chapter. The tachometer is model number DT-5AG, manufactured by Shimpo America Corp. The rotor speed is displayed digitally on the instrumentation rack. Also, the tachometer provides an analog output which can be digitized and stored directly during data acquisition.

The temperature of the drive shaft bearings can be monitored to prevent overheating. A type T thermocouple is attached to the bearings and the temperature is displayed by an Omega Engineering digital display, part number 115TF.

An alarm is also provided to indicate if rotor offset is excessive and is producing blade-tip rub. The nominal blade-tip clearance is 0.65 mm (0.026 in) which provides an adequate margin of safety under normal operating conditions. However, under unusual circumstance

[1]TTL is an industry standard for digital circuitry voltage levels. From zero and 0.4 V is a TTL low signal and between 2.4 and 5 V is a TTL high signal

should the rotor eccentricity become excessive, an electrically insulated snubber bearing would be contacted by the rotor. When the rotor touches the snubber bearing an alarm is tripped to warn the operator. The electrical schematic for the alarm is shown in figure 3.8.

The entire test section is mounted on a 5 cm (2 in) thick steel plate bolted to a test stand which is constructed from six inch steel box beams welded together (see fig. 3.5). The steel plate is shimmed level, pinned and bolted in place during testing, but can be unbolted and lowered onto rollers and rolled away from the flow loop to allow access to the test section during assembly and disassembly. The test stand sits on six vibration reducing mounts which are bolted to the floor.

3.2 Flow Loop

The flow loop is a closed loop system using Freon-12 as the operating fluid. This configuration was chosen due to the relatively high density and low viscosity of Freon which is desirable in order to achieve the highest possible Reynolds number, as was explained in the previous section.

Commercially available 0.30 m (12 in) and 0.25 m (10 in) PVC piping and fittings were used for the construction. The piping is rated at 90 psig which is well above our maximum operating pressure of 15 psig and is compatible with Freon. Joints in the pipe sections are sealed with neoprene gaskets. The loop is supported with several structures attached to the concrete roof, floor and wall of the test facility room.

Freon is circulated through the flow loop by a compressor driven by a General Electric 75 kW (100 hp) AC motor. The compressor is manufactured by The Spencer Turbine Company, Windsor, CT. This model was chosen by estimating the flow losses in the loop and the pressure drop across the turbine which resulted in a minimum necessary compressor pressure ratio of 1.295. Once the compressor pressure ratio was determined the final factor was the

required mass flow which is simply the design mass flow of the turbine, 4.48 kg/s (the actual design specification was 5 kg/s to allow off-design operation).

Performance curves were provided by the manufacturer for different inlet pressures. A sample is shown in figure 3.10 for Freon.at 101.3 kPa (14.7 psia) inlet pressure. The curve shows an operating range of 15.6 to 42.5 m^3/min (550 to 1500 ft^3/min) at the inlet. The size of the AC motor which drives the compressor was chosen for a maximum mean loop pressure of 203 kPa (29.4 psia) and an inlet temperature of 298 K (80 °F) which translates to an inlet volume flow of approximately 1300 cfm. From the compressor performance curve for a 203 kPa mean loop pressure the power necessary is 67 kW (90 hp). Assuming a motor efficiency of 90%, the AC motor was sized at 75 kW (100 hp). The compressor and motor are mounted on the building roof outside of the test facility room (see fig. 3.2).

In order to achieve the highest possible density of the flow entering the turbine and to prevent overheating, a heat exchanger is used to remove heat added by the compressor. The heat exchanger is rated at 52 kW (177,430 btu/hr) which was chosen by subtracting the test turbine design power (14.55 kW) form the compressor power (67 kW). The result (52 kW) is the excess power which only raises the temperature of the gas in the loop and is thus the amount of power needed to be removed by the heat exchanger. City water is used to remove the heat and inlet temperatures of as low as 40° F in the winter months and 75° F in the summer months have been encountered. The lower limit on inlet temperature is quite dependent on the time of year, since un-cooled city water is used.

The mass flow through the loop is measured using a B I F Plastic Insert Venturi Tube, model no. 0182-10-2231 (see fig. 3.1, item 3). This Venturi provides mass flow measurement accuracy of 1% of reading at a low head loss. The differential pressure is measured with a 17.2 kPa (2.5 psi) differential pressure gauge which will be discussed in the next chapter.

Several flow straighteners are provided at various locations around the loop to assure uniform flow at the turbine inlet (see fig. 3.1, item 2). The flow straighteners consist of a 5.1

cm (2 in) thick honeycomb section followed about 2.5 cm (1 in) downstream by a wire screen to remove any eddys produced by the honeycomb.

The mass flow through the loop is controlled by a by-pass loop and throttle valves (see fig. 3.1). The by-pass loop allows flow to by-pass the test section back to the compressor inlet. The amount of bypass is controlled by a servo driven butterfly valve. The servo valve is powered by 115 V AC and a switch to control it is located on the instrumentation rack. Two throttle valves are also used to control the mass flow. The valves are simple hand-operated butterfly valves.

An attempt was made to make the flow loop completely leak-free. However with the hundreds of connections, seals, etc. an absolute gas tight loop was not achieved. The primary source of leaks are mainly the dynamic seals, such as the compressor seal and test section strut seals. The leak rate is slow enough (less than 0.016 kg/min or 0.1% of total gas in loop per minute at maximum operating pressure) that it has a negligible effect on data measurements, however, over time the loop pressure drops significantly enough to warrant the use of a pressure regulator to keep the loop at a constant pressure. The regulator chosen is a Fairchild Model 10 which supplies a constant outlet pressure independent of supply line pressure variations. The outlet pressure can be set up to 20 psig which exceeds our maximum necessary loop pressure. The regulator sensitivity is 31 Pa (0.005 psi) which results in less than 0.02% variation in loop pressure at design conditions.

The nominal pressure level in the loop can be adjusted from 2.8 to about 210 kPa (0.4 to 30 psia). The vacuum pump, manufactured by Welch, model no. 1397, is mounted on the test section frame through vibration absorbing rubber mounts to reduce transmitted vibrations to the test section. The pump is powered by a 0.74 kW (1 hp) electric motor and can evacuate the loop to maximum vacuum in approximately one hour. As stated earlier, the flow loop can be pressurized to 210 kPa (30 psia), which is done using standard Freon canisters. The procedure to fill the loop involves first evacuating the loop with the vacuum pump then pressurizing to the desired nominal loop pressure with Freon. Because the loop can be

evacuated to only 2.8 kPa (0.5 psia) approximately 2% air will remain in the loop after filling with Freon to design pressure. To reduce the air remaining, the loop may be partially evacuated and refilled to the desired operating pressure. This assures less than 1% air remaining in the loop. The effect of 1% air in the loop can be determined by calculating the error in the density of the loop if it was assumed 100% Freon. From simple ideal gas relations it can be shown that the percentage error in density is,

$$\%\text{error} = \frac{y_{air}M_{air} + (y_{Freon} - 1)\, M_{Freon}}{y_{air}M_{air} + y_{Freon}M_{Freon}} \times 100$$

where y is the mole fraction and M is the molecular weight. For 1% air in the loop (y_{air} = 0.01, y_{Freon} = 0.99) the density is overestimated by assuming 100% Freon by only 0.77% which has negligible effect on the measurements. In actuality better than 99% Freon can be achieved making the error even less.

After completion of testing the Freon in the loop can be recovered and stored. This is achieved by the use of a Freon recovery system. The recovery system is a self-contained unit model no. 17200 manufactured by Robinair . Although the system has the capability to recover Freon to sub-atmospheric pressure, generally the loop pressure is brought to just above atmospheric and the recovery stopped. A schematic of the vacuum, pressurizing and recovery plumbing is shown in fig. 3.9.

3.2 Transmission and Power Absorption System

The purpose of the drive system is to absorb the power of the turbine as well as to spin the rotor without running the compressor if desired. This system consists of a lower drive

shaft, pulleys and belt, DC motor/generator, resistors to dissipate electrical energy and DC power supplies to drive the DC motor.

The lower drive shaft is connected to the turbine drive shaft through a flexible coupling (see fig. 3.5) which allows for angular misalignment between the two shafts. This is especially important since the turbine drive shaft will be purposely displaced during testing causing misalignment between the two shafts. The shaft exits the turbine exhaust plenum through a rotating seal and bearing. Outside the plenum the shaft is connected to another shaft with a Dodge Para-Flex flexible coupling which allows for both angular and lateral misalignment. A full bridge, 45 degree axis torque sensitive strain gauge set is located just below the coupling on the shaft (see fig. 3.5, item 14) which is calibrated to measure the torque acting on the rotor.

The rotating seal which seals the lower shaft (see fig. 3.5, item 7) is a John Crane type 28 series, dry-running, non-contact gas seal. It is a double face seal which has sealing capabilities in both vacuum and pressure. Also, it is capable of operation under considerable shaft eccentricity and tilt which is necessary because of the rotor offset which causes slight misalignment of the lower shaft.

The shaft which is connected to the lower drive shaft is supported by two bearings (see fig. 3.5). A 34-tooth drive belt pulley sprocket is keyed to this shaft between the two bearings. A belt connects this sprocket to a 56-tooth sprocket which is connected through a Dodge Para-Flex high speed flexible coupling to the DC motor/generator (see fig. 3.2). This provides a 1.65:1 reduction between the motor and turbine. This was necessary because the maximum turbine operating speed exceeds the limiting speed of the DC motor/generator. The belt is kept in tension by a spring loaded idler pulley. The idler pulley is smooth and simply applies tensioning pressure to the back side of the belt. Provisions are made for the idler to ride on either side of the belt so that it can always apply tension to the slack side of the belt which will change depending on generator or motor mode of operation

The DC motor/generator is manufactured by Reliance Electric Co. and is rated at 40 hp. It is used as a DC generator when the turbine is running or as a motor to spin the turbine for calibration, diagnostics, etc., if desired. When operating as a generator electric power is supplied to the motor field only and the power generated by the armature is dissipated by resistors. When operated as a motor, power is supplied to both the field and armature. Both the field and armature are rated at 240 V. The maximum armature current is 142 amperes which exceeds the maximum output of the power supplies, so there is no danger of over powering the armature. The motor/generator is bolted to a heavy steel plate which is connected to the test section frame with rubber mounts to reduce the amount of motor vibration transferred to the test section.

A danger for all DC motors is the loss of field power. In theory, as the field voltage approaches zero the motor speed becomes infinite. Of course, in practice the speed would not become infinite due to inefficiencies and friction, however catastrophic failure would probably occur if field voltage was lost. For this reason a control box for the motor was designed and constructed. It consists of a field cut-out safety relay, which, in the event of loss of power to the field, interrupts power to the armature preventing the motor from over speeding. The control box also has an emergency stop button and a meter to indicate the armature voltage.

The DC motor/generator does not have a built-in cooling fan, therefore forced ventilation for cooling was implemented. A 1 hp blower is connected to the motor ventilation port which forces room air through the motor and exhausts it outside the test room. The blower is mounted on the test section frame through vibration absorbing rubber mounts to reduce transmitted vibration to the test section.

Two DC power supplies are used to provide power to the motor/generator. The power supplies used are Hewlett Packard model number 6479C. The input to the power supplies is 460V three phase AC and the output is zero to 300 V DC at a maximum current of 35 A for each unit. One power supply is used for the motor field and the other for the armature. The

armature power supply is used only during motor operation and is disconnected during generator operation.

The power absorbed by the turbine generates electrical energy by spinning the motor/generator. The electrical power generated is then dissipated into heat by resistive heating strips. The resistive strips are mounted inside a cabinet and provide a maximum dissipation of 16.4 kW (22 hp). A rheostat is also provided to vary the resistance of the circuit to vary the load on the turbine as will be explained in the next section. The rheostat is part number ED25971 manufactured by Ward Leonard and is driven by a DC motor. Because the resistive strips get quite hot, air is forced through the cabinet to provide cooling by means of a connection to the M.I.T. Gas Turbine Lab steam ejector. A schematic of the power dissipating circuit is shown in figure 3.10.

3.4 Operation

The turbine operation is quite simple and will be explained briefly in this section. The three variables in the turbine operating point are rotational speed, mass flow and pressure ratio. The system provided allows variation of two of the three while the third is held constant which allows testing at an infinite number of turbine operating conditions.

As stated earlier, the mass flow through the turbine can be controlled two different ways. First, the amount of flow "bypassed" back to the compressor inlet can be varied by varying the position of the servo driven butterfly valve in the bypass loop. Secondly, two hand-operated butterfly valves can be used to throttle the flow both upstream and downstream of the test turbine.

The rotor speed can be varied while keeping the mass flow constant by varying the load on the turbine. This also can be done in two ways. First, the generator field voltage can be varied. As the field voltage is increased the resistive load on the turbine increases, thus lowering the speed for a constant mass flow. The resistive load can also be varied through the resistor dissipating circuit. Coarse adjustments can be made by switching individual resistive

heating strips on or off. Finer adjustments can be made by varying the resistance of the motor-driven rheostat.

Table 3.1 Design parameters for SSME fuel turbopump first stage and Alford force test facility turbine

	SSME fuel turbopump, first stage	Alford force test facility turbine
Flow coefficient, ϕ	0.58	0.58
Work coefficient, ψ	1.508	1.508
Stator exit angle	70°	70°
Relative rotor inlet angle	43.9°	43.9°
Rotor exit angle	60°	60°
Absolute exit angle	−3.1°	−3.1°
Degree of reaction	0.216	0.216
Rotor mean radius, cm (in)	12.88 (5.07)	12.88 (5.07)
Number of rotor blades	63	63
Rotor blade height, cm (in)	2.17 (0.854)	2.17 (0.854)
Rotor blade chord, cm (in)	2.21 (0.870)	2.21 (0.870)
Rotation rate, rpm	34,560	3440
Axial flow velocity, m/s (in/s)	262 (10,300)	26 (1020)
Mass flow rate, kg/s (slug/s)	71.8 (4.92)	4.48 (0.307)
Inlet pressure, kPa (psi)	34,950 (5069)	224 (32.43)
Inlet temperature, K (°F)	1053 (1436)	300 (80)
Pressure ratio	1.192	1.231
Efficiency	0.821	0.85

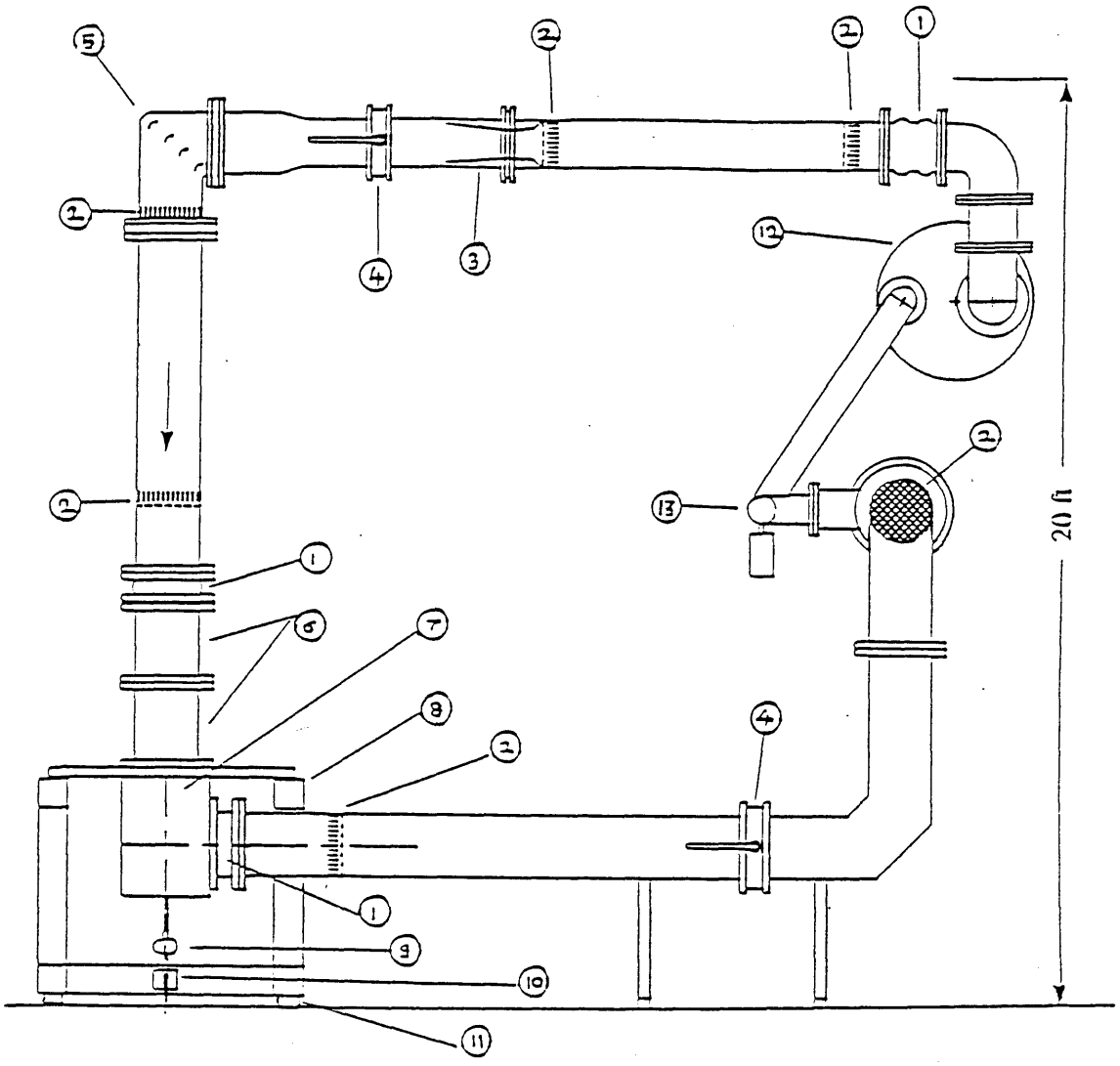

Fig. 3.1 Overall view of the Alford force test facility, front view. (1) Vibration isolator, (2) Flow straightener, (3) Venturi meter, (4) Throttle valve, (5) 90 degree bend with flow straightening vanes, (6) Turbine test section, (7) Exhaust plenum, (8) Test stand, (9) Flexible shaft coupling, (10) Pulley sprocket, (11) Vibration absorbing mounts, (12) Heat exchanger, (13) Servo driven by-pass valve

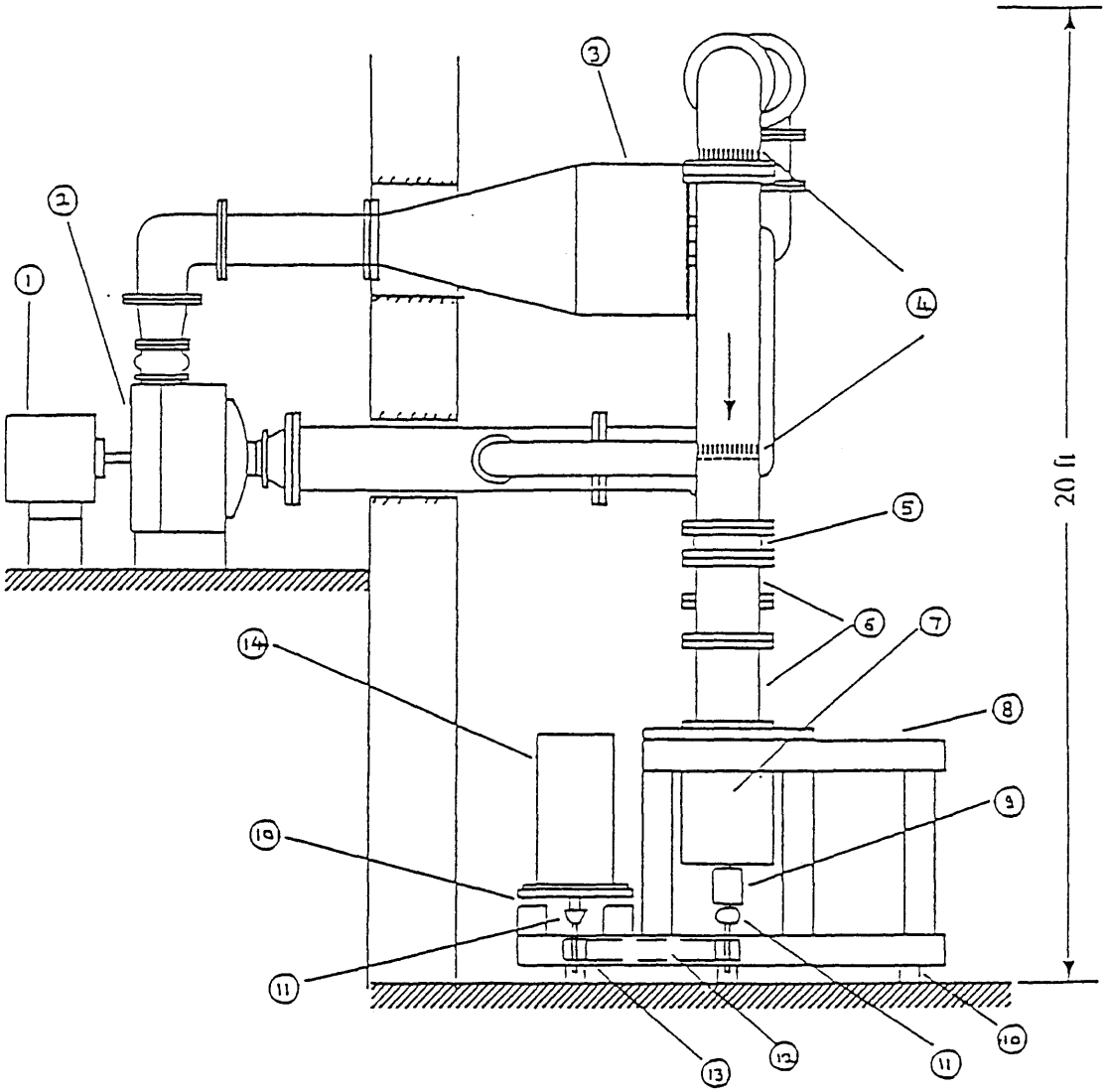

Fig. 3.2 Overall view of the Alford force test facility, side view. (1) 100 hp electric motor, (2) Compressor, (3) Heat exchanger, (4) Flow straightener, (5) Vibration isolator, (6) Test section, (7) Exhaust plenum, (8) Test stand, (9) Slipring assembly, (10) Vibration absorbing mounts, (11) Flexible shaft coupling, (12) Drive belt, (13) Pulley sprocket, (14) DC motor/generator

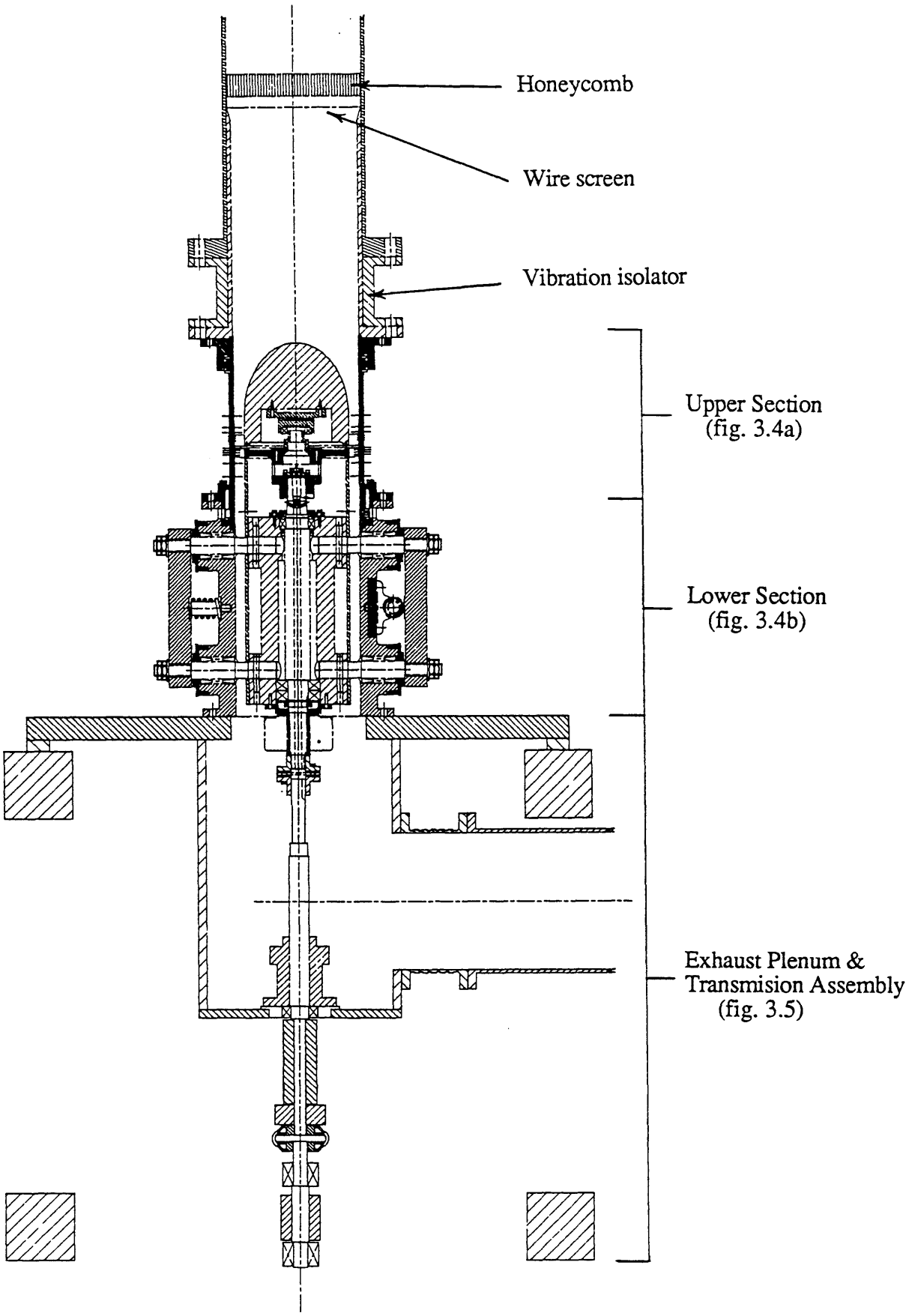

Fig. 3.3 Turbine test section and transmission assembly

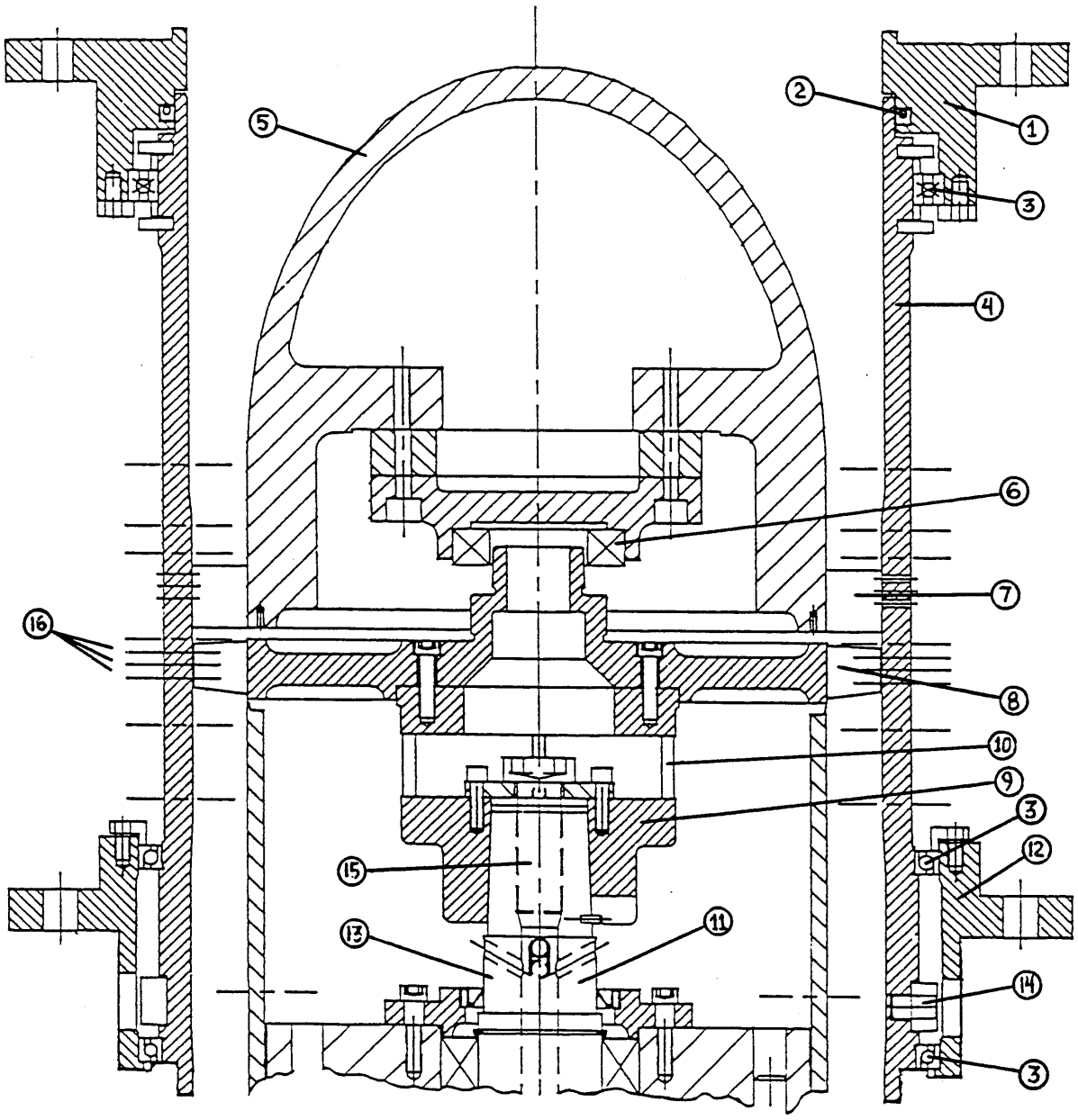

Fig. 3.4a Turbine test section, upper section. (1) Upper flange, (2) Rotatable casing seal, (3) Rotatable casing bearing, (4) Rotatable casing, (5) Ogive, (6) Electrically insulated snubber bearing, (7) Stator blades, (8) Rotor, (9) Rotating dynamometer, (10) Square posts where strain gauges are attached, (11) Upper drive shaft, (12) Lower flange, (13) Location of upper torque strain gauge bridge, (14) Chain for rotating casing, (15) Hollow shaft for instrumentation wires, (16) Three axial locations for stator retaining screws

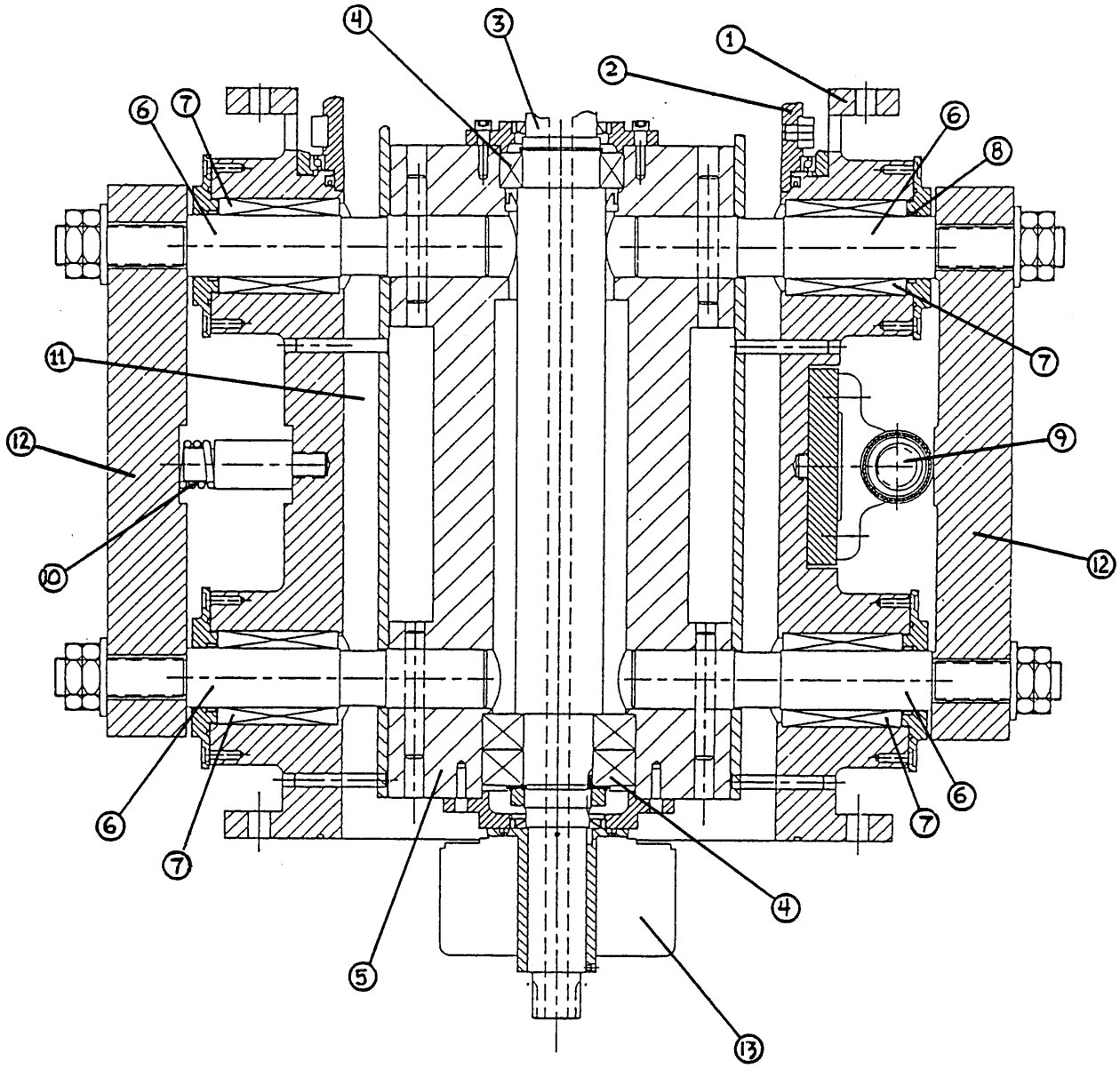

Fig. 3.4b Turbine test section, lower section. (1) Upper flange, (2) Rotatable casing, (3) Upper drive shaft, (4) Upper drive shaft bearings, (5) Bearing housing, (6) Movable struts, (7) Linear bearings, (8) Strut seal, (9) Eccentric cam mechanism, (10) Spring, (11) Flowpath, (12) Strut connecting bars, (13) Optical encoder

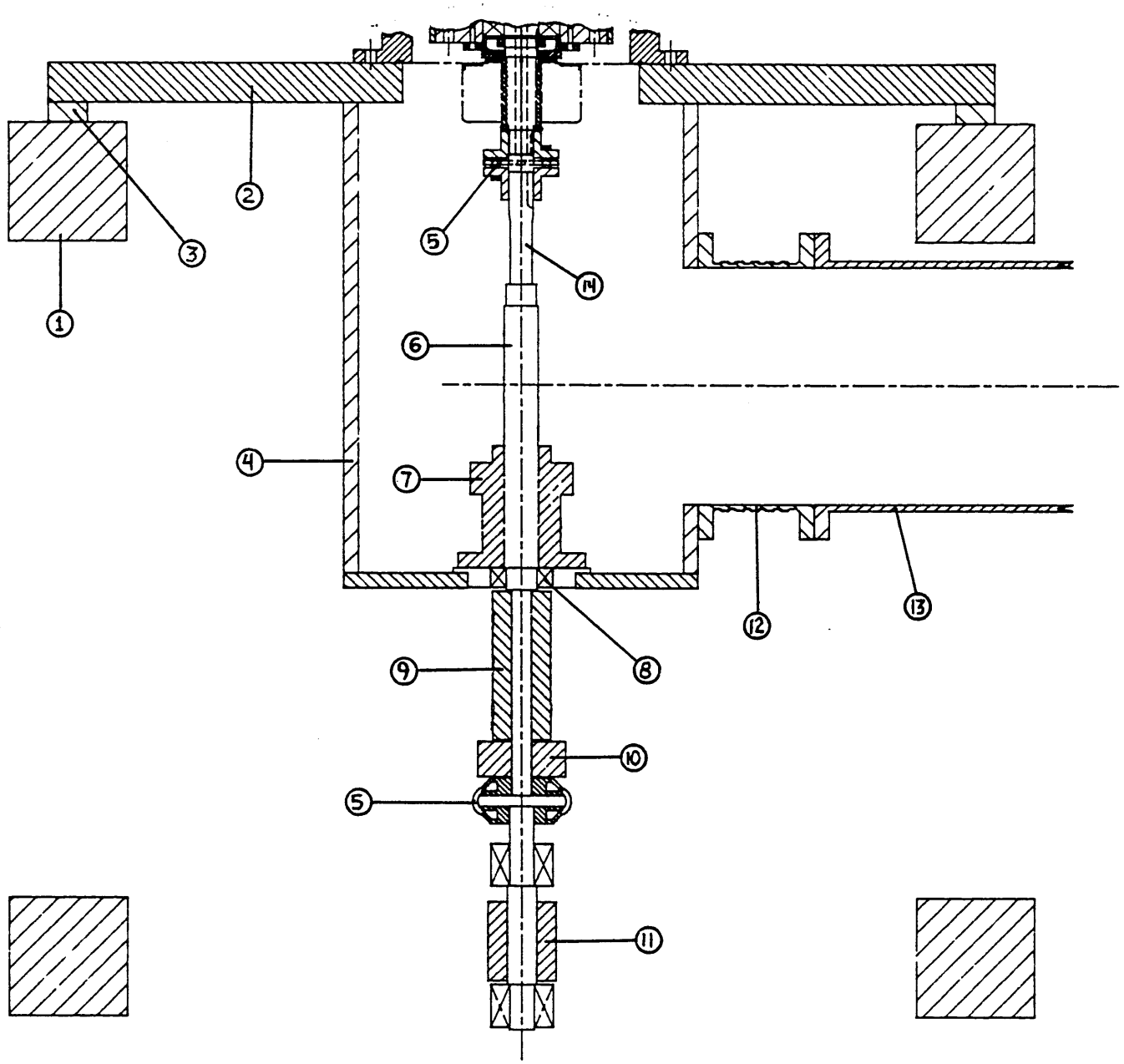

Fig. 3.5 Exhaust plenum and transmission assembly. (1)Test stand, (2) Test section support plate, (3) Shims, (4) Exhaust plenum, (5) Flexible coupling, (6) Lower drive shaft, (7) Rotaing seal, (8) Lower drive shaft bearing, (9) Slipring, (10) Instrumentation wire connection cup, (11) Drive belt pulley, (12) Vibration isolator, (13) PVC pipe, (14) Location of lower torque strain gauge bridge

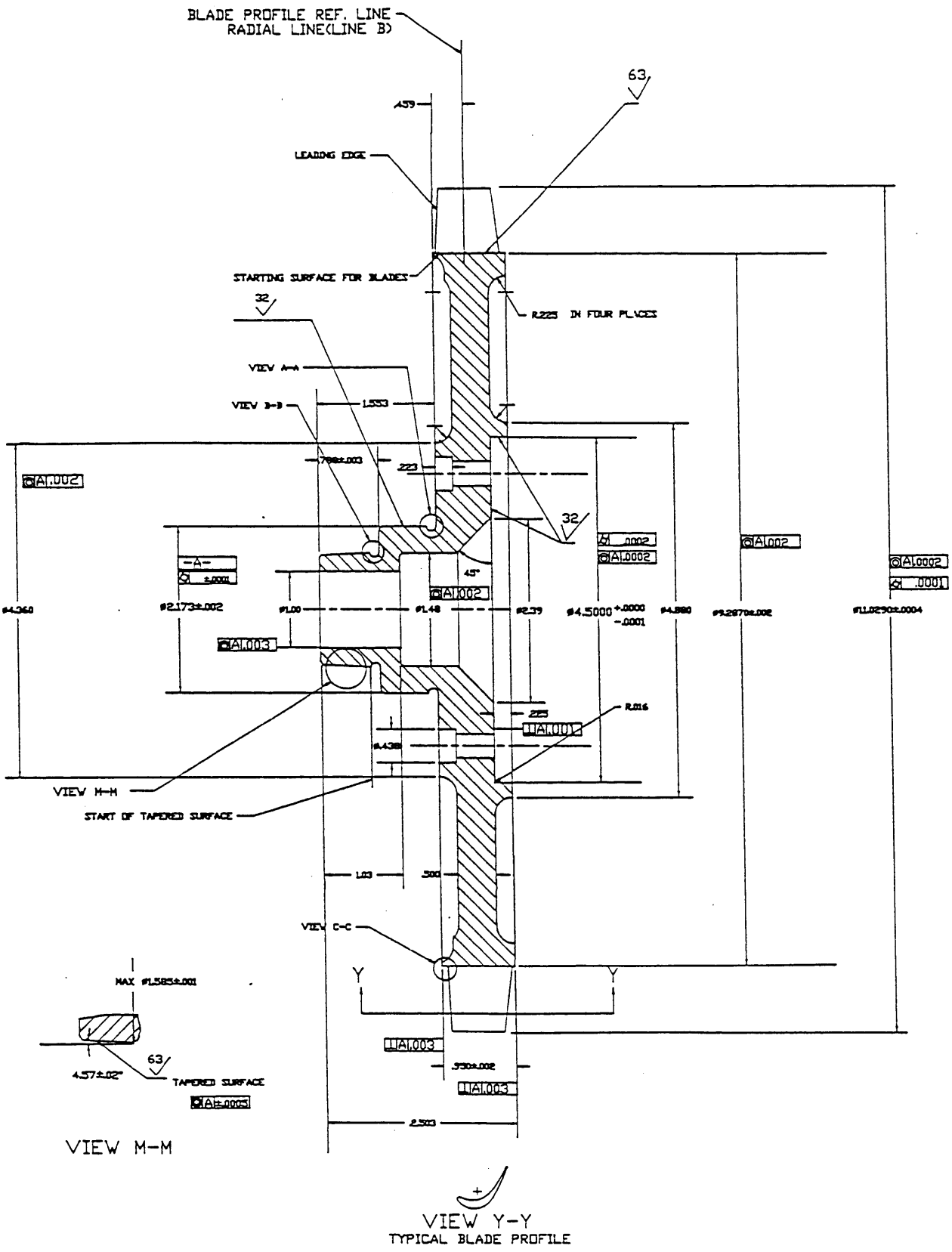

Fig. 3.6 Machine drawing of turbine test rotor

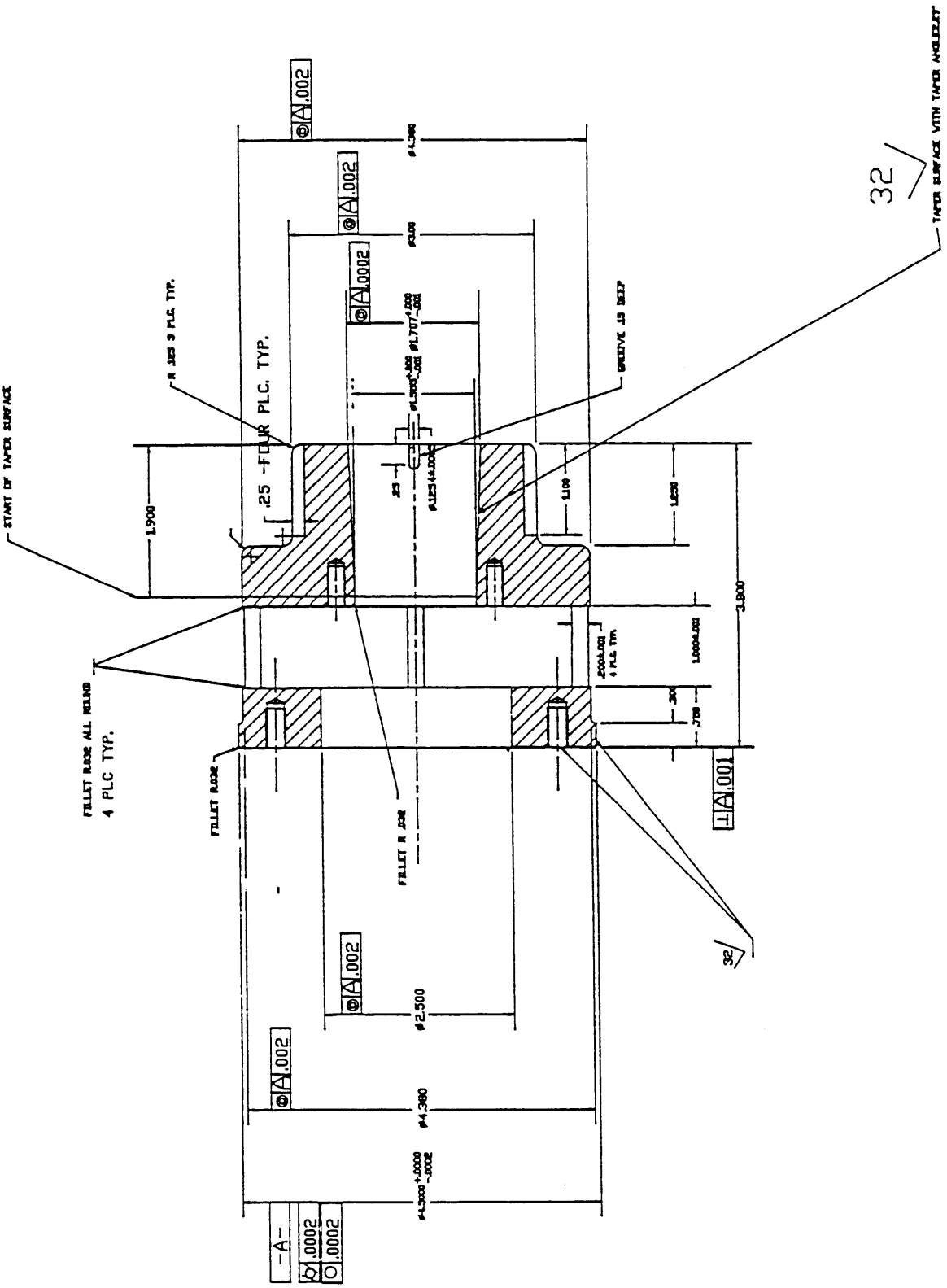

Fig. 3.7 Machine drawing of loadcell

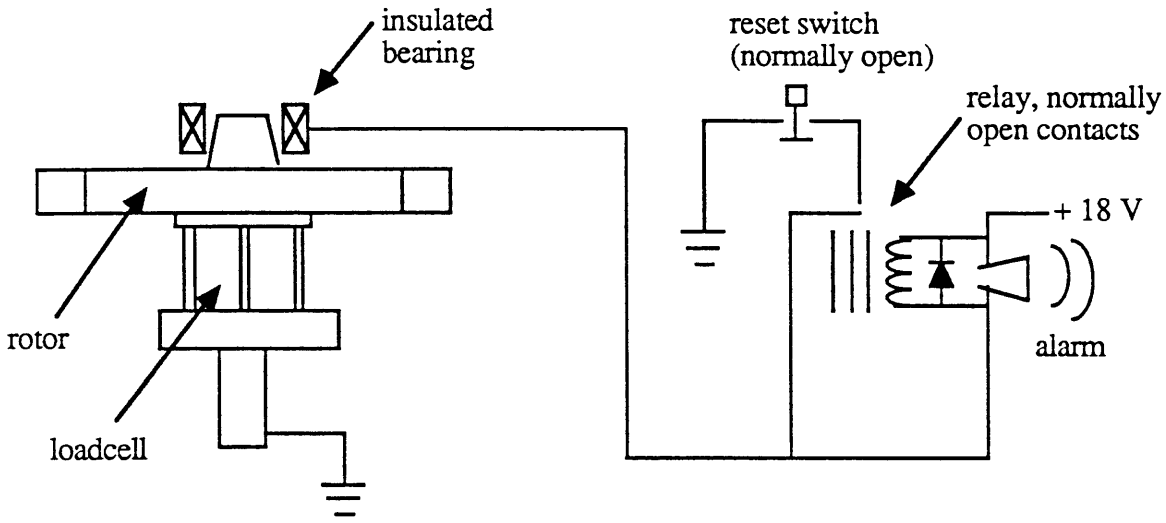

Fig. 3.8 Snubber alarm electrical schematic

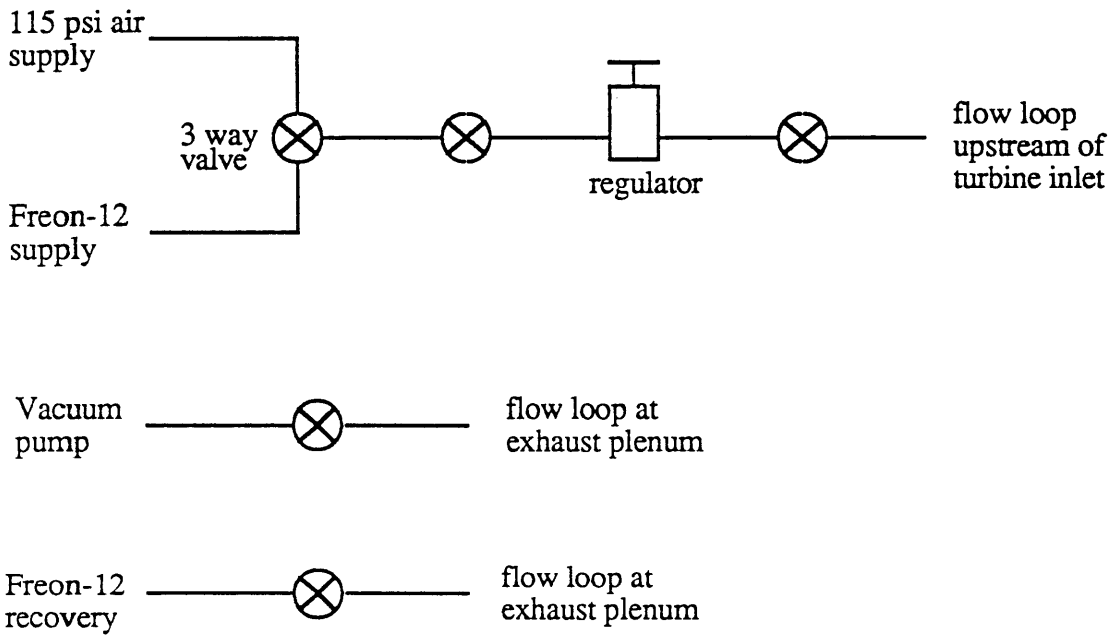

Fig. 3.9 Flow loop pressurizing and evacuation plumbing

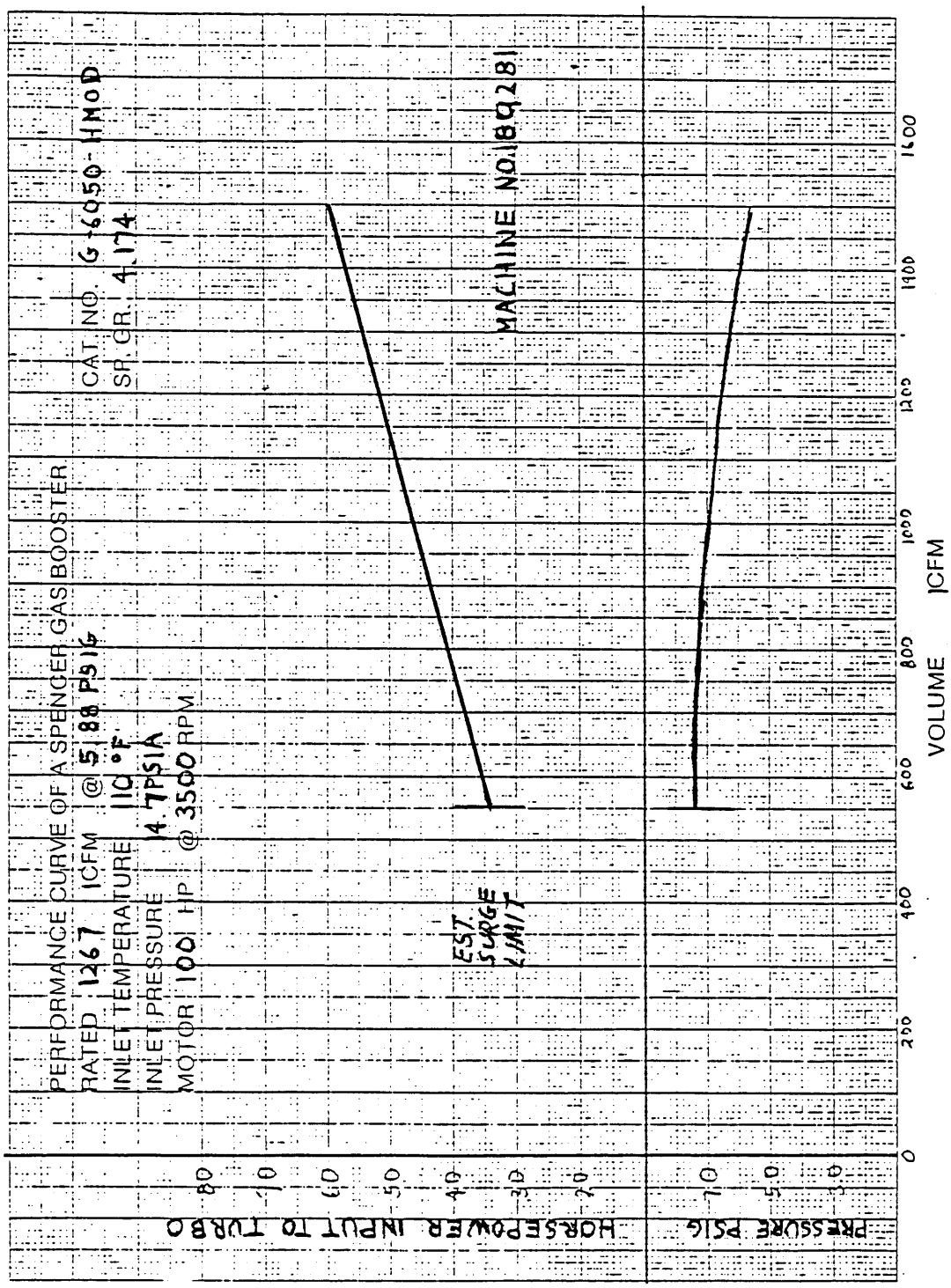

Fig. 3.10 Performance curve for Spensor compressor with Freon-12 at 14.7 psi inlet pressure

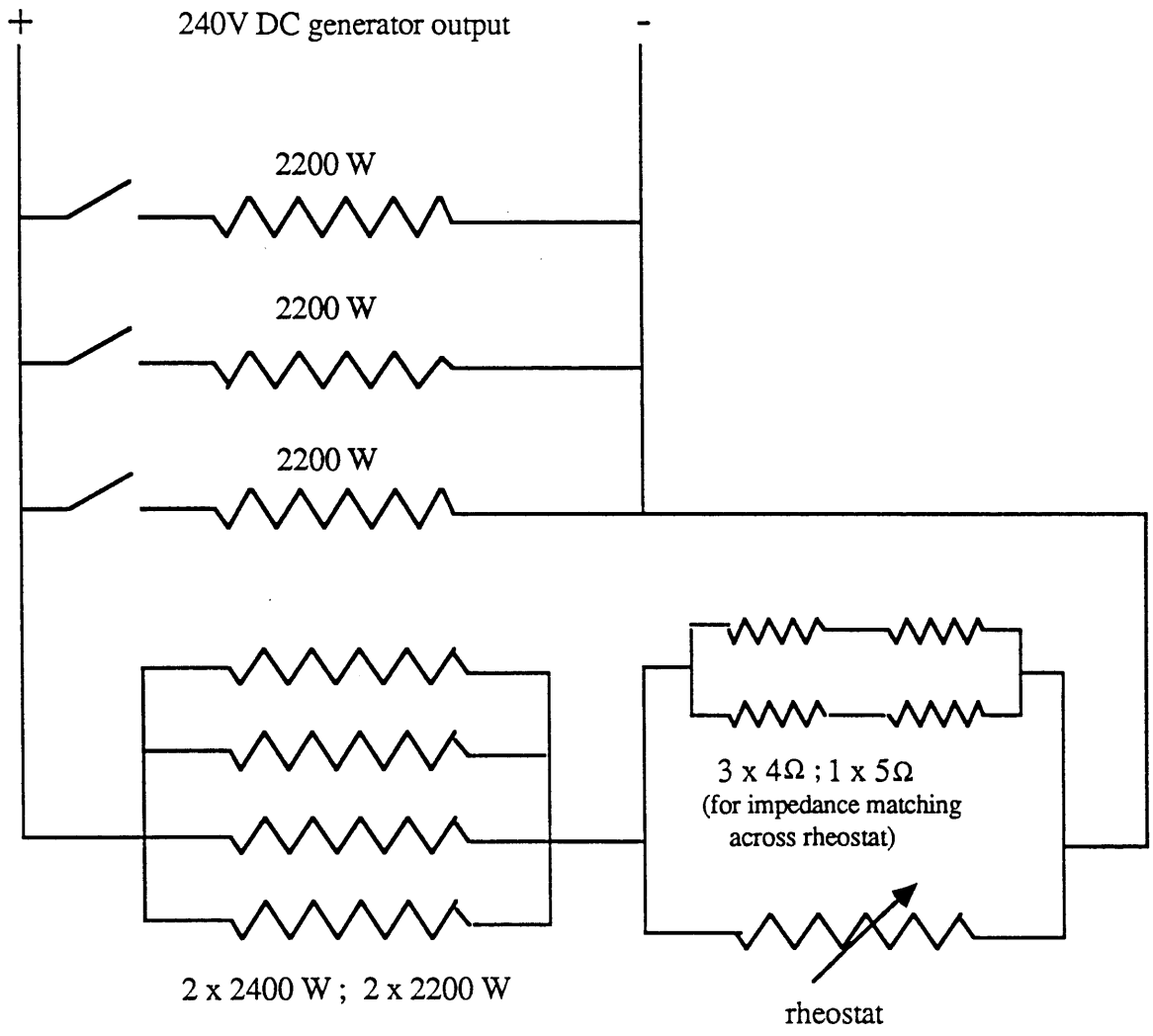

Fig. 3.11 Turbine power dissipation system

CHAPTER 4

INSTRUMENTATION

The instrumentation and data acquisition used for the measurement of Alford forces and flow parameters will be reviewed in this chapter. The instrumentation for this facility includes a rotating dynamometer for rotor force measurements and various pressure probes, thermocouples and pressure transducers for flow measurements. Data from these are digitized by one of three different A/D systems and then stored on computer disks for later processing. All processes of data acquisition are controlled by computer through various software packages.

4.1 Rotating Dynamometer

4.1.1 Design

The main emphasis of the experimental work for this thesis was identifying and measuring the Alford force. To this end, a rotating dynamometer attached to the turbine rotor capable of measuring all components of force and moment acting on the rotor was designed and built. Because the rotor is connected to the drive shaft directly through the rotating dynamometer all forces felt by the rotor are measured by the dynamometer. Also, because the dynamometer is rotating all forces measured must be converted from the rotating frame to an inertial reference frame.

As explained in the previous chapter the rotating dynamometer consists of four stainless steel square posts equally spaced which are parallel to the rotor axis at a radius of 0.053 m (2.1 in.). The posts are 0.005 m (0.2 in.) on the side and 0.0254 m (1.0 in.) in length and are instrumented with nine sets of full Wheatstone bridge strain gauge sets. The size and material

were determined by calculating the expected lateral rotor forces and then sizing the posts to strain enough to enable measurement of the minimum expected force (0.4 N operating at 50% of full power) with 10% accuracy while still safely supporting the rotor.

The orientation of the nine sets of full Wheatstone bridge strain gauge sets on the posts is shown in figure 4.1 and the primary sensitivities of each bridge are shown in figure 4.2. All of the bridges, except one, are primarily sensitive to two components of force or moment. The exception is bridge no. 9 which is primarily sensitive to thrust only. The bridges also respond to the other four (or five) force and moment components. These secondary sensitivities are one to two orders of magnitude smaller, however, than its primary responses and are accounted for in the calibration as will be explained in the next section. Semi-conducter gauges are used in order to maximize sensitivity and dynamic response which is necessary due to the relatively small dynamic forces that are generated. These gauges cannot be used for DC measurement, however, due to their large drift rates.

The wiring of the dynamometer required the use of four sets of 10 conductor shielded cable. The wires are connected at the dynamometer by soldering strips and then covered with epoxy to assure a firm connection even under running conditions. The 10 conductor wires then are routed from the solder strips through the center of the dynamometer and through the hollow center of the upper and lower drive shafts. The wires exit at the bottom of the lower drive shaft where they are routed to an aluminum cup which spins with the shaft. The cup provides access to make wire connections but then can be covered to provide protection for the wires while the turbine is operating

Since the wires are rotating with the shaft, a slipring is necessary. The strain gauge wires are soldered and insulated from ground inside the aluminum cup. The slipring rotor is keyed to the lower drive shaft and the housing is pinned to the aluminum exhaust plenum.

The wires from the slipring are then routed to a terminal box which is mounted on the front side of the discharge plenum. The terminal box has two purposes: First, it provides a place to connect zeroing potentiometers across one leg of each of the nine bridges. The zeroing

potentiometers are used to initially zero the output of each bridge under no load conditions. The second purpose of the terminal box is to provide a place to connect all of the strain gauge wiring to extension wires which are routed across the room to the instrumentation rack. A four pin receptacle is provided for each of the nine bridges.

Power and signal conditioning for the strain gauge bridges is provided by nine strain gauge conditioning amplifiers, model numbers 2310 manufactured by Measurements Group, Inc. The excitation was set at 10V and gain set at 100 for bridges 1 to 8 and 50 for bridge 9. Since numerous samples over several rotor revolutions were acquired and averaged, which provides excellent noise filtering, the analog filter on each amplifier was set at wide-band. The amplifiers also have built-in AC coupling which was used to reduce the DC component of the signals since the only data of interest was the dynamic signal.

The strain gauge conditioners also provide an active "guard" connection in addition to chassis ground to reduce electrical noise pick-up from the extension wires . The extension wires have an inner and outer shield. The inner shield is connected to the amplifier's active guard and the outer shield is connected to chassis ground. Both shields are disconnected and insulated from ground at the gauge end.

4.1.2 Calibration

The objective of the dynamometer calibration was to produce a six-by-six matrix, [B], which, when multiplied by a six component voltage vector made up of six bridge voltages would result in a six component force vector made up of the three components each of force and moment acting on the dynamometer. The force vector is found from the relation

$$\{f\} = [B]\ \{V\}$$

where $\{f\}$ is the six component force vector and $\{V\}$ is the six component voltage vector.

The matrix [B] is the inverse of the bridge slope matrix, [S], which is simply the slope of the voltage output by each bridge for each of the six components of force and and moment acting on the dynamometer. The slope matrix includes the effects of all forces and moments acting on each bridge, both primary and secondary sensitivities. If all of the effects are linear (which they were to certain extent in the range of expected force and moment magnitudes) all interactions will be taken into account and the force vector will represent the correct loading of the dynamometer.

Prior to calibration the continuity of all wiring and the resistance across the legs of all bridges was checked to ensure that all connections were correct. Also, raw voltage outputs from each bridge were recorded under known loading to determine amplifier gain values.

The elements of the slope matrix were then determined by loading six sets of individual force and moment loads and recording the responses of each bridge to the six individual loadings. The force and moment loads were applied through a system of pulleys and weights which was capable of applying both positive and negative loadings of all six force and moment components An dummy aluminum disk was bolted to the dynamometer in place of the rotor to apply the loads (see figures 4.3 and 4.4). The lateral forces, F1 and F2, consisted of 15 loadings from -2.2 to +2.2 N (-10 to +10 lbf), and the thrust force, P, consisted of nine loadings from zero to +11.2 N (0 to +50 lbf). The bending moments, M1 and M2, consisted of 17 loadings from -16.5 to +16.5 Nm (-146 to +146 in lb) and the torque, T, consisted of 9 loadings from zero to -22.6 Nm (0 to -200 in lbf). A typical calibration graph is shown in figure 4.5.

Two additional static tests were performed in order to evaluate the performance of the dynamometer. The first to determine hysteretic effects, if any, was to compare the response of the bridges under increasing and decreasing loadings. These tests showed that no significant errors were introduced by hysteretic effects. A second test was the response to combined loadings, such as lateral force and torque, to assure that both components could be resolved from the bridge voltages. These tests also proved successful.

Because the dynamometer is rotating with the rotor it was also necessary to determine its dynamic characteristics. To do this a cable was connected to the calibration disk through a lightly loaded pulley (see figure 4.6). This enabled a lateral force (representing the expected Alford force) to be applied to the dynamometer while it was spun with the DC motor. The signals were checked for several speeds ranging from 30 to 3500 rpm and for several loadings from zero to 44.5 N (10 lbf). The loading was reconstructed with the calibration matrix and the error in the lateral force measurement was found to be under 2% for all loadings and speeds.

4.1.3 Natural Frequency Considerations

In order to fully evaluate the performance of the dynamometer it was also necessary to perform some natural frequency tests. The natural frequencies of the system were determined by several different tests.

The first test was done by simply tapping the rotor in the lateral direction with a soft hammer and simultaneously recording the dynamometer voltages. A typical plot of the response of one bridge is shown in figure 4.7. Figure 4.8 shows the spectral response of the lateral force measured by the dynamometer after the hammer strike. Lateral natural frequencies of 105 Hz and 580 Hz are clearly seen.

A second test was a coast down test which was done by spinning the rotor with the DC motor and then switching off the armature power and recording the dynamometer response as the turbine spins through all speeds. This test was done with the flow loop under vacuum to minimize aerodynamic forces. The signal was then spectrally analyzed and a typical FFT plot is shown in figure 4.9. Natural frequency estimations of the drive system indicated a torsional natural frequency of vibration of the rotor and upper and lower drive shafts about the lower flexible coupling to be approximately 22 Hz (see fig. 4.10). The cost-down test confirmed this by indicating a torsional natural frequency at approximately 18 Hz.

4.2 Test Section Measurements

4.2.1 Test Section Instrumentation

The primary purpose of the test section instrumentation is to allow measurement of local flow variable distribution. As discussed in chapter 2, the argument that Alford gives for the generation of a lateral force is that the local efficiency of an eccentric turbine will vary linearly with the blade-tip clearance around the turbine circumference. He argues that the local efficiency at any azimuthal location of an eccentric turbine is that of a concentric turbine operating with a blade-tip clearance equal to the local blade-tip clearance at that azimuthal location. In order to evaluate this argument it is necessary to measure the azimuthal distribution of efficiency.

The test section is heavily instrumented with numerous provisions for several different pressure and temperature probes which allow measurement of turbine inlet and exit total pressure, total temperature and flow angle distributions. Other instrumentation includes numerous static pressure taps to allow detailed flow mapping in the blade-tip region and proximity probes which are used to determine the turbine rotor location relative to the casing at any given time. An instrumentation map is shown in figure 4.11.

The Pitot-static probe and thermocouple at station 0 are used primarily to monitor inlet pressure and temperature prior to and during test runs. Another function is to determine the turbine inlet velocity profile (see Appendix A) to determine if any inlet flow distortions exist.

Station 1 and station 9 are used to determine the flow conditions far upstream and downstream of the turbine. One assumption which Alford made in his argument [1] is uniform upstream and downstream flowfields. As mentioned in Chapter 2, his assumption may not be valid and this instrumentation provides a means to help determine this.

Station 2 and station 8 are used to determine the full 3-D flow pattern at the turbine inlet and exit. Again, this instrumentation is used to explore the effect that blade-tip clearance

variation has on the upstream and downstream flowfield as well as determination of the turbine operating point (stage pressure drop, inlet total pressure, etc.).

Station 3 and station 4 are used to measure the wall static pressure both upstream and downstream of the stator passage. Because the stator is fixed to and rotates with the turbine casing (see fig. 3.4a), there is no way to azimuthally traverse the stator passage. For this reason the static taps in stations 3 and 4 are arranged so that five static pressure taps are equally spaced in between two stator blades. With this arrangement measurements are possible at five azimuthal positions between stator blades.

Stations 5, 6 and 7 are located at the rotor blade-tips. Static pressure measurements can be made at each of these axial stations enabling determination of the azimuthal static pressure distribution at three axial locations of the rotor. Station 6 is also instrumented with two proximity probes located 90° apart which are used to measure the rotor position relative to the casing.

Station 10 consists of eight static pressure taps located far downstream on the inside diameter of the flowpath. Again, this station is used to measure the azimuthal static static pressure distribution far downstream from the rotor exit to see if flow variations at the rotor are carried far downstream.

Three different types of pressure/temperature probes are used. As mentioned earlier, a Pitot-static probe with a thermocouple for total temperature measurements at station 0 is used to monitor inlet flow conditions. The two other types of pressure/temperature probes used are 3-hole and 5-hole pressure probes with thermocouples. The probes were manufactured and acquired from United Sensor. The 3-hole probes are wedge type probes which indicate both static and total pressure, as well as yaw angle and total temperature. The 5-hole probes are prism shaped probes which measure static and total pressure, total temperature and yaw and pitch angles. Each individual probe was provided with calibration curves from he manufacturer.

Since the test section provides for nearly one hundred pressure measurements some type of pressure transducer multiplexer was necessary. A 48 channel double Scanivalve system, Scanivalve Corp. model number DSS-48C/MK4 was used. A 69 kPa (10 psid) transducer referenced to the inlet total pressure is connected to one side which is used to measure pressure variations across the turbine stage. A 6.9 kPa (1 psid) transducer is connected across the Scanivalve which is used to measure azimuthal pressure variations. Figure 4.12 shows a schematic of the Scanivalve set-up.

Recording Devices model SCSG/D±5V/VG signal conditioners provide 12V excitation and signal conditioning to the Scanivalve pressure transducers. The conditioners have variable gain with span and zero adjustments built in and provide a ±5V full scale analog output.

Other miscellaneous instrumentation includes two proximity probes to measure the rotor location relative to the casing, a Venturi meter to measure the mass flow, a tachometer, two visual pressure gauges to indicate loop pressure (or vacuum) and a volt meter connected across the DC motor/generator armature to indicate the armature voltage.

The pressure differential across the Venturi tube is measured with a 17 kPa (2.5 psid) transducer type PDCR 120/WL obtained from Druck Incorporated. It is a high accuracy transducer which is compatible with Freon on both the positive and reference sides.

The absolute inlet total pressure is measured with a type PDCR 900 200 kPa (30 psia) pressure transducer also from Druck. This provides an absolute measurement of the inlet total pressure to which other pressures are referenced.

4.2.2 Calibration

A single calibration system was used for calibration of all pressure transducers and a schematic is shown in figure 4.13. The system consists of a calibration tank, oil-free air pressure source, high accuracy pressure transducer and a series of valves for control.

The high accuracy pressure transducer is an MKS Instruments, Inc. model 398 Baratron differential transducer which has an accuracy of 0.08% of reading. The Baratron was originally calibrated against a dead weight pressure standard by the manufacturer. A 140 kPa (20 psi) relief valve is incorporated in the system to protect the Baratron against overpressure.

As stated in the previous section, the signal conditioners used for the Scanivalve pressure transducers have zero and span adjustment potentiometers. These adjustments were made first using the Baratron for span reference. The linearity of the transducers was then checked over the range of the transducer. The calibration was checked again several times and it was determined that the slope of the calibration line does not change significantly over time, however the zero offset does. For this reason the Scanivalve pressure transducers are zeroed before every day of testing.

The remaining pressure transducers do not have integral span and zero adjustments so the calibration procedure is slightly different. Pressure was applied over the range of the transducer and the voltages output at each pressure recorded. A calibration graph for each transducer was then generated. The slope and zero offset are then input in the computer software which automatically converts the raw voltages from the transducers to a pressure reading. Again it was determined that the zero offset should be adjusted before every day of testing.

The proximity probes were calibrated in place on the test section. The rotor was incrementally offset and the real time voltage outputs from the proximity probes were recorded while the rotor was spun at approximately 60 rpm. The minimum peak voltage (see figure 4.14) at each rotor offset was used to calculate a calibration line. A typical proximity probe calibration graph is shown in figure 4.15.

The calibration for the Venturi meter was provided by the manufacturer. However, the calibration provided was for volume flow of water versus pressure differential. This required some modification to convert to mass flow of Freon versus pressure differential. Also,

standard Mach number correction factors for Venturi meters were calculated, but because the Mach no. in the Venturi is low (less than 0.1) the correction factors are negligible.

Both strain gauge torque bridges were calibrated using the system of pulleys and weights used for the dynamometer calibration. The torque was varied from zero to 22.6 Nm (0 to 200 in lbf) while the rotor shaft was locked from rotating. The bridge output voltages were recorded and calibration lines calculated. A typical calibration graph is shown in figure 4.16.

4.3 Data Acquisition

The acquisition of data from all the sources mentioned above requires the use of analog to digital converters and a computer for control and storage. An IBM PC-AT computer was used with three different A/D systems to convert the voltage outputs from the various transducers into a digital signal. The digital signals are then read and stored on disk for later analysis. A flow chart of data acquisition is shown in figure 4.17.

The A/D used for the rotating dynamometer strain gauge bridges, upper strain gauge torque bridge and proximity probes is a LeCroy model 8212A 32 channel simultaneous sampling data logger. The 8212A provides for up to 32 analog inputs (12 are currently used) which are sampled simultaneously at a rate up to 5kHz (faster with less than 32 active channels) and has 12 bit (0.025%) resolution.

The clock and trigger signals for the 8212A data logger come from the optical encoder which is keyed to the rotor drive shaft. This provides a means to phase-lock average the signal since data acquisition will occur at the same rotor angular locations regardless of any rotation speed variations. The optical encoder provides both a 4096 per revolution TTL pulse signal used for clocking as well as a once-per-revolution TTL pulse for zero reference. A circuit was designed and built (schematic shown in figure 4.18) to divide the 4096 per revolution signal into a 256, 128, 64 or 32 per revolution signal. A secondary circuit was also necessary

(schematic shown in figure 4.19) to invert the clock signal so that the clock and zero reference signals would be in phase. Generally, the 32 per revolution signal was used to maximize the number of rotor cycles during data acquisition. The once per revolution signal was used to trigger the data acquisition. This assured that the data acquisition started at the same rotor angular position on every test.

The data are initially stored as acquired in LeCroy model 8800A dynamic memory modules. Four modules are used each having a capacity of 32,768 12-bit data words for a total capacity of 128K data words. As currently set-up with 12 input channels and a clocking rate of 32 samples per revolution, this is enough memory to acquire data over 256 rotor revolutions which at 3000 rpm takes approximately five seconds. The data can then be transferred from the 8800A memories to the computer through an IEEE-488 interface and then stored on disk for later analysis.

All operations of the 8212A data logger are controlled by the computer also through the IEEE-488 interface. Waveform-Catalyst software is used which was obtained directly from LeCroy. This software provides control, display and storage of all acquired data.

The outputs from the Scanivalve pressure transducers are interfaced to the computer through a Scanivalve Digital Interface Unit (SDIU) also obtained from Scanivalve Corp. The SDIU has several capabilities. First, it has a two channel A/D to which the pressure transducer signal conditioner outputs can be directly connected. The SDIU also has internal memory for pressure data storage. This is desirable because data can be acquired and stored without computer interaction during testing when the computer is busy with other tasks and then read and stored on disk at a later time. For interaction with the computer the SDIU has a standard IEEE-488 connection. Finally, the SDIU is used to control the position of the Scanivalve. The Scanivalve can be instructed to single step or scan continuously from the front panel or remotely from the computer. Remote operation from the computer also provides the ability to program the Scanivalve which provides more flexibility in its operation.

The third A/D system used is a high resolution plug-in interface card which is installed directly into a peripheral slot of the computer. This system is used for thermocouple inputs, the lower torque strain gauge bridge, the Venturi pressure transducer and the inlet absolute pressure gauge. The interface card, model WB-AAI-B16 obtained from Omega Engineering, Inc, has high 16 bit (0.0015%) resolution which is necessary for thermocouple measurements in order to resolve the relatively small azimuthal temperature variations which are on the order of 0.4 degrees C (0.8 degrees F)

The operation is controlled through software which was also obtained from Omega. The data acquisition rate is controlled by an internal clock and triggering is done manually from the computer keyboard. Data is first acquired into memory and then directly transferred to disk for storage.

Data processing is done with Asystant™ data processing software obtained from Asyst Software Technologies, Inc. This software has numerous capabilities for post data processing including FFT, curve-fit routines, statistics and others. The specifics of post data analysis used for this thesis will be discussed in the next chapter.

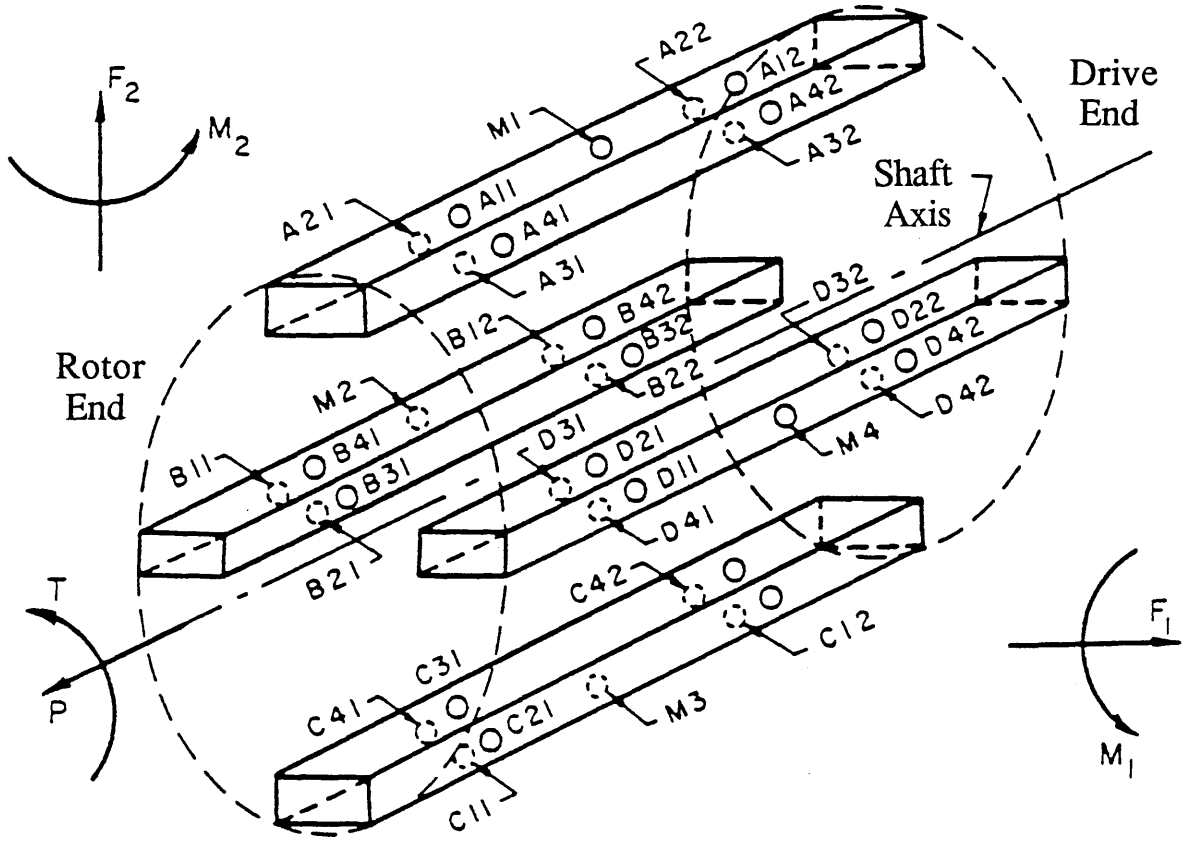

Fig. 4.1 Sketch of dynamometer measuring section consisting of four posts A, B, C and D and 9 strain gages per post: 4 at quarter length, XK1, 1 at mid-length, MK and 4 at three-quarter length, XK2. Forces and moments shown are defined as acting on the rotor, at the rotor end of the dynamometer [*8*].

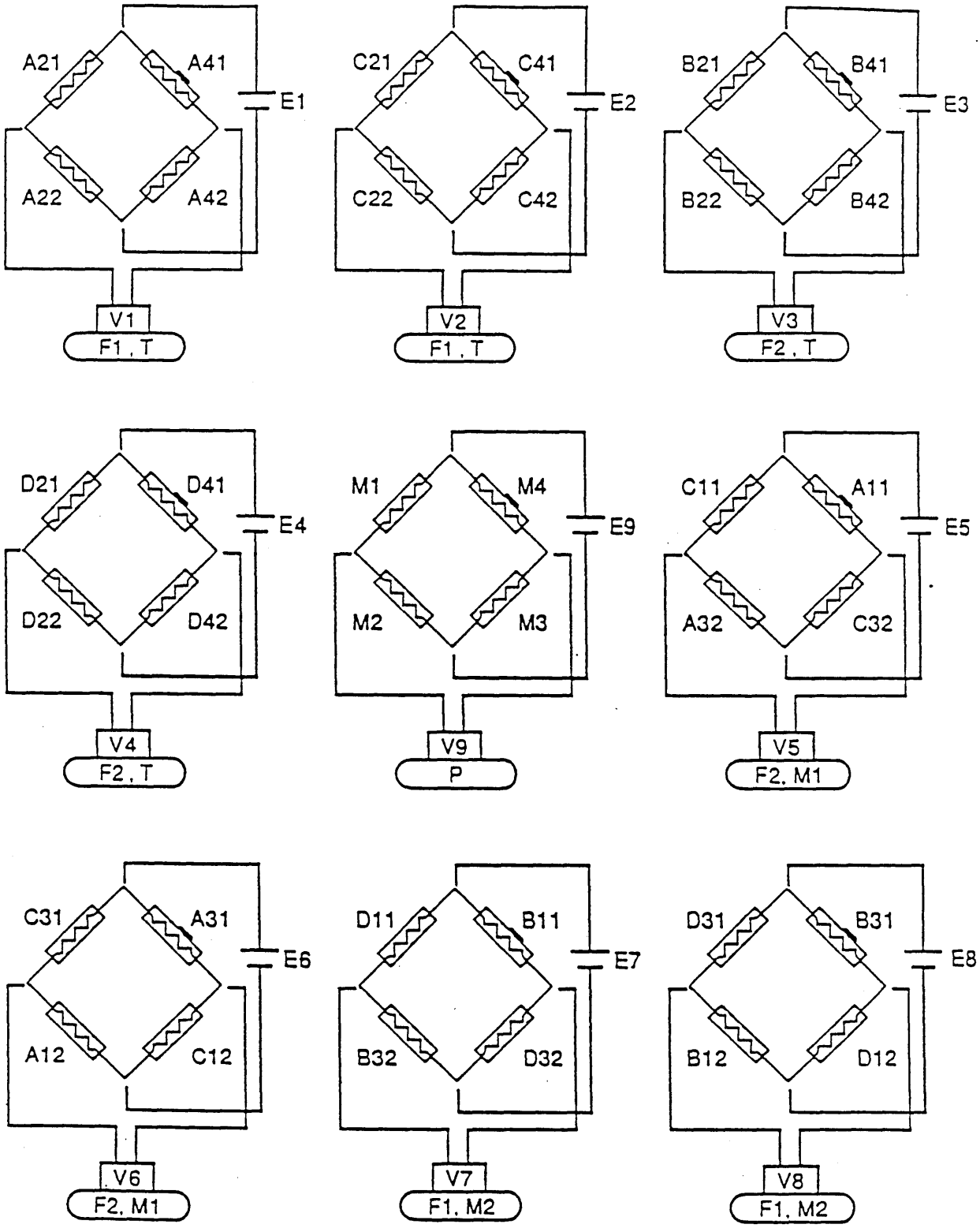

Fig. 4.2 Arrangement of the 36 semi-conductor strain gages in nine Wheatstone bridges showing bridge excitation voltages, E1 through E9, and bridge output voltages, V1 through V9. Each bridge is primarily sensitive to one or two of the six components of force and moment as indicated in the oval box below the bridge output voltage symbol.

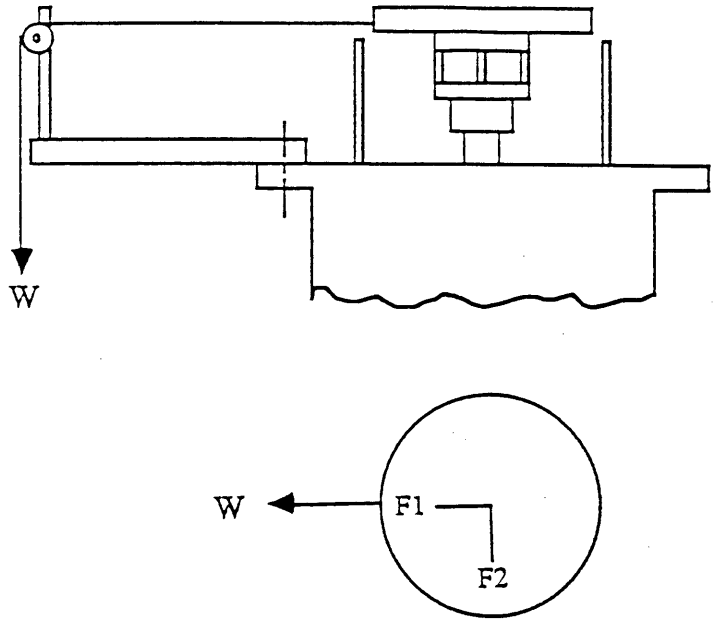

i) F1 and F2 Loading

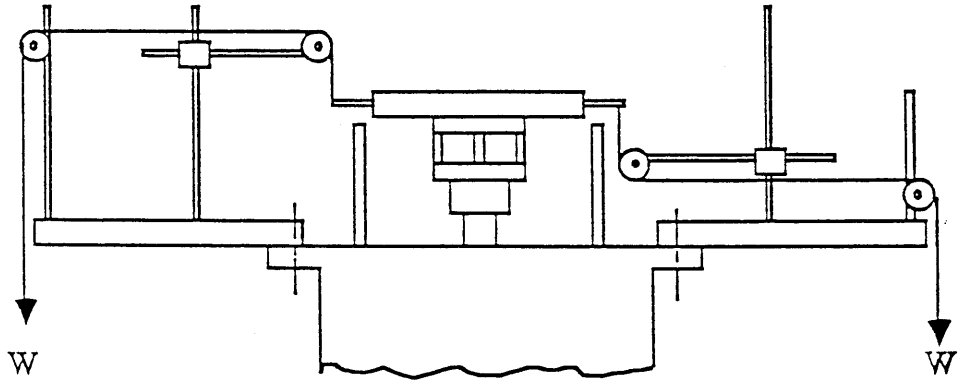

ii) M1 and M2 Loading

Fig. 4.3 Arrangement of weights and pulleys used to apply individual forces and moments on the calibration disk during dynamometer calibration

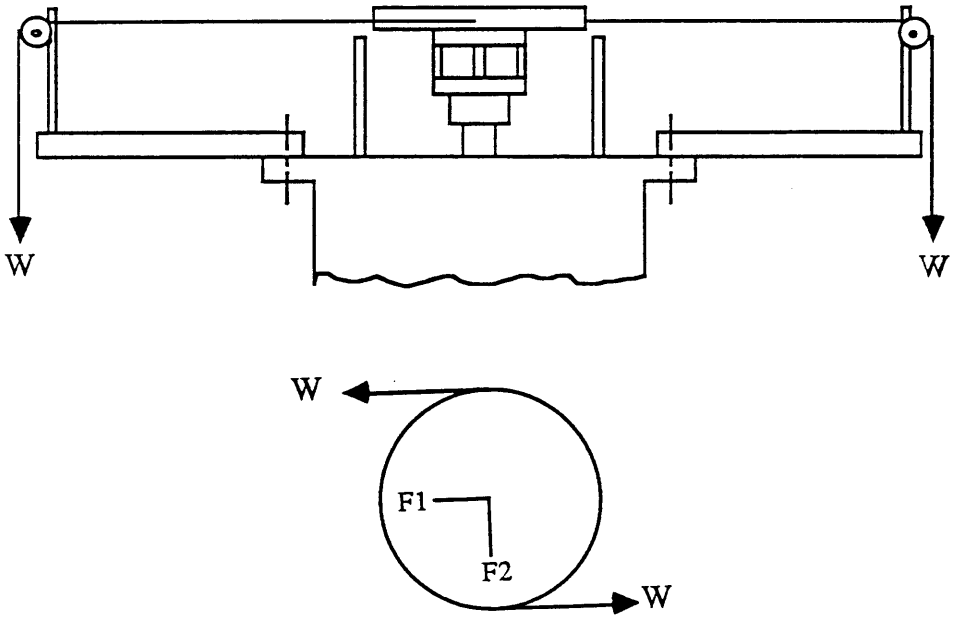

iii) Torque Loading

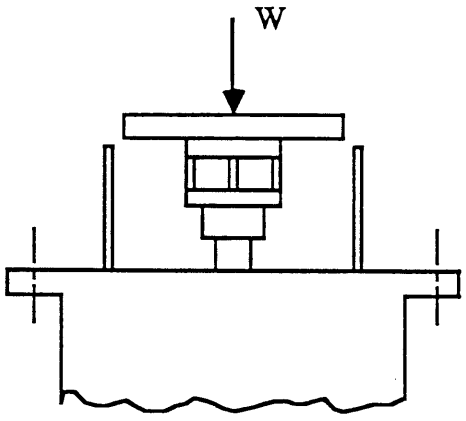

iv) Thrust Loading

Fig. 4.4 Arrangement of weights and pulleys used to apply individual forces and moments on the calibration disk during dynamometer calibration

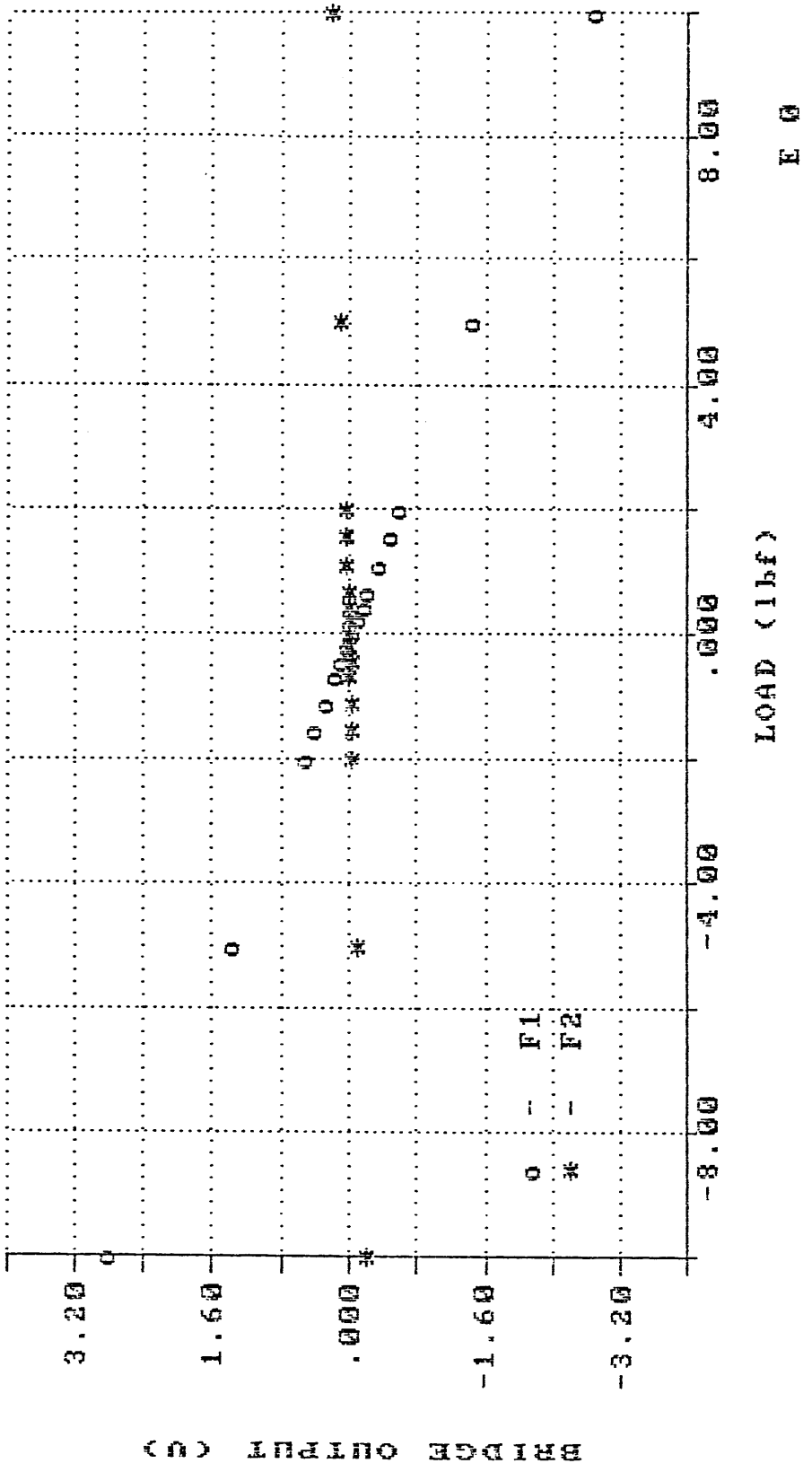

Fig. 4.5 Typical dynamometer static calibration graph. Shown is bridge 7 versus F1 and F2.

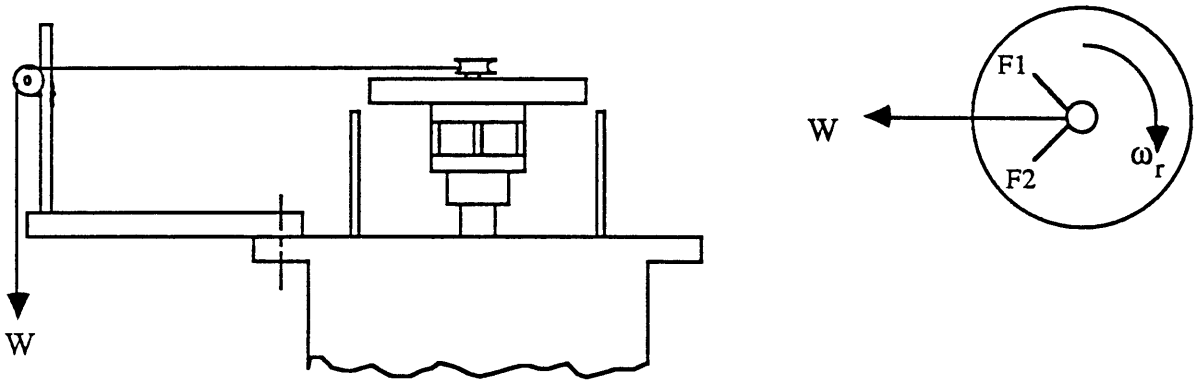

Fig. 4.6 Arrangement of weights and pulleys used to apply a lateral force on the calibration disk during dynamic dynamometer tests

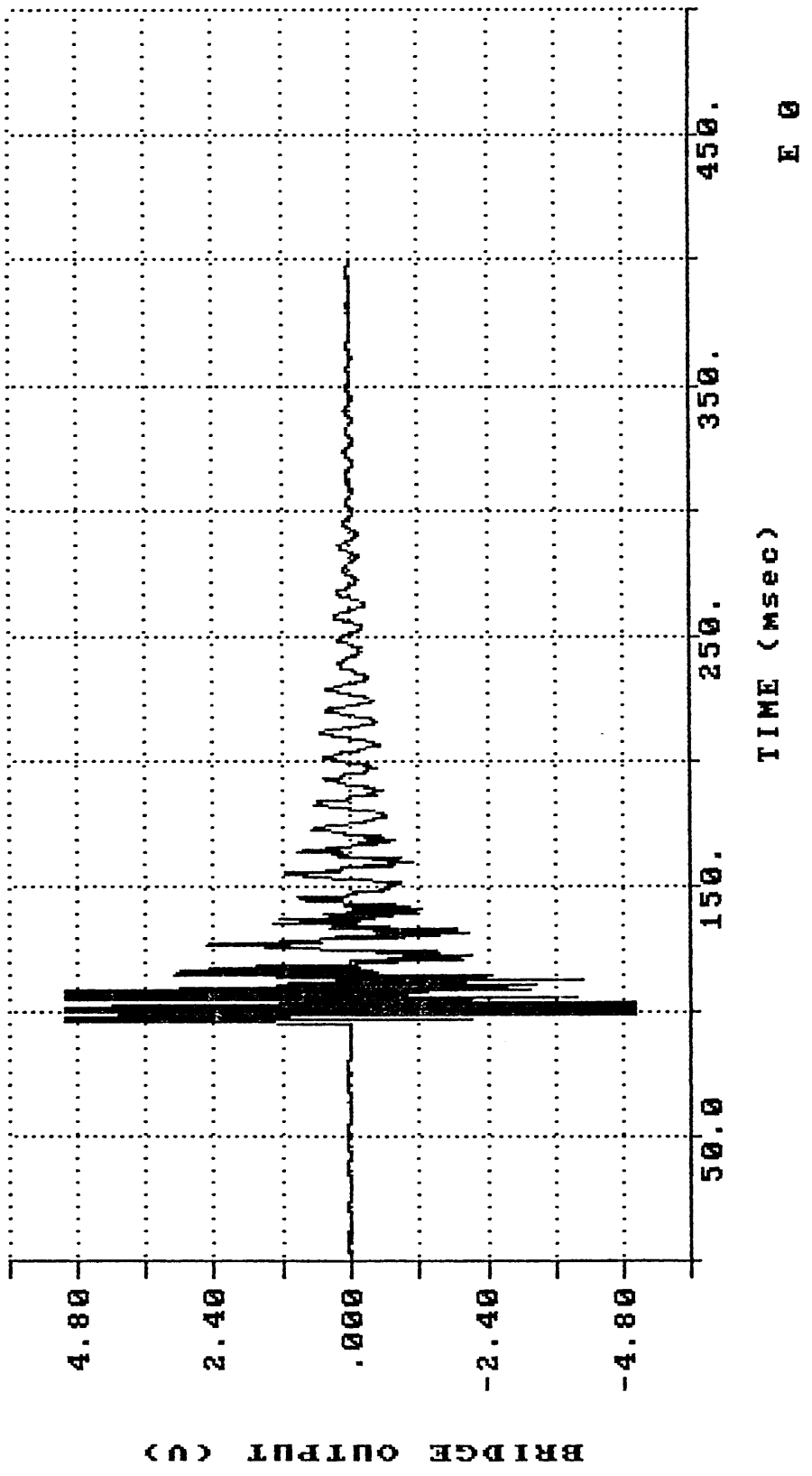

Fig. 4.7 Plot of bridge 1 voltage output versus time after lateral impulse load (hammer strike).

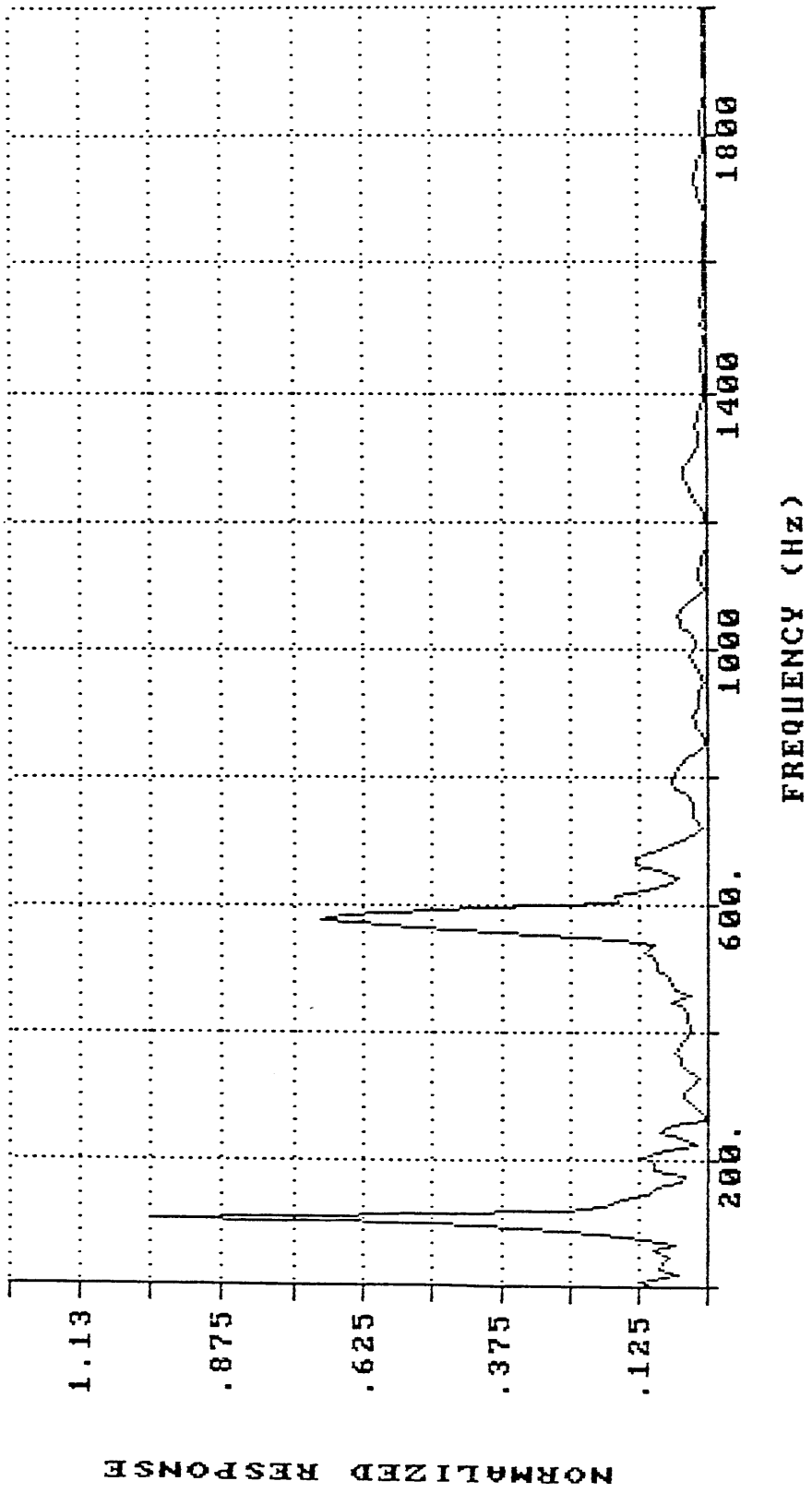

Fig. 4.8 Spectral plot of lateral force response after impulse load (hammer strike) showing lateral natural frequencies of 105 Hz and 580 Hz

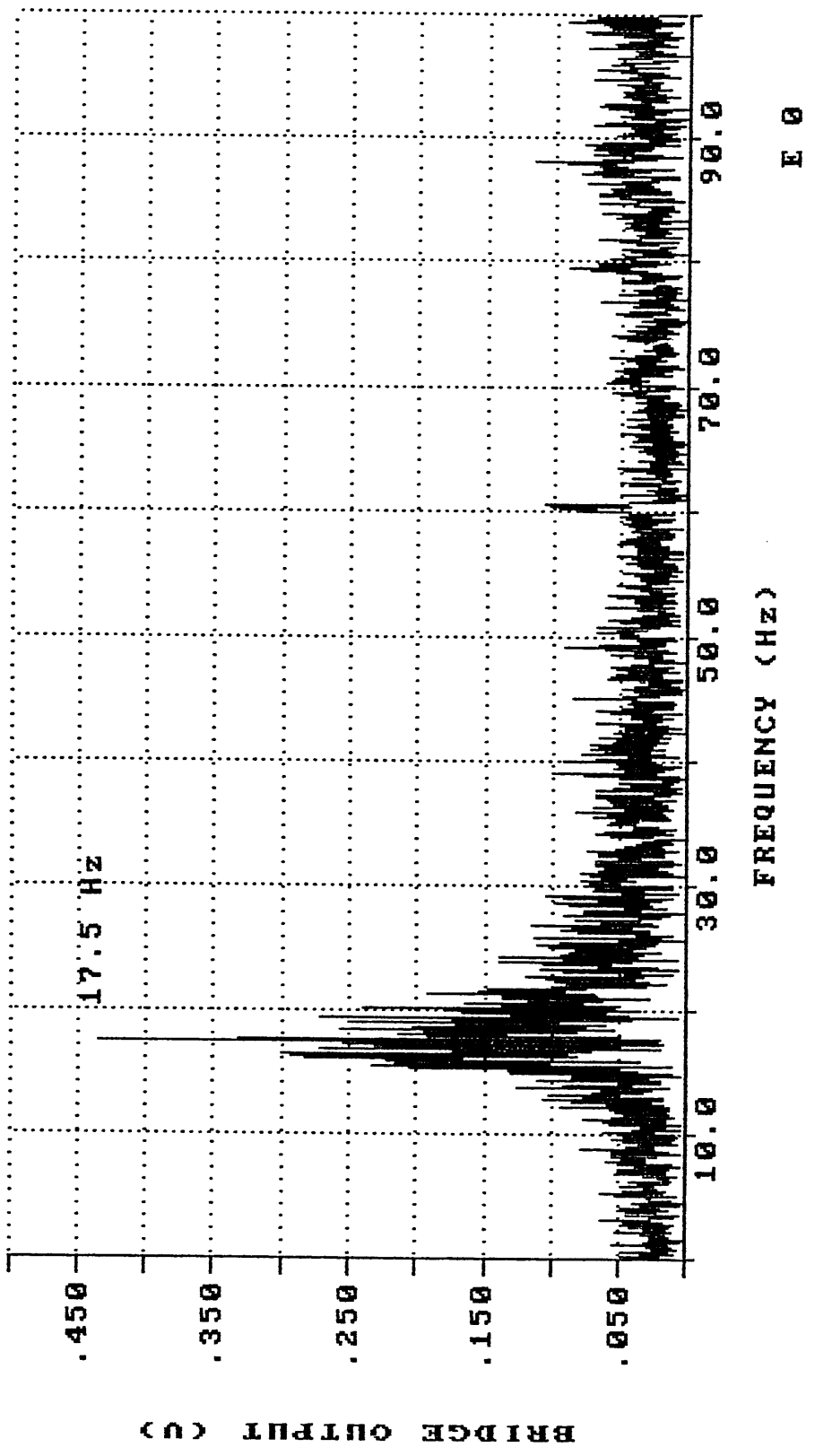

Fig. 4.9 Typical spectral response of bridge output voltage during coast-down test

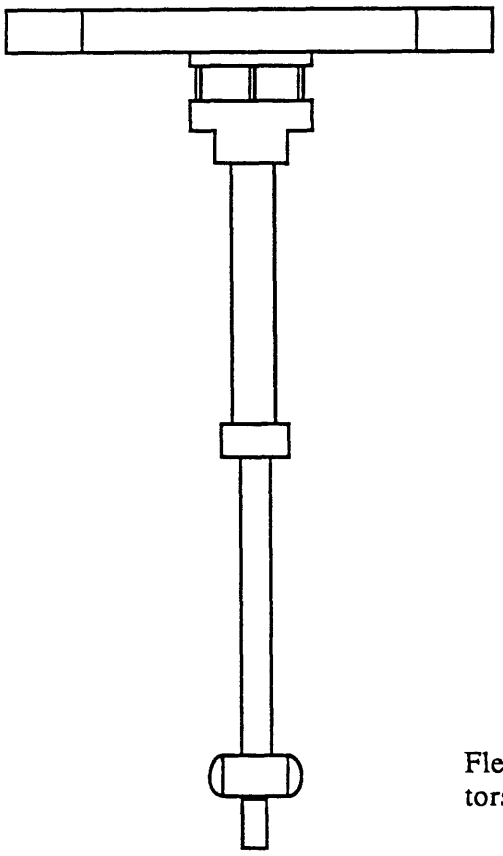

Fig. 4.10 Schematic of components used in natural torsional natural frequency calculation

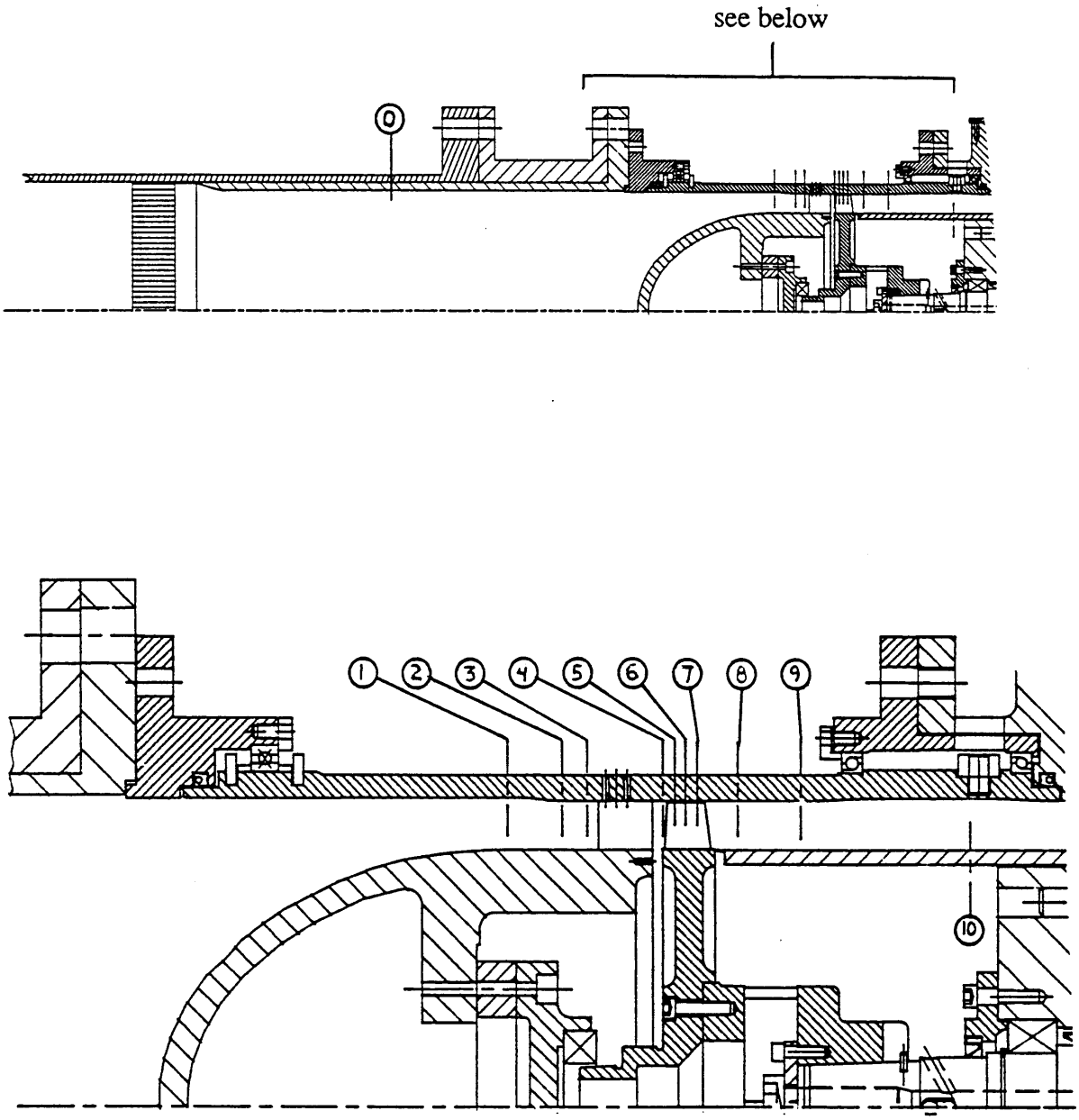

Fig. 4.11a Axial instrumentation station locations

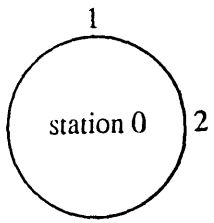

1, 2 pitot-static probe, thermocouple
- •total and static pressure
- •total temperature

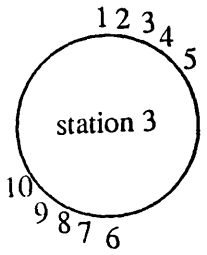

1 - 10 wall tap
- •static pressure

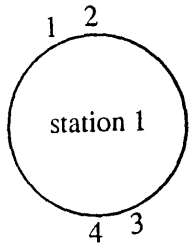

1, 3 3-hole wedge probe
- •total and static pressure
- •yaw angle

2, 4 wall tap
- •static pressure

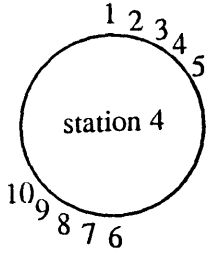

1 - 10 wall tap
- •static pressure

1 5-hole probe, thermocouple
2 traversing 5-hole probe, thermocouple
- •total and static pressure
- •total temperature
- •yaw and pitch angle

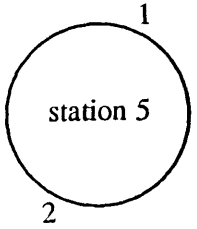

1, 2 wall tap
- •static pressure

Fig. 4.11b Instrumentation map

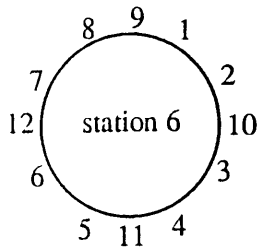

1 - 8 wall tap
- •static pressure

9 - 12 proximity probe
- •rotor position relative to casing

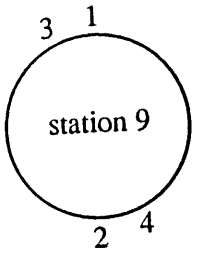

1, 2 wall tap
- •static pressure

3 3-hole probe, thermocouple

4 traversing 3-hole probe, thermocouple
- •total and static pressure
- •total temperature
- •yaw angle

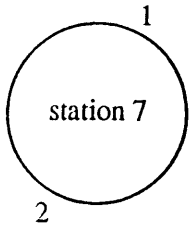

1, 2 wall tap
- •static pressure

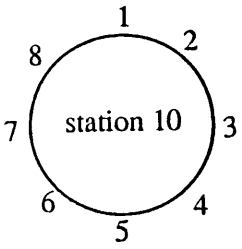

1 - 8 wall tap
- •static pressure

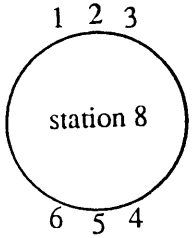

1 5-hole probe, thermocouple

2 traversing 5-hole probe, thermocouple
- •total and static pressure
- •total temperature
- •yaw and pitch angle

2, 5 hot-wire probe
- •flow velocity

3, 6 wall tap
- •static pressure

Fig. 4.11c Instrumentation map

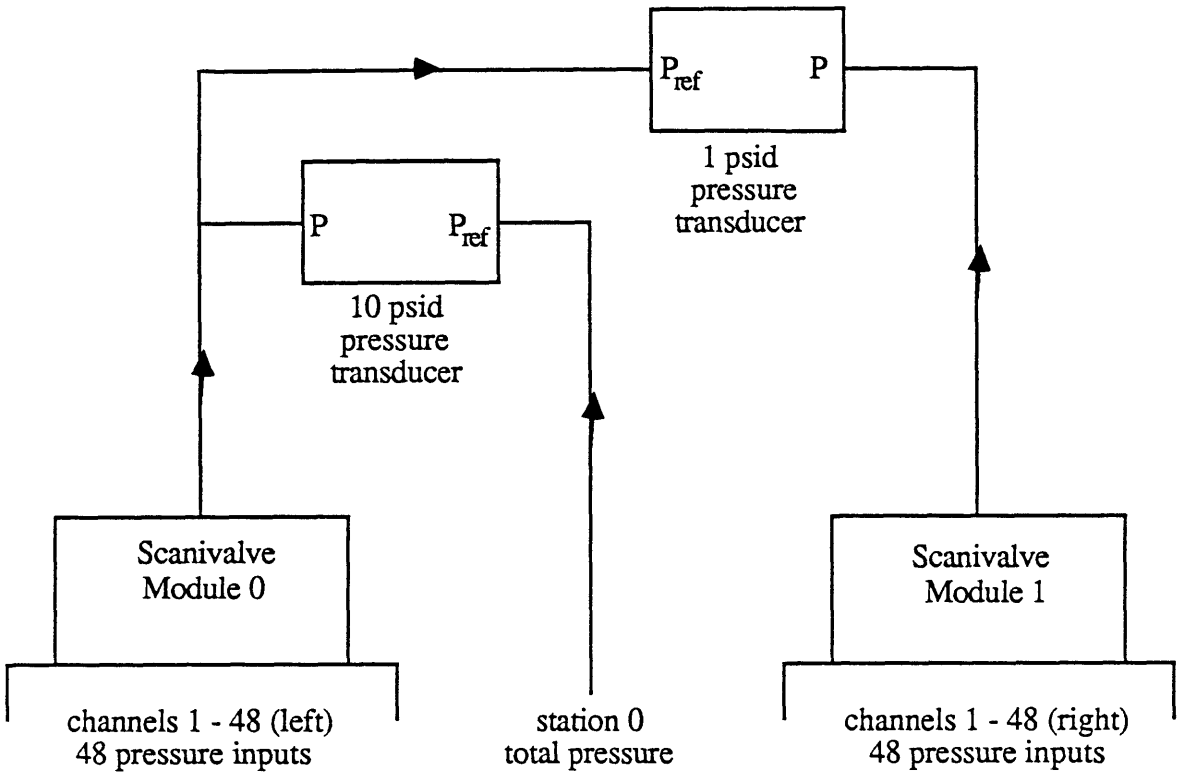

Fig. 4.12 Schematic of Scanivalve pressure transducer connections. Each module of the Scanivalve has provisions for 48 pressure inputs. The 1 psid transducer measures the pressure difference between the same channel on module 0 and 1 and the 10 psid measures the pressure difference between module 0 and the inlet total pressure.

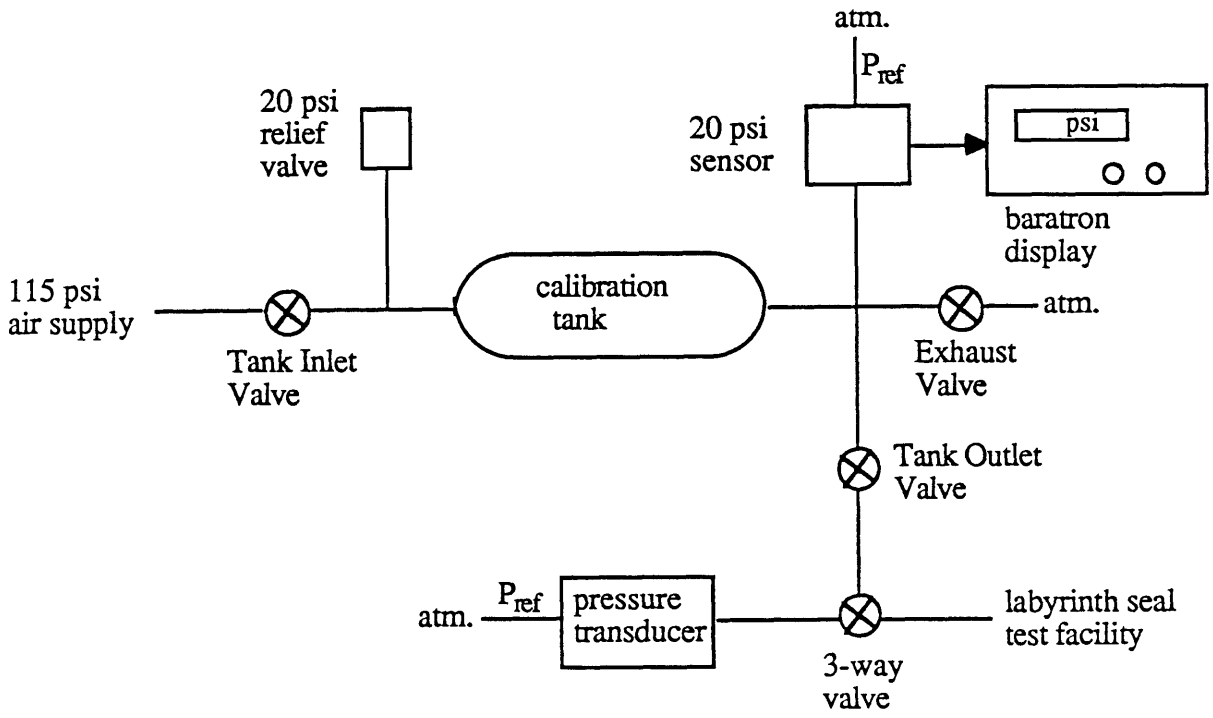

Fig. 4.13 Pressure transducer calibration system

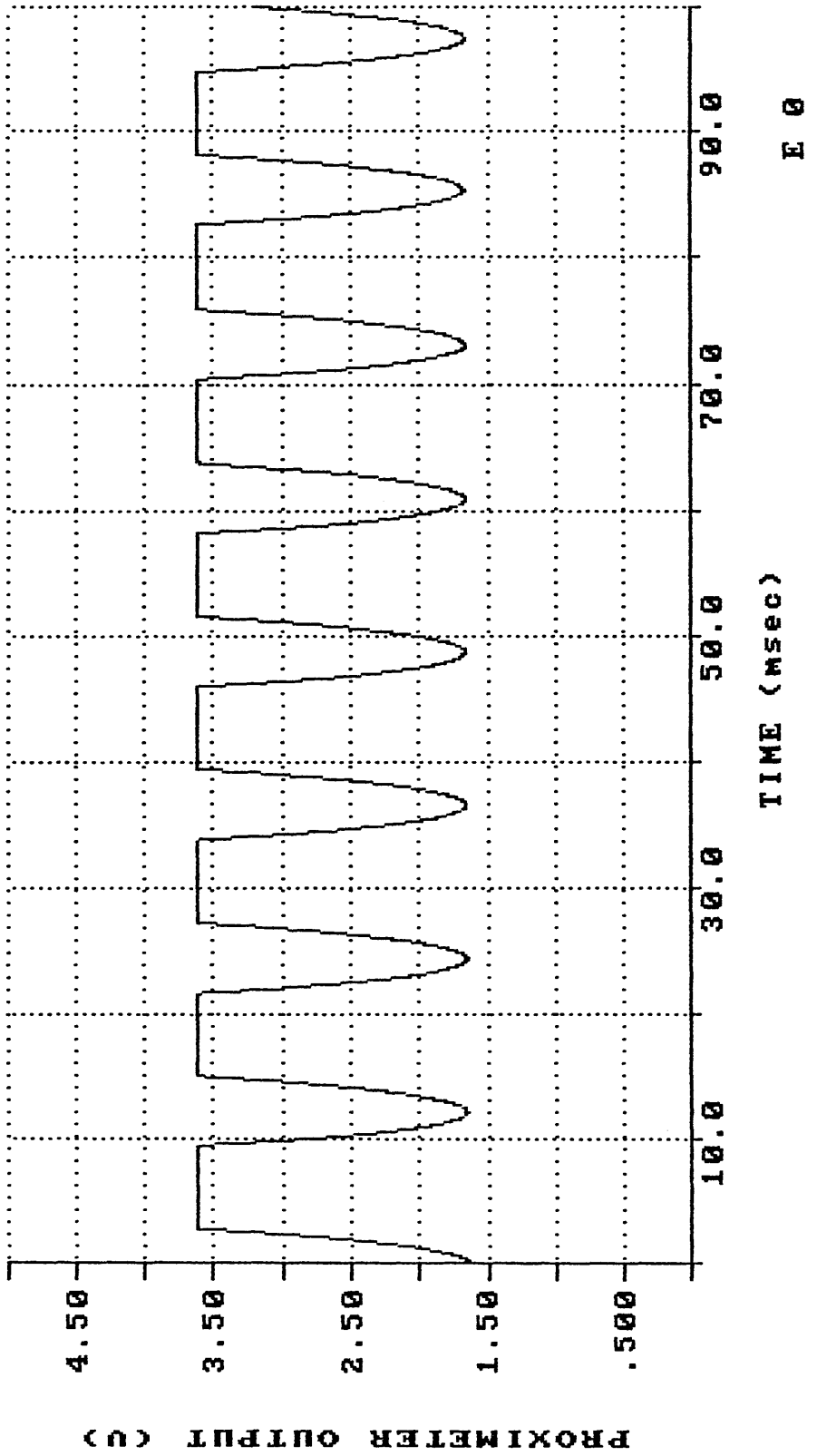

Fig. 4.14 Typical proximity probe voltage output. Negative peaks correspond to blade passing.

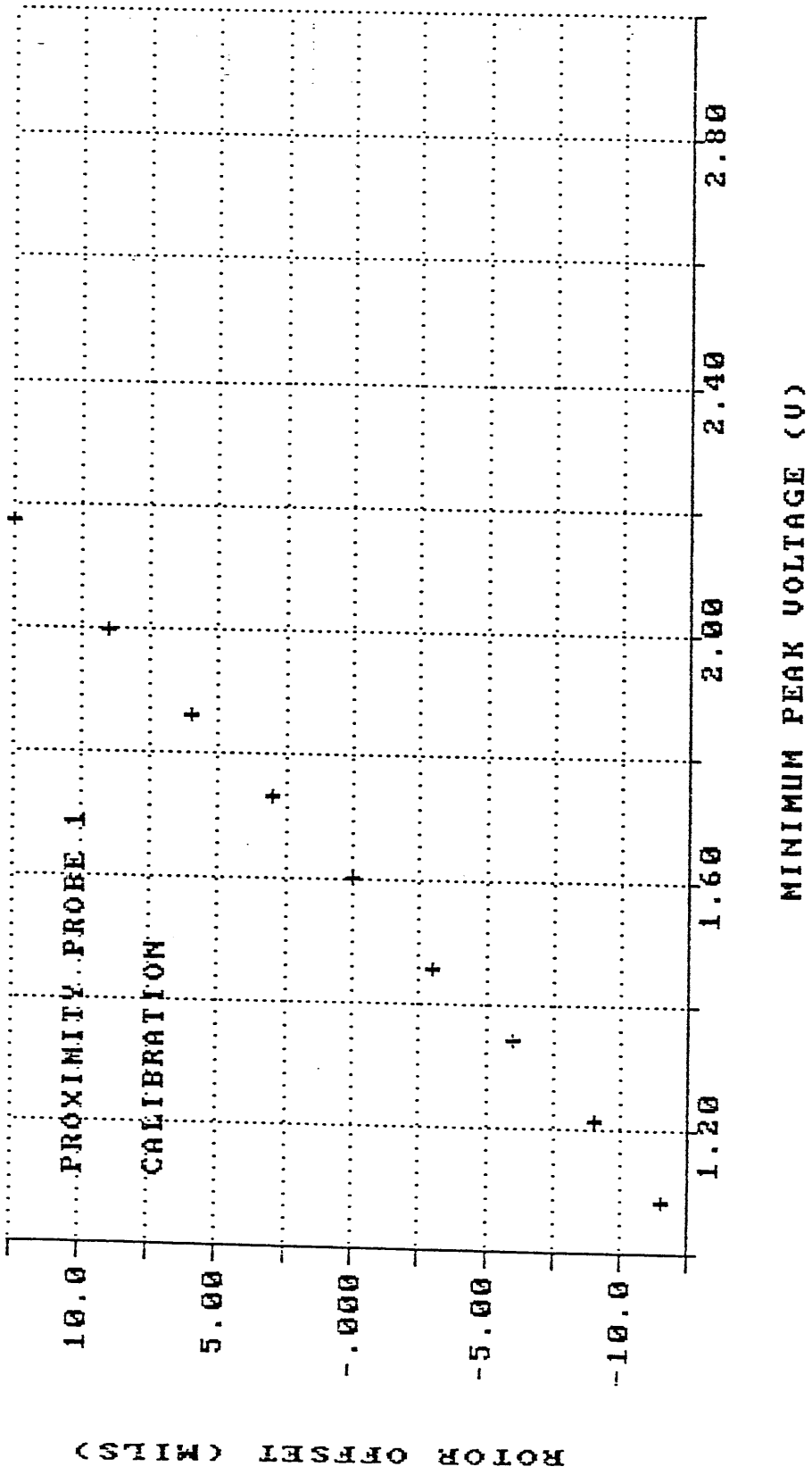

Fig. 4.15 Calibration graph for proximity probe

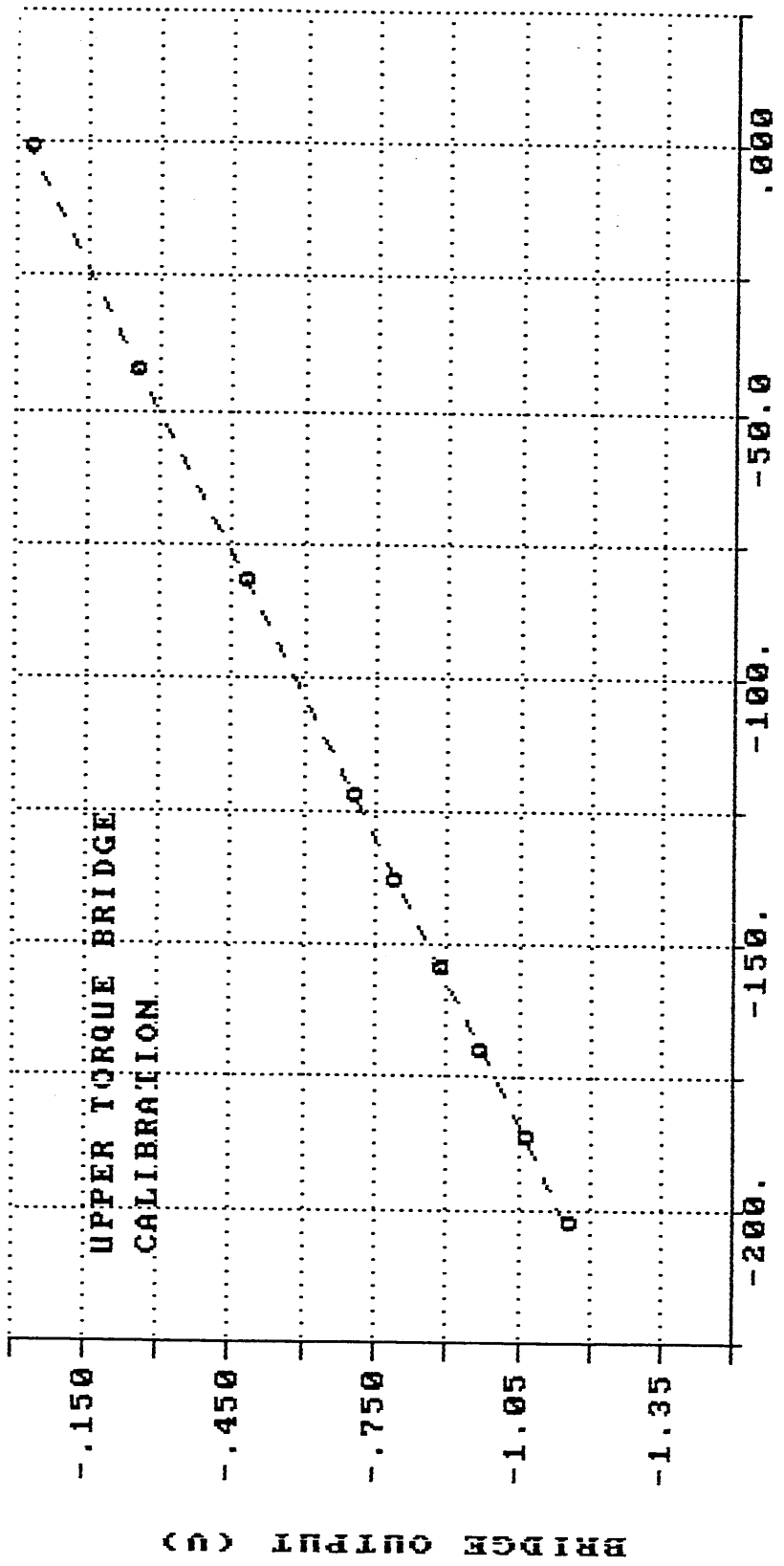

Fig. 4 16 Upper torque bridge calibration graph

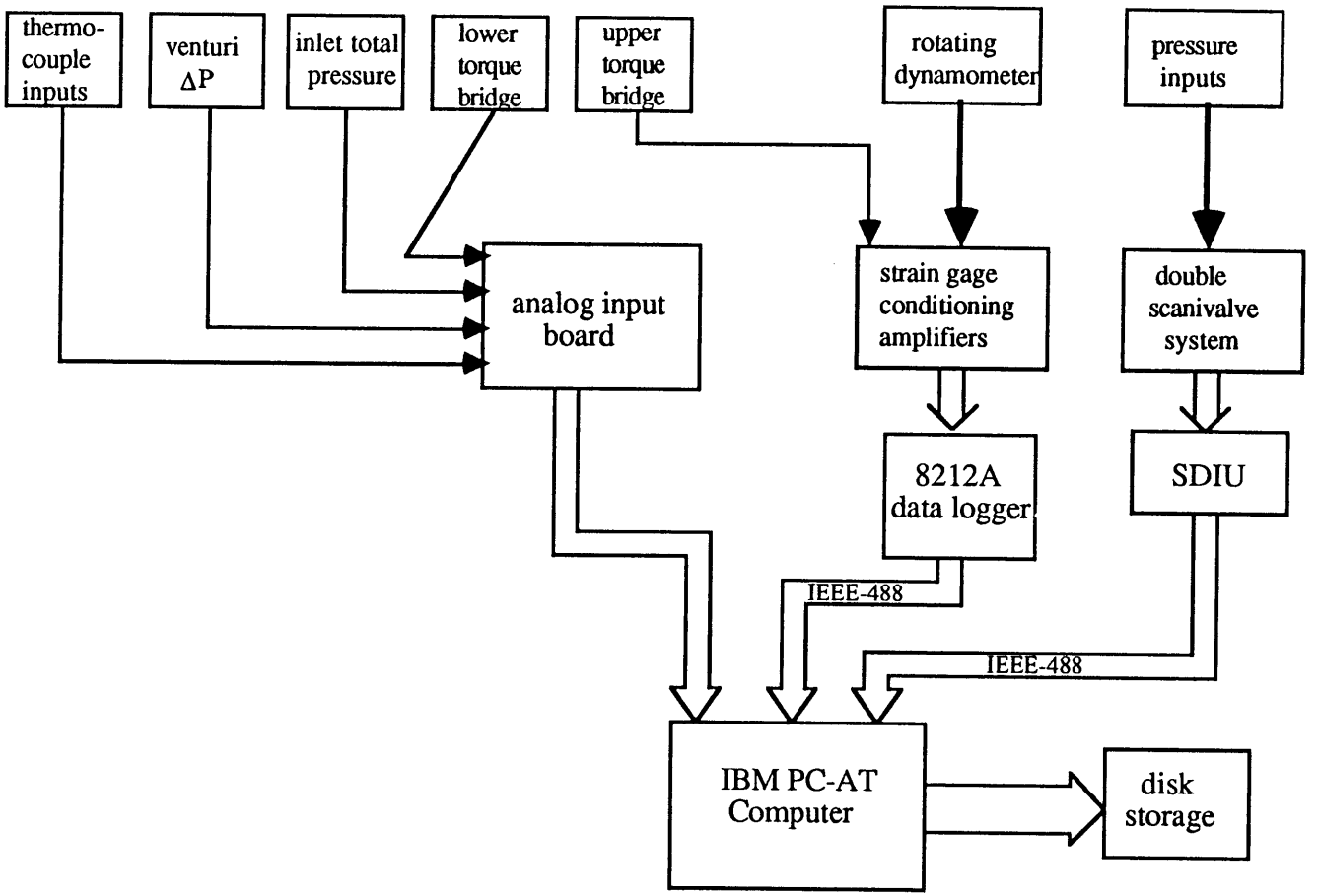

Fig. 4.17 Flow chart of data acqusition

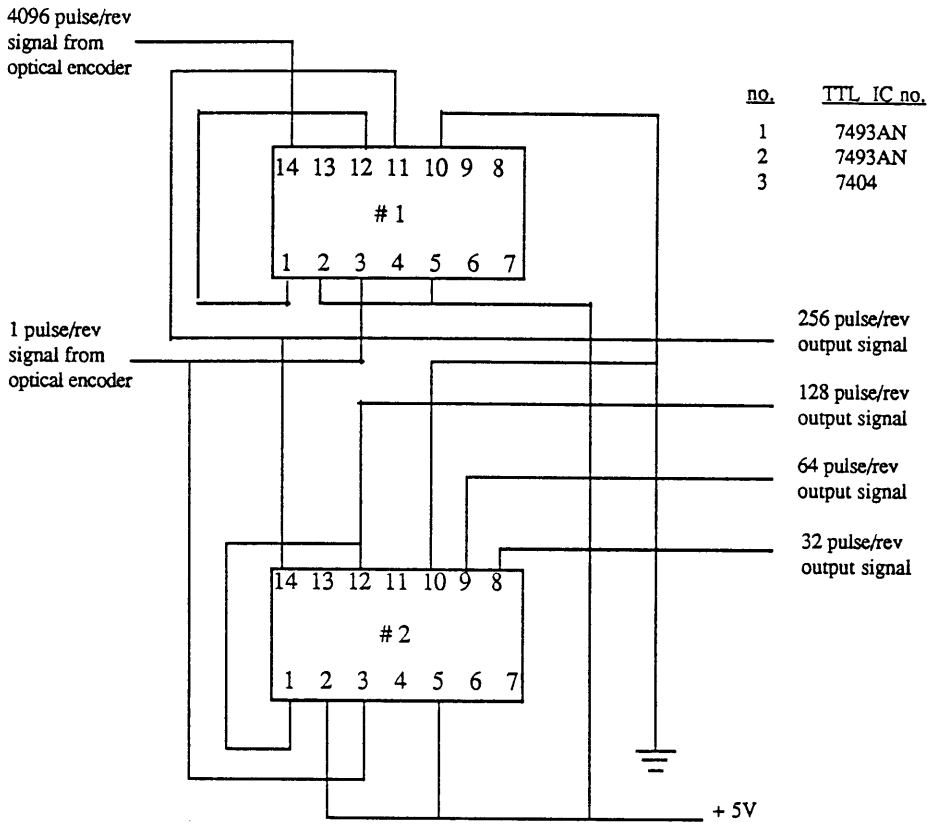

Note: pin 11 on IC #2 is a 16 pulse/rev signal used for tachometer input

Fig. 4.18 Schematic of circuit used to divide the optical encoder 4096 pulse per revolution signal into 256, 128, 64 or 32 pulse per revolution signal for data aquisition clocking

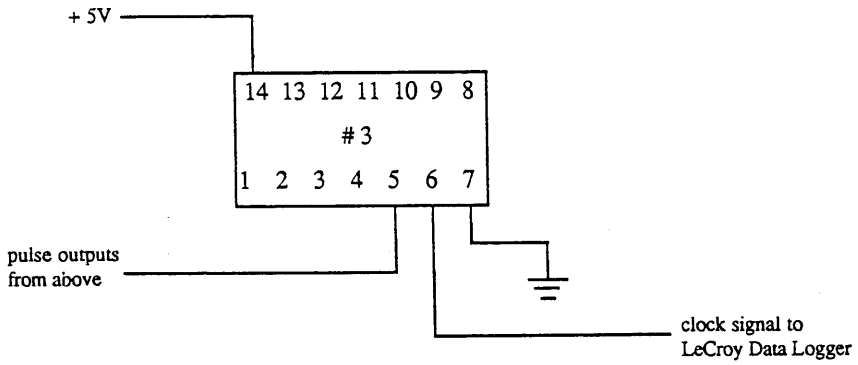

Fig. 4.19 Schematic of inverter circuit for pulse outputs from fig. 4.18.

CHAPTER 5

EXPERIMENTAL RESULTS

5.1 Steady Force Measurement

5.1.1 Data Acquisition and Processing

During each test run data from the rotating dynamometer was acquired at 32 data points per rotor revolution over 256 revolutions for a total of 8192 data points per dynamometer strain gage bridge. Because the data acquisition is synchronously clocked with the rotor, every 32 data points will occur at the same rotor angular position. Also, because the data acquisition is triggered by the zero reference pulse from the optical encoder the first data point on successive runs will occur at the same rotor angular position. A plot of the raw voltage from bridge 1 acquired during a typical test run is shown in figure 5.1.

Although only information from 6 bridges is necessary in order to resolve all components of force and moment, data from all nine bridges was acquired and stored. This assured that if any of the bridges failed, testing could continue without complete disassembly of the test section.

Data was immediately stored on the hard disk after every test run. Writing to the hard disk takes approximately 30 seconds for each test run which is the limiting time factor between successive runs. Also, after every day of testing all data was written to floppy disk in both raw format and ASYSTANT format (ASYSTANT format is necessary for data processing). Raw data is converted to ASYSTANT format through CATASYST software acquired from LeCroy.

To calculate the desired steady lateral force the 8192 data points from each bridge were first averaged over the 256 revolutions which resulted in an average voltage output for each bridge at 32 rotor angular positions (equally spaced, 11.25 degrees apart). Averaging was

done by reshaping the 8192 data points into a 256x32 matrix where each row represents data taken during one rotor revolution. The average of each column was then found which results in a 32-component vector representing the average bridge output in volts at the 32 rotor positions where data acquisition occurred. This was done for six strain gage bridges.

The averaged voltage values from the six bridges were then organized into 32 six-component vectors, each vector representing the averaged strain gage bridge output voltage of six bridges at one of the 32 rotor angular positions. Each of the 32 voltage vectors was then multiplied by the six-by-six calibration matrix to give 32 six-component force and moment vectors which represent the average value of the six components of force and moment in the rotating reference frame acting on the rotor at 32 positions over one rotor revolution. A single force or moment component would then consist of one entry from each of the 32 force vectors. F_1, for example, is the first entry of each vector. A typical plot of F_1 averaged over 256 revolutions is shown in figure 5.2.

Because F_1 and F_2 are in the rotating reference frame and we are interested in the steady forces in the inertial reference frame some transformation of the forces is necessary. To begin it is first necessary to develop a system of coordinates. The coordinates used are shown in figure 5.3, where X and Y are the inertial or lab coordinates and F_1 and F_2 are the dynamometer coordinates which rotate at the rotor speed, ω_r, rad/sec.

The lateral forces, F_1 and F_2, in the rotating coordinate system are transformed to the inertial frame through the relations,

$$F_x(\psi) = F_1 \cos(\psi + \phi) + F_2 \sin(\psi + \phi)$$

$$F_y(\psi) = F_1 \sin(\psi + \phi) - F_2 \cos(\psi + \phi)$$

where $F_x(\psi)$ and $F_y(\psi)$ are the force components in the X and Y direction, respectively. ψ is the rotor angular position in degrees measured from the rotor position at the first data point and is given as,

$$\psi = \omega_r t * (2\pi/360) = (n-1)/32 * (360)$$

where n is an integer from 1 to 32. Because of the synchronous data acquisition clock and zero reference trigger, ψ will equal the same 32 values on all test runs regardless of rotor speed. The phase angle, ϕ, is the angle between the F_1-axis and the X-axis at the time of the first point in the data acquisition.

Because F_x and F_y, which represent the averaged force components in the X and Y directions, respectively, over one rotor cycle can vary with rotor angular position, ψ, they still do not represent the steady force which is desired. The steady force components $\overline{F}_x$ and $\overline{F}_y$ then are simply the average value of F_x and F_y, respectively

The resultant steady force in the inertial reference frame, **F**, then has magnitude $\overline{F}$ and angle θ given as,

$$\overline{F} = \sqrt{\overline{F}_x^2 + \overline{F}_y^2}$$

$$\theta = \arctan\left(\frac{\overline{F}_y}{\overline{F}_x}\right)$$

where θ is measured from the positive X-axis.

The phase angle, ϕ, which is the angle between the F_1-axis and the X-axis at the time of the first point in the data acquisition, was determined from dynamic calibration data. As was explained in the previous chapter an aluminum calibration disk was mounted on the dynamometer in place of the turbine rotor and a weight suspended from the disk as the drive shaft was rotated with the DC motor. One set of data was taken at slow speed (30 rpm) so that dynamic forces would be minimized. A 45.1 N (10.14 lbf) load acting along the positive X-axis was suspended from the disk. The averaged values for F_1 and F_2 were found and then transformed to the inertial reference frame using the above procedure with $\phi = 0$. The

transformation resulted in $\overline{F}_x$ = -37.4 N (-8.40 lbf) and $\overline{F}_y$ = 25.1 N (5.64 lbf). The resultant force vector is then, **F** = 45.0 N (10.12 lbf) at an angle of 146.1 degrees (2.55 radians). To represent the correct loading the resultant force calculated should be rotated 146.1 degrees (2.55 radians), therefore,

$$\phi = 146.1° = 2.55 \text{ rad}$$

This value for ϕ was confirmed by checking several other cases of dynamic calibration data. The transformation equations are then,

$$F_x(\psi) = F_1 \cos(\psi + 146.1) + F_2 \sin(\psi + 146.1)$$
$$F_y(\psi) = F_1 \sin(\psi + 146.1) - F_2 \cos(\psi + 146.1)$$

5.1.2 Lateral Force vs. Eccentricity

The first series of tests consisted of measurement of the lateral force acting on the turbine rotor at one turbine operating condition. Three data sets were taken at each eccentricity which was varied from +0.33 mm (+13.0 mils) to -0.33 mm (-13.0 mils) in 0.076 mm or 0.010 mm (3 or 4 mil) increments. The rotor speed and mass flow were held constant throughout the tests at 3000 rpm and 4.80 kg/s (0.329 slug/s), respectively.

Both $\overline{F}_x$ and $\overline{F}_y$ were calculated for the three data sets at each eccentricity and the results are presented in Appendix C,table C.1. Because we are interested in the forces caused by rotor offset only, the values of $\overline{F}_x$ and $\overline{F}_y$ found for the turbine in the concentric position were subtracted from the respective values for $\overline{F}_x$ and $\overline{F}_y$ found for the various degrees of rotor offset for each data set and are presented in Appendix C, table C.2.

The first series of tests were used to indicate the repeatability of dynamometer measurements. The repeatability is shown to be exceptionally good with cross force magnitudes of tests at three identical conditions varying by only 0.0445 N (0.01 lbf).

The second series of tests consisted of measurement of the lateral force acting on the turbine rotor at eight eccentricities for various turbine operating conditions. The eccentricity was again varied from +0.33 mm (+13.0 mils) to -0.33 mm (-13.0 mils). The mass flow was initially set at 4.7 kg/s (0.322 slug/s) and held constant throughout the tests. Data was taken at four different speeds; 2200, 2600, 3000, and 3440 rpm.

Tests were begun with the rotor offset by the maximum positive value of +0.33 mm (+13.0 mils). One data set was taken at the four rotor speeds with the speed being varied between tests by changing the DC generator field voltage keeping the mass flow constant. The rotor offset was then incremented and the tests repeated. The tests were done at eccentricities of ±0.33 mm, ±0.25 mm, ±0.18 mm, ±0.10 mm and 0 mm (±13.0, ±10.0, ±7.0, ±4.0 and 0.0 mils).

Both $\overline{F}_x$ and $\overline{F}_y$ were calculated at each eccentricity and the results are shown in Appendix C, tables C.3 through C.6. Again, because we are only interested in the effects of rotor offset the values of $\overline{F}_x$ and $\overline{F}_y$ found for the turbine in the concentric position were subtracted from the respective values for $\overline{F}_x$ and $\overline{F}_y$ found for the various degrees of rotor offset. This results in the forces acting on the rotor solely due to rotor offset and are presented in Appendix C, tables C.7 through C.10.

Both a cross force and direct force were found and the magnitudes are plotted versus eccentricity for the various operating conditions in figures 5.4 through 5.11.

The conclusions which can be made from these first series of measurements are quite substantial. First, it was demonstrated that lateral forces due to rotor eccentricity do occur and can be measured accurately and repeatedly with this new facility. Also, the linearity of the cross force with eccentricity was shown. The plots of cross force versus eccentricity all had

correlation coefficients greater than 0.9994 and maximum straight line deviation of ± 0.18 N (0.04 lbf).

5.1.3 Cross Force vs. Torque

The third series of tests consisted of measuring the cross force for various power levels while holding the rotor speed constant, thus varying the rotor torque. Data were acquired at eccentricities of +0.33 mm, +0.18 mm and 0 mm (13.0, 7.0, and 0.0 mils).

The power level was varied by changing the mass flow while simultaneously adjusting the DC generator field voltage to hold the rotor at a constant speed of 3440 rpm (design speed). The mass flow was controlled with the lower throttle valve (see flow loop description in chapter 3) which was initially set fully open. The throttle valve was incrementally closed and the field voltage decreased (thus lowering the turbine load) which effectively lowered the power level, and hence rotor torque, between test runs. Nine tests were done at rotor torque levels varying from 150% to 13% of design.

Again the concentric rotor values were subtracted from the eccentric values to eliminate any effects other than those due to rotor offset. The data are presented in Appendix C, tables C.11 through C.14 and plotted as cross force versus torque for both +0.33 mm and +0.18 mm (13.0 and 7.0 mil) eccentricities in figure 5.12. A least squares fit is also plotted for both eccentricities.

The data show that the magnitude of cross force is dependent on the turbine loading and in fact is quite linear with the rotor torque. Both the +0.33 mm and +0.18 mm (13.0 and 7.0) mil eccentricity data have correlation coefficients greater than 0.96 with maximum straight line deviation of less than 0.445 N (0.10 lbf).

5.1.4 β Calculation

The Alford factor, β, was calculated by rearranging the equation for cross force, F_y, given in Chapter 2 into the following form,

$$\beta = \frac{2\,F_y\,H\,R}{T\,e_x} = \frac{F_y\,H\,D_m}{T\,e_x}$$

where $D_m = 2\,R$ is the mean rotor diameter, T is the total rotor torque, H is the blade height, e_x is the eccentricity and F_y is the cross force.

Data from the second series of tests, in which the cross force was measured for various rotor eccentricities, showed that the cross force was very linear with eccentricity (correlation coefficients average 0.9999) while all other operating conditions remained constant. Because of the linearity the ratio F_y/e_x is constant at any given operating point and in the above equation it can be seen that β is therefore not dependent on eccentricity. This agrees with the theory which says β is dependent on turbine geometry and operating point, not the amount of rotor eccentricity.

Because we are testing a single turbine, the variation of β with turbine geometry cannot be determined. It is however possible to determine how β varies with turbine operating point. To do this, the Alford factor was calculated for nine turbine power operating levels at two eccentricities, +0.33 mm and +0.18 mm (13.0 and 7.0 mils). The data are presented in Appendix C, table C.15 and plotted as β versus torque in figures 5.13 and 5.14.

The plots of β versus torque (which is directly proportional to power at constant speed) rises sharply from zero to a peak value at approximately the 50% power level.and then slowly decreases to a constant value at higher power levels. Also, β is zero at some non-zero torque value (under 20% of design) which means that no cross force is generated below a certain torque (or power) threshold.

5.2 Azimuthal Pressure Distribution

5.2.1 Data Acquisition and Processing

In order to distinguish between lateral forces caused by blade-tip clearance variations (the Alford force) and circumferential static pressure variations some measure of the azimuthal static pressure distribution is necessary. If the azimuthal pressure distribution is known, the force acting on the rotor due to pressure variations can be calculated. The contribution of the pressure variation forces can then be found by comparing them to the total force acting on the rotor as measured by the rotating dynamometer.

The static pressure was measured at three axial locations, A, B and C (A being the farthest upstream), along the rotor blade at eight equally spaced azimuthal locations. The axial locations are stations 5, 6 and 7 on the instrumentation map (see figure 4.11). Each of the three axial stations have two static pressure taps located 180° apart, so data were taken at four positions of the rotatable casing giving eight static pressure measurements around the casing diameter. Because a constant reference pressure is required, station 6 static taps were used. Station 6 has eight static taps equally spaced along the diameter of the casing which meant even as the casing was rotated to four different positions, station 6 static taps were still located in the same locations relative to a stationary axis.. The reference pressure used was that at 90° from the minimum rotor gap.

The procedure for data acquisition was as follows: The turbine test section casing was initially positioned at its maximum counterclockwise (looking down on the turbine inlet) position. In that position a station six static pressure tap which was used for the reference pressure is aligned 90° from the minimum rotor tip clearance. 100 pressure readings were taken for each of the six static pressure taps (2 sets, 180° apart, at 3 different axial locations). The eccentricity was then changed and the procedure repeated for nine eccentricities; ±0.33 mm, ±0.25 mm,±0.18 mm,±0.10 mm and 0.mm (±13.0, ±10.0, ±7.0, ±4.0 and 0.0 mils). The next step was to rotate the test section casing clockwise 45°. The reference pressure line

was moved to the station 6 static pressure tap which now was aligned 90° from the minimum rotor blade-tip clearance and again the pressures were read at all eccentricities. This was repeated at four test section casing positions.

The 100 pressure readings at each data point were first averaged. The values for concentric rotor were then subtracted from the values for eccentric rotor. Because we are only interested in the pressure variation the DC offset was also subtracted from each case. The values are plotted for the +13.0 and +7.0 mil eccentricities in figures 5.15 and 5.16. Also shown are the sinusoidal curve fits for each case. Also, in figure 5.17, the magnitude of the azimuthal pressure variation is plotted versus eccentricity for each axial location.

5.2.2 Pressure Force Calculation

The lateral forces acting on the rotor due to azimuthal pressure variations can now be calculated from the relations,

$$F_x^P = -\int_0^b \int_0^{2\pi} P(z,\theta) \cos\theta \, R \, d\theta \, dz$$

$$F_y^P = -\int_0^b \int_0^{2\pi} P(z,\theta) \sin\theta \, R \, d\theta \, dz$$

where the superscript P indicates forces due to pressure variations, b is the rotor blade axial length and R is the radius (which will be discussed further in the next paragraph). To simplify the calculations the axial blade length, b, was divided into three sections of length Δz_n, n = 1 to 3. It is assumed that the pressure at each of the these three axial sections is only a function of θ and equal to the pressure measured at the static pressure taps at axial locations A, B, and C, respectively. The integration is done over three bands and the total force due to pressure variation is then the sum of forces calculated for each band. The integrals simplify to,

$$F_x^P = -R \sum_{n=1}^{3} \Delta z_n \int_0^{2\pi} P_n(\theta) \cos\theta \, d\theta$$

$$F_y^P = -R \sum_{n=1}^{3} \Delta z_n \int_0^{2\pi} P_n(\theta) \sin\theta \, d\theta$$

where Δz_n is the axial length of the band of integration, n, which has pressure $P_n(\theta)$ equal to the pressure measured at axial locations A, B and C.

One question which might arise at this point is whether the pressure variation acts along the rotor hub area ($2\pi R_i$ x axial hub length, where R_i is the rotor hub radius) or just the area of the blade-tips. The percentage of blade-tip area to total projected area ($2\pi R_o$ x axial blade length, where R_o is the rotor outer radius) of each band was calculated. The blade-tip area to total projected area ratios at axial location i, r_i, were calculated to be 17.7%, 20.8% and 15.0% at axial locations A, B and C, respectively. The pressure force acting in the eccentricity direction, F_x^P, (which is the dominant pressure force component) was first calculated for the total area from the relations above with $R = R_o$ and then multiplied by r_i to determine the force if the pressure were acting on the blade-tips only. F_x^P was also calculated assuming the pressure acts on the entire hub of the rotor using $R = R_i$ in the above relations. These calculations were done for all eccentricities. It was found that the force calculated assuming the pressure acts on the blade-tips only was an order of magnitude less than the direct force which was measured with the rotating dynamometer while the forces calculated assuming the pressure acts on the entire hub was not only of the same order of magnitude, but within 11% (under 5% in most cases) of the direct forces measured by the rotating dynamometer.

Because the azimuthal variation in static pressure is not in phase with the blade-tip clearance variation, it also generates a cross force which acts in the same direction as the Alford force. The contribution of pressure force to the total cross force measured by the rotating dynamometer is found to range from 37% to 41% for all eccentricities.

These results are quite good considering (i) pressures were measured in only three axial locations and it was assumed constant across each axial length, Δz and (ii) pressures were measured at the inner diameter of the test section casing and assumed to have no radial variation.

The calculated forces due to azimuthal pressure variation are presented in Appendix C, tables C.15 and C.16 and plotted as force magnitude versus eccentricity in figures 5.18 and 5.19.

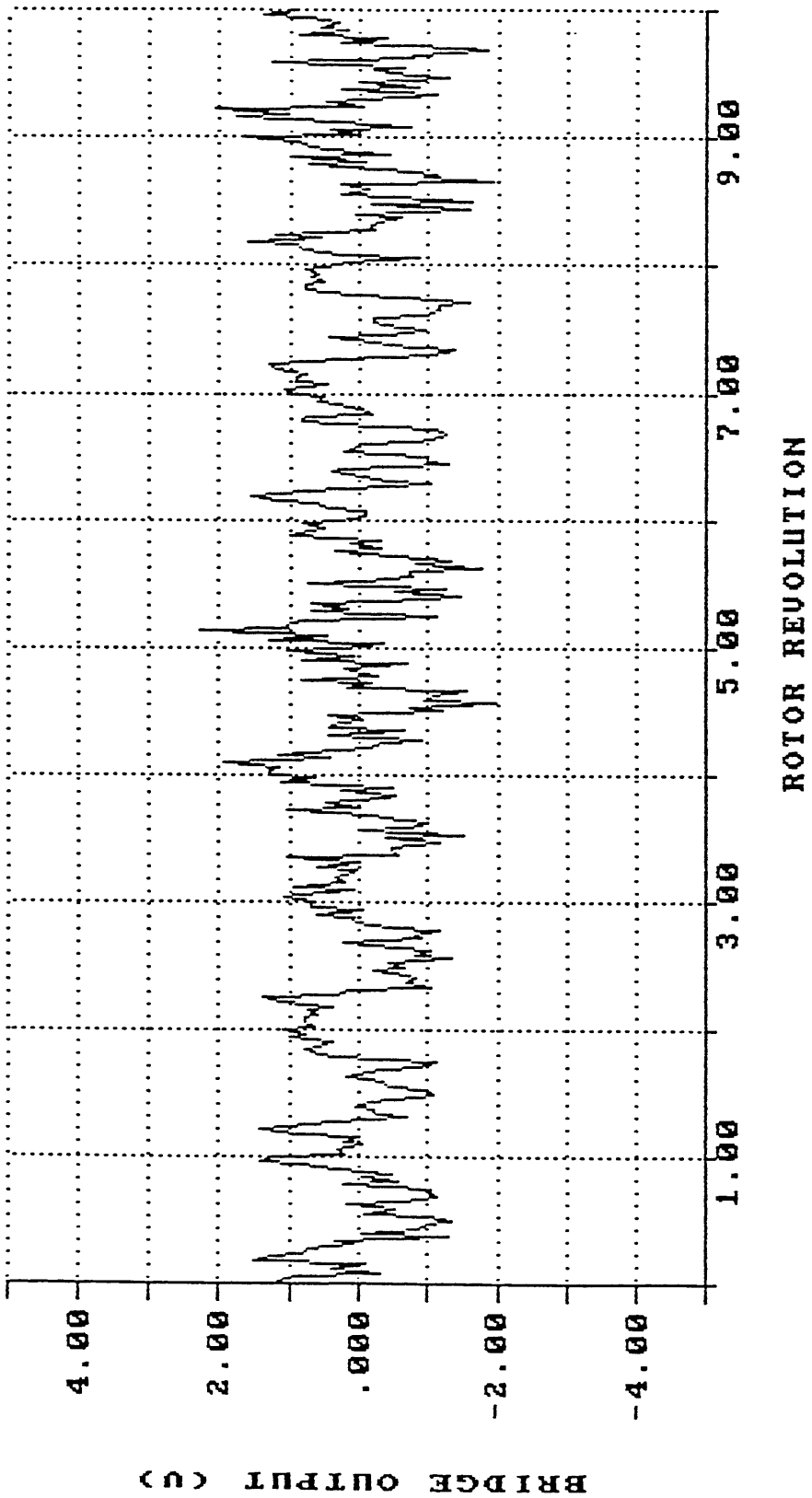

Fig. 5.1 Typical raw voltage strain gage bridge output. Shown is ten revolutions of bridge no. 7, 2600 rpm, +13.0 mils eccentricity

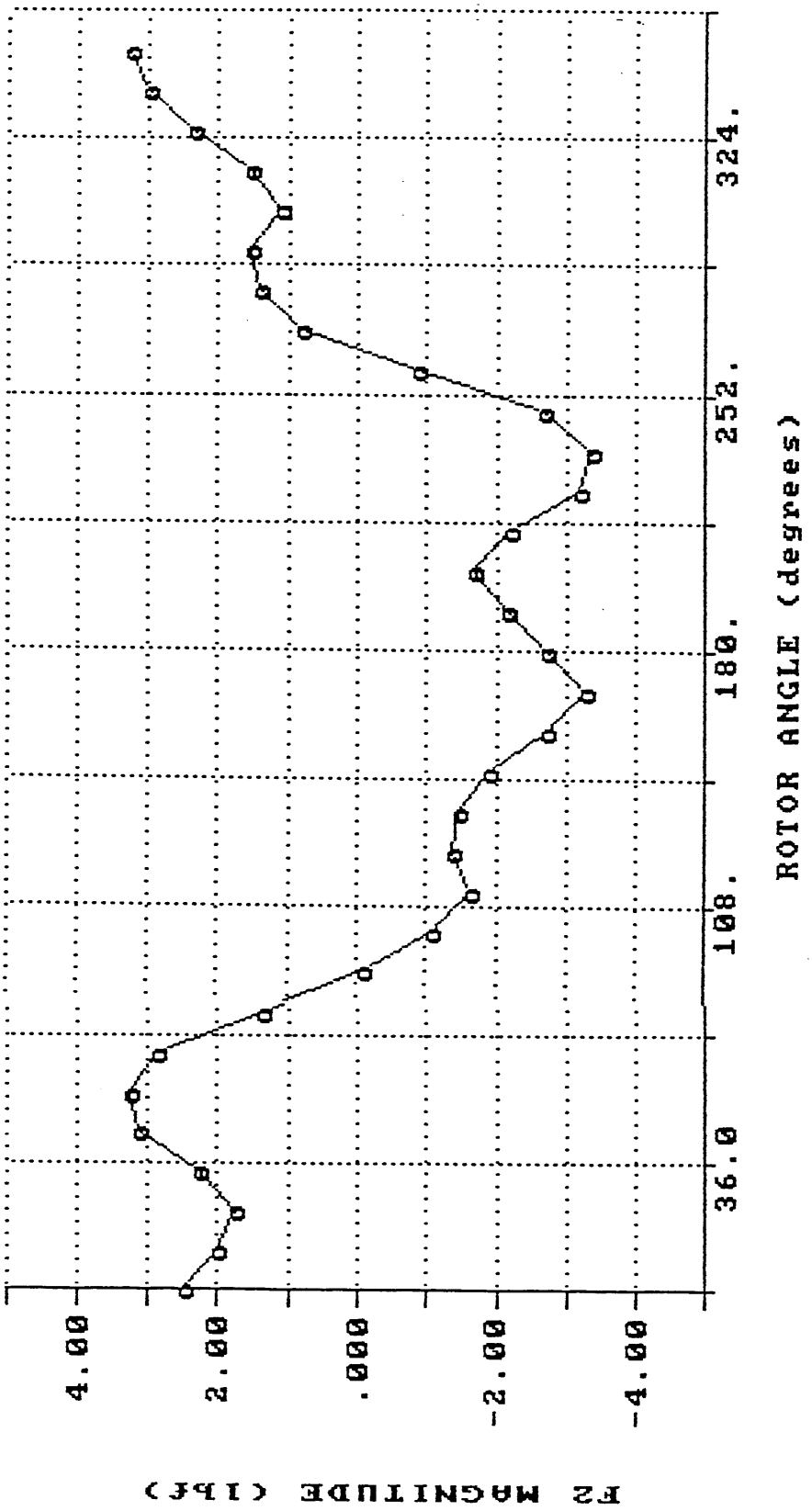

Fig. 5.2 Typical averaged force in the rotating frame. Shown is F_2 over one rotor revolution, 2600 rpm, +13.0 mils eccentricity

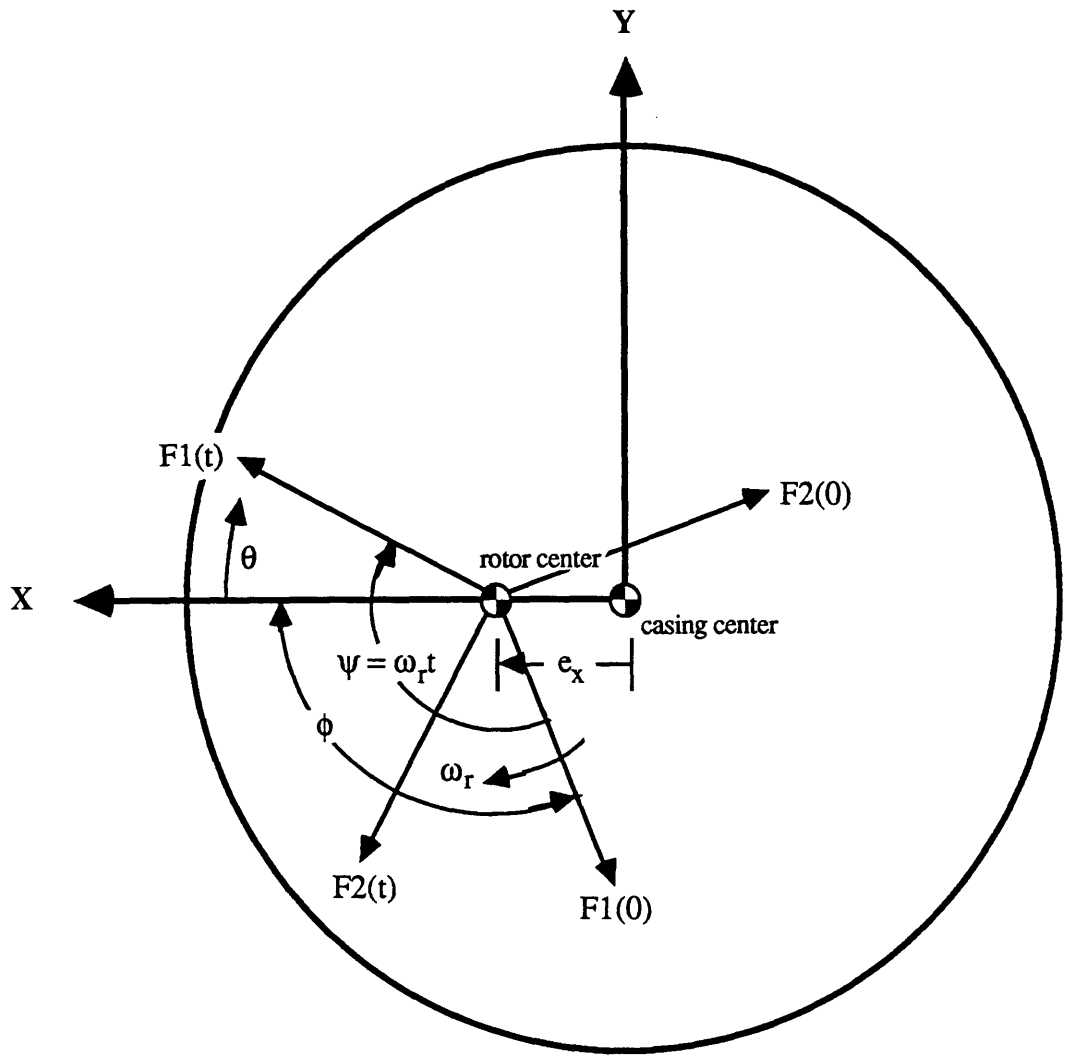

Fig. 5.3 Coordinate system used for data processing

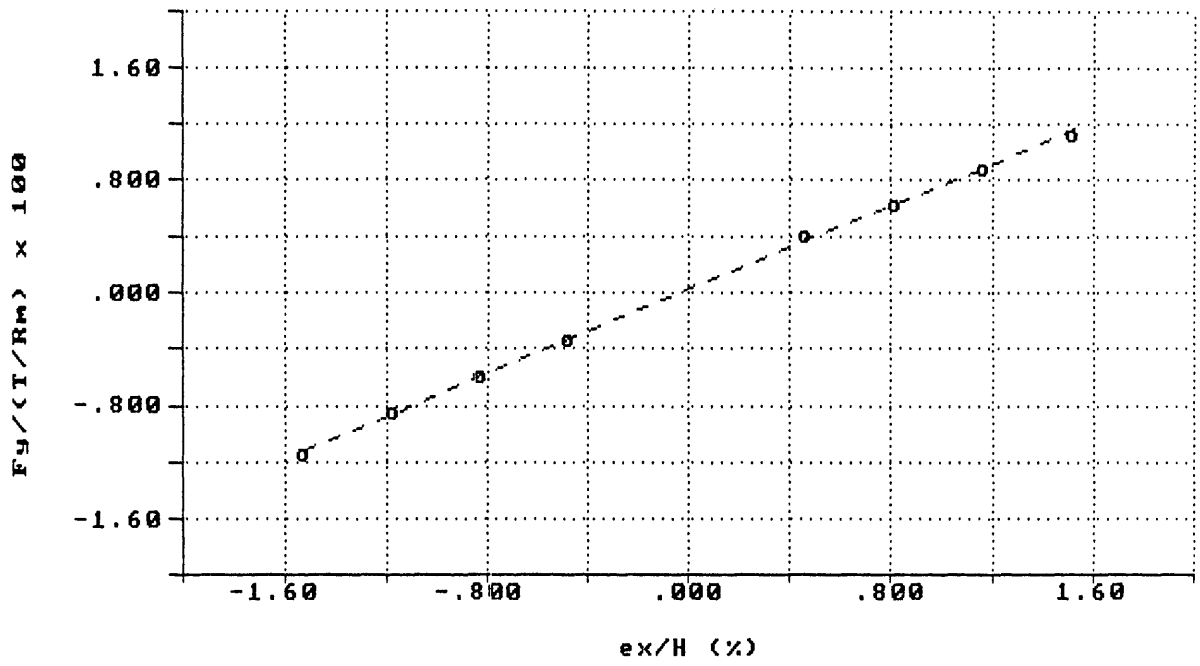

Fig. 5.4 Cross force vs. eccentricity, $\omega_r / \omega_{r,des} = 0.64$

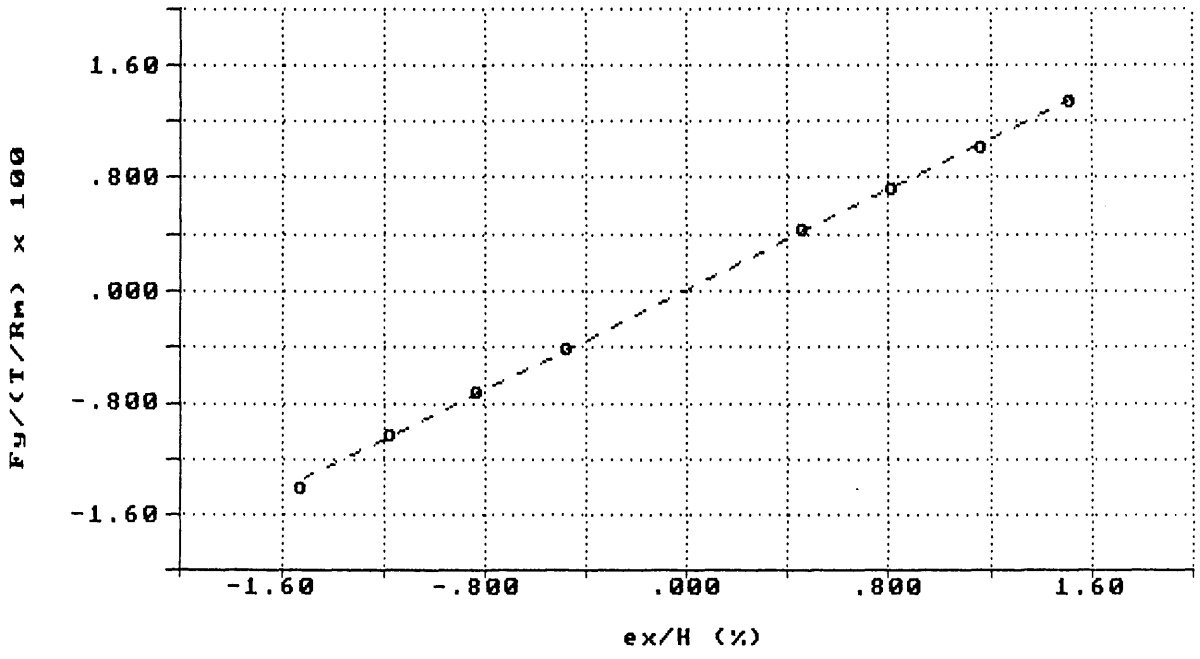

Fig. 5.5 Cross force vs. eccentricity, $\omega_r / \omega_{r,des} = 0.76$

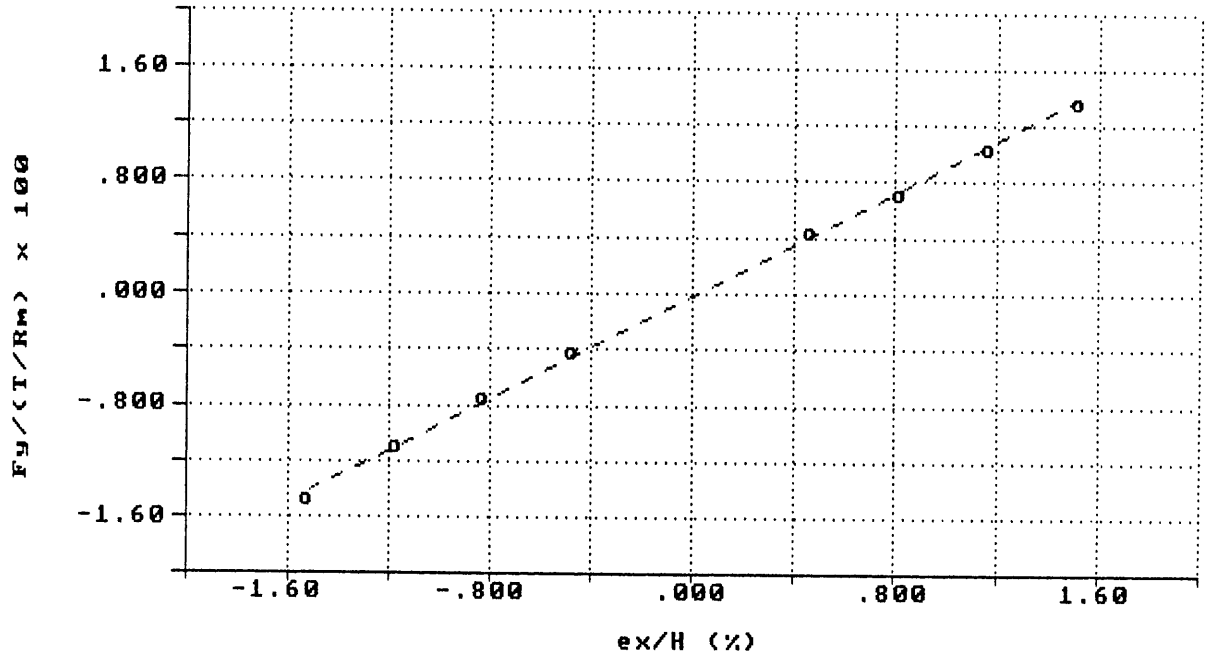

Fig. 5.6 Cross force vs. eccentricity, $\omega_r / \omega_{r,des} = 0.87$

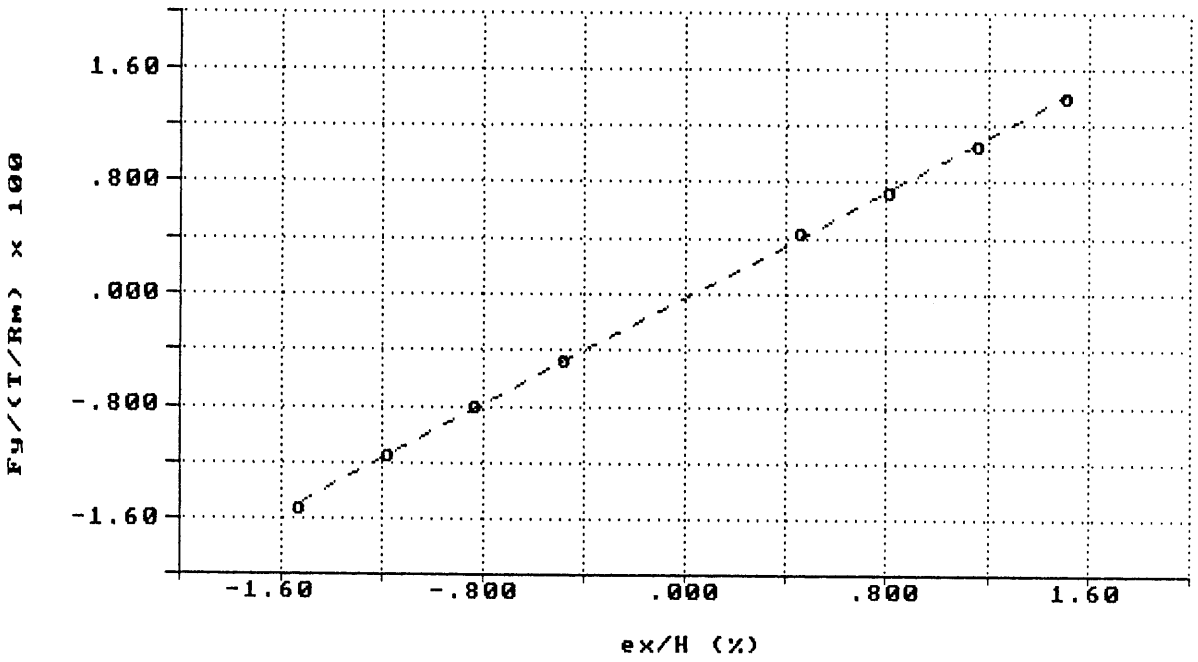

Fig. 5.7 Cross force vs. eccentricity, $\omega_r / \omega_{r,des} = 1$

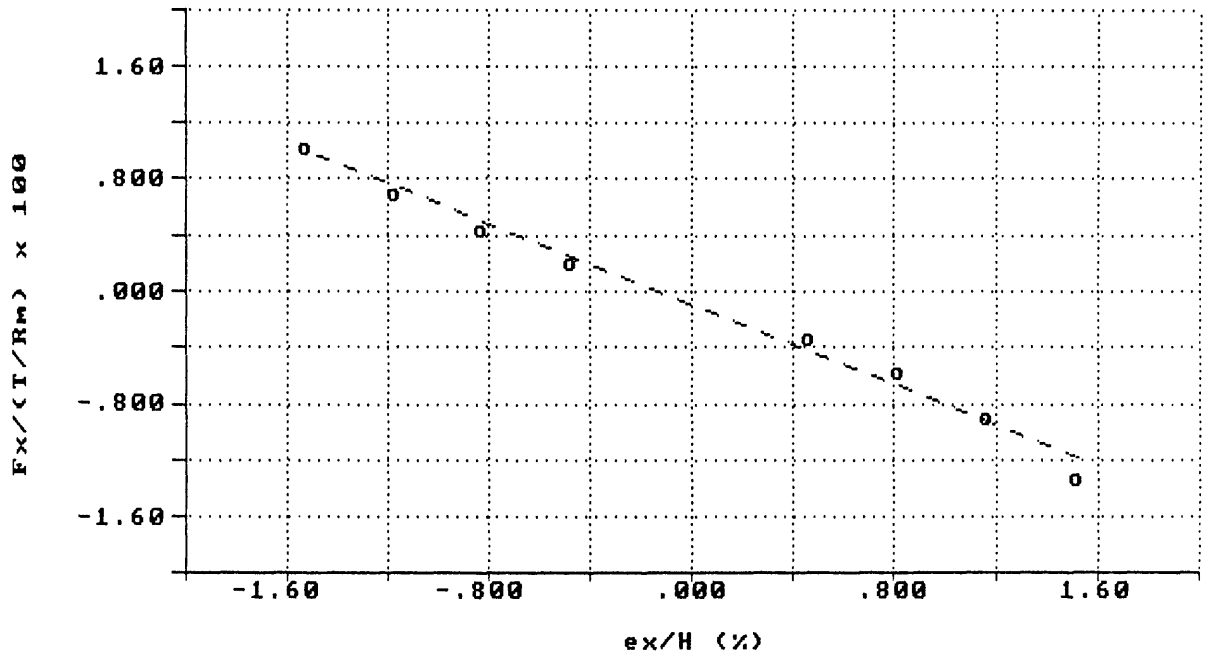

Fig. 5.8 Direct force vs. eccentricity, $\omega_r/\omega_{r,des} = 0.64$

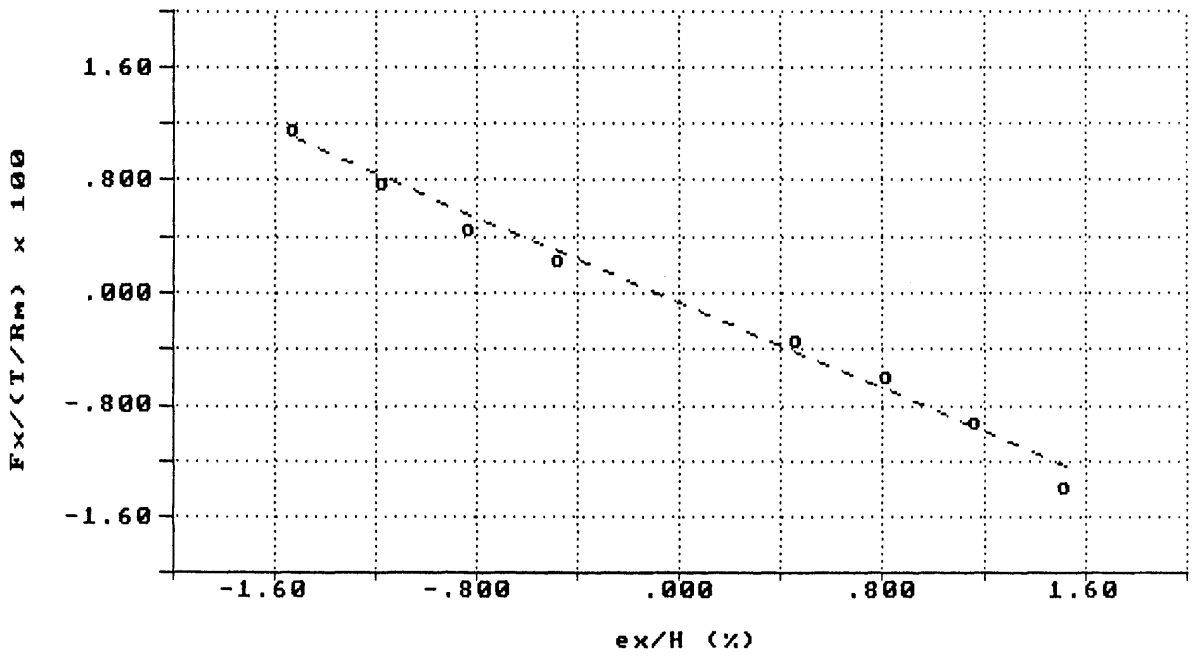

Fig. 5.9 Direct force vs. eccentricity, $\omega_r/\omega_{r,des} = 0.76$

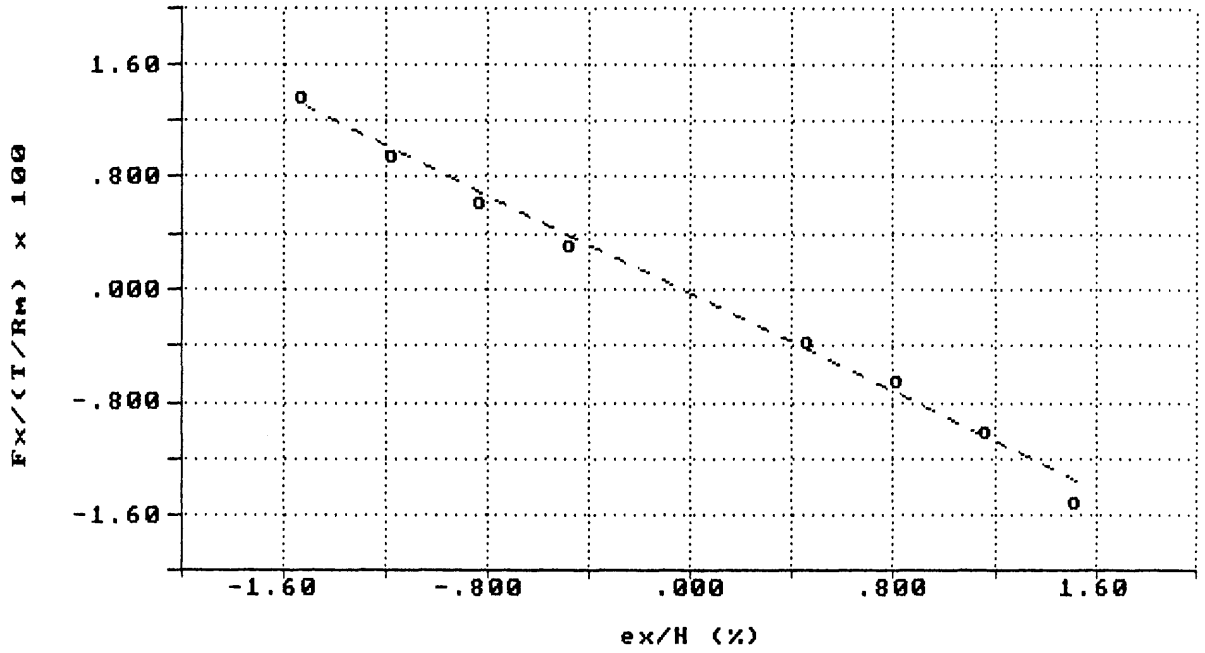

Fig. 5.10 Direct force vs. eccentricity, $\omega_r/\omega_{r,des} = 0.87$

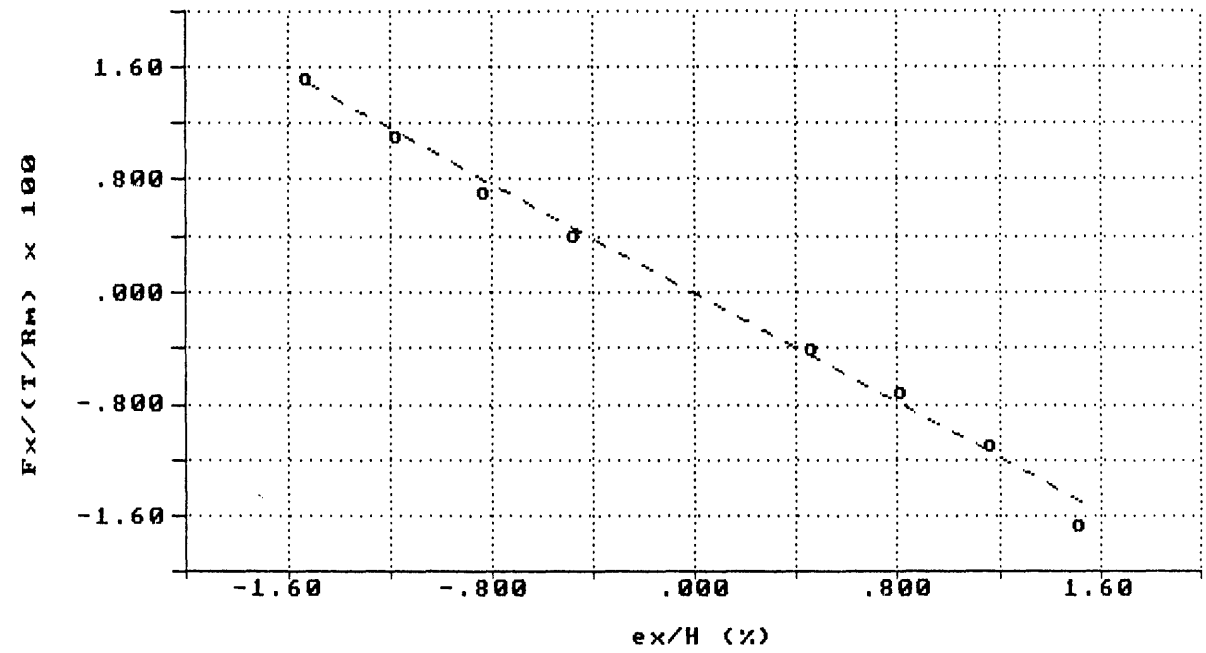

Fig. 5.11 Direct force vs. eccentricity, $\omega_r/\omega_{r,des} = 1$

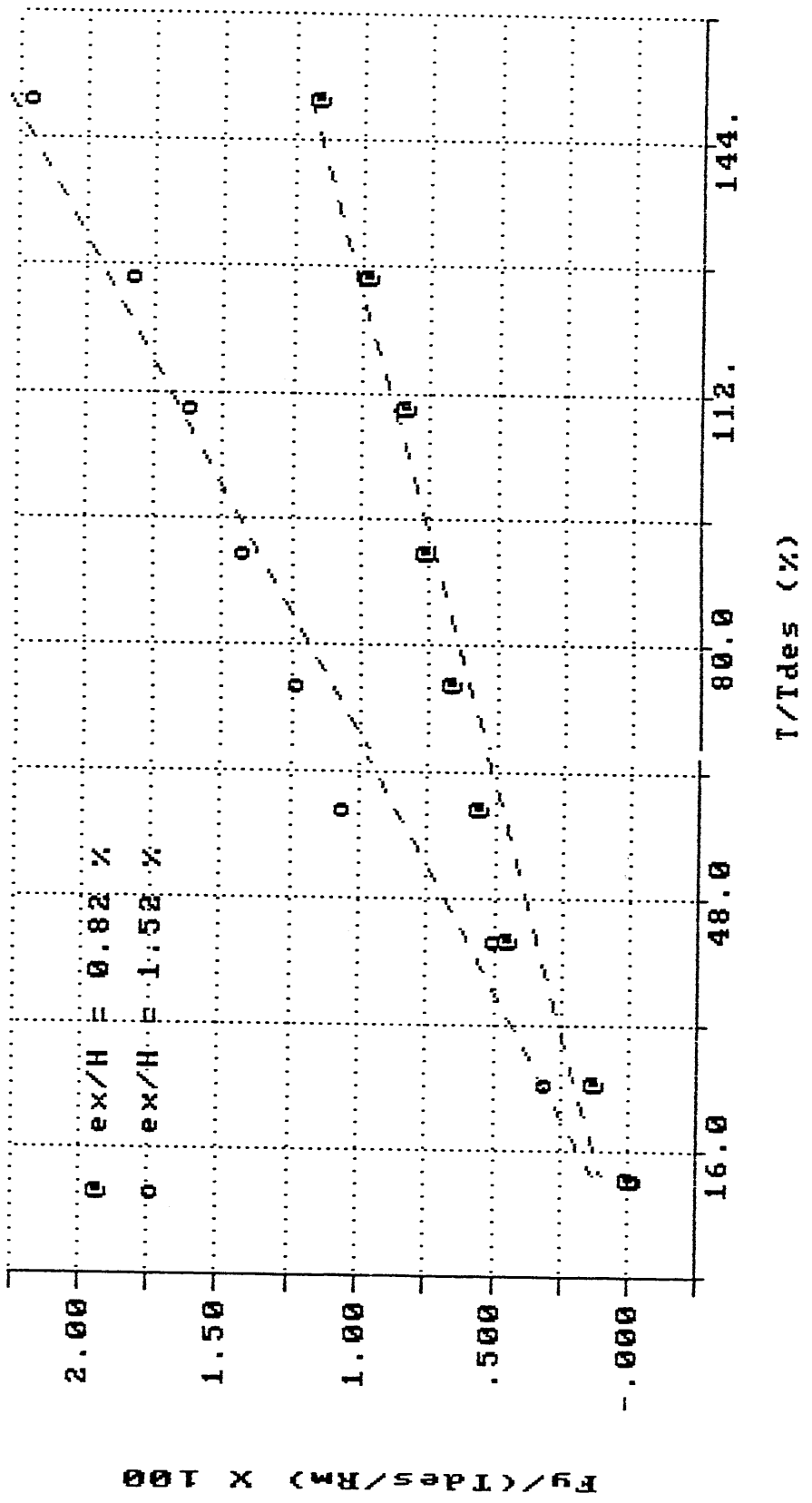

Fig. 5.12 Cross force vs. torque

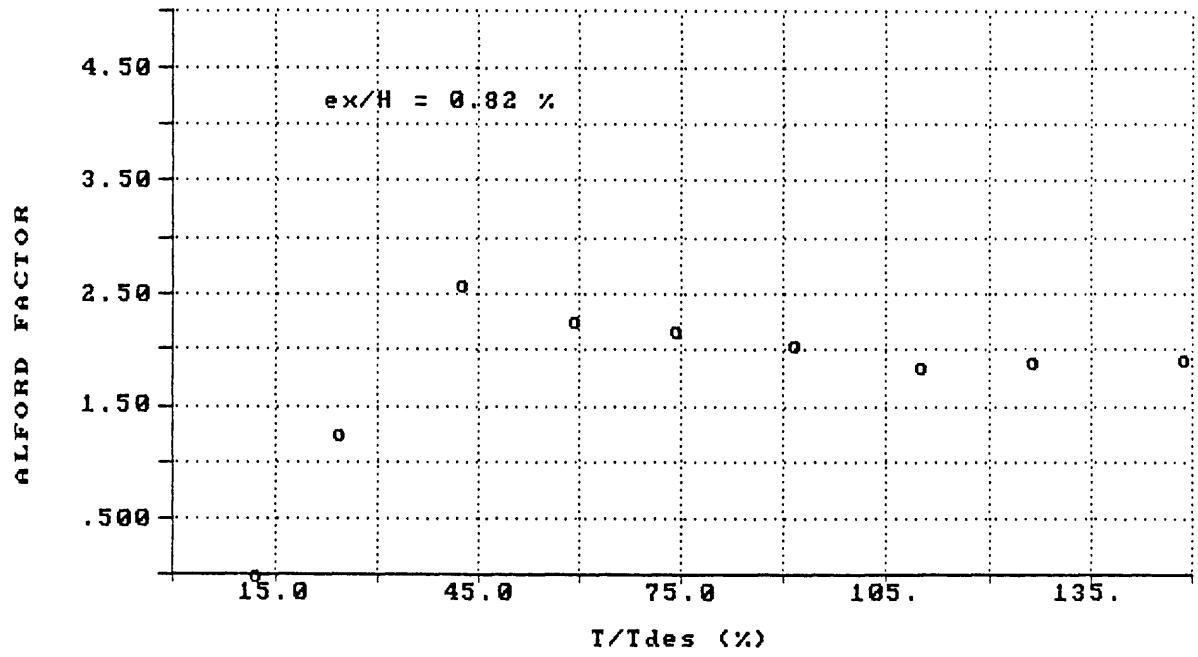

Fig. 5.13 Alford factor, β, vs. torque, e_x / H = 0.82%

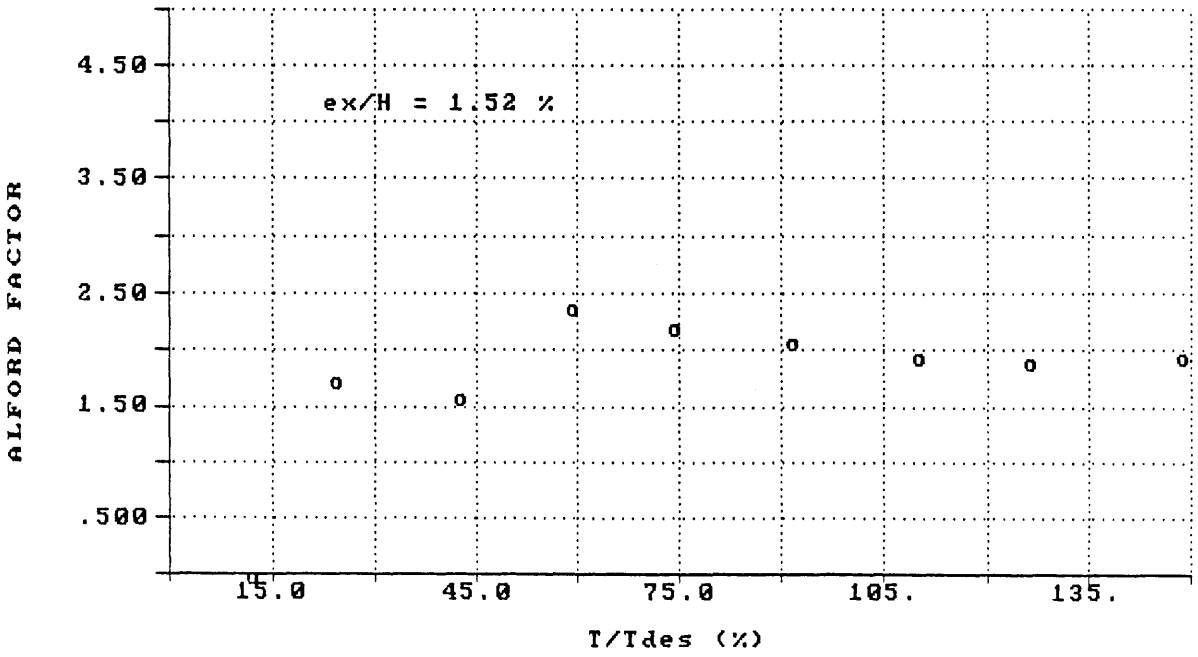

Fig. 5.14 Alford factor, β, vs. torque, e_x / H = 1.52%

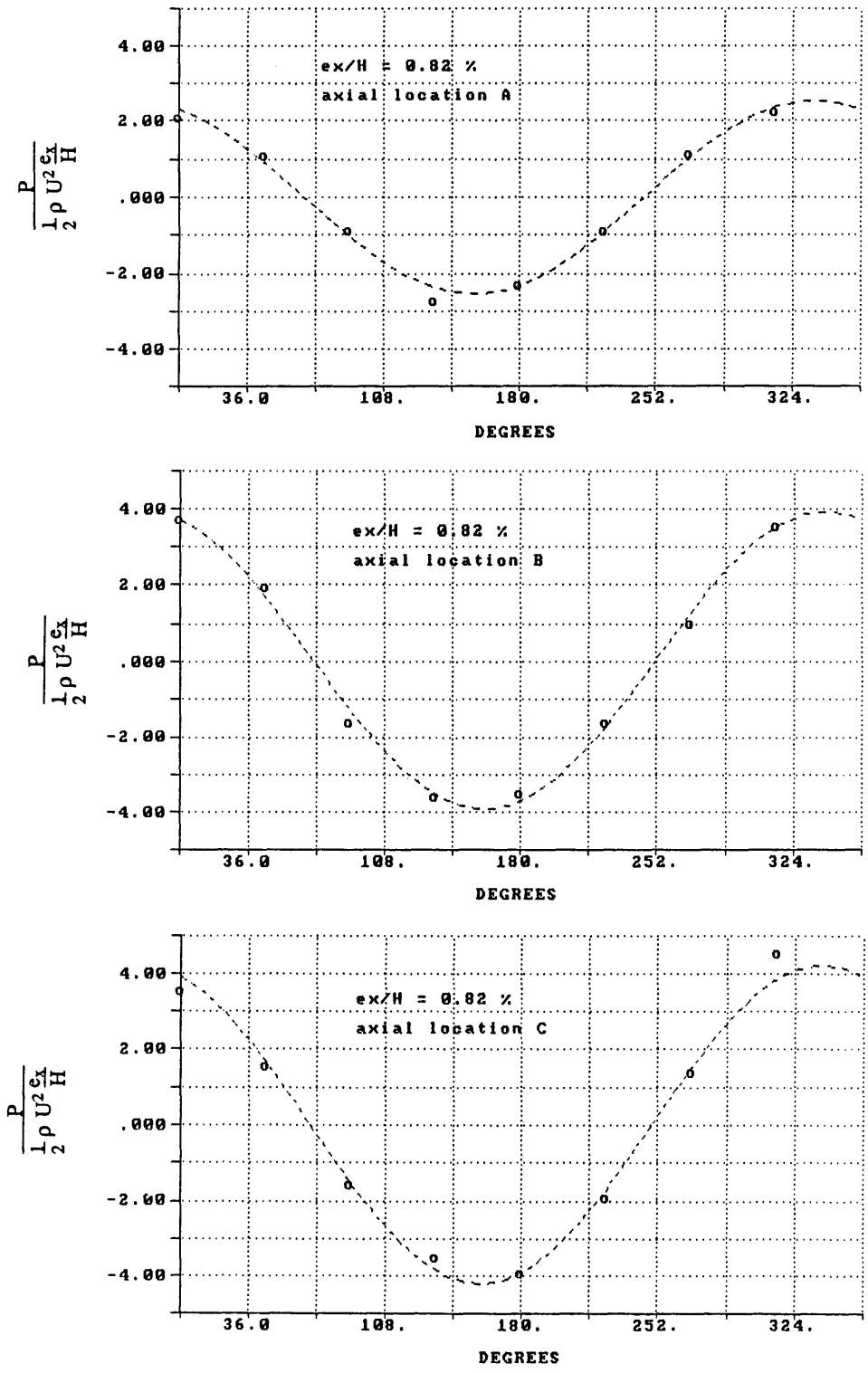

Fig. 5.15 Static wall pressure vs. angle, θ, $e_x / H = 0.82\%$. (i) axial location A (st. 5), (ii) axial location B (st. 6), (iii) axial location C (st. 7)

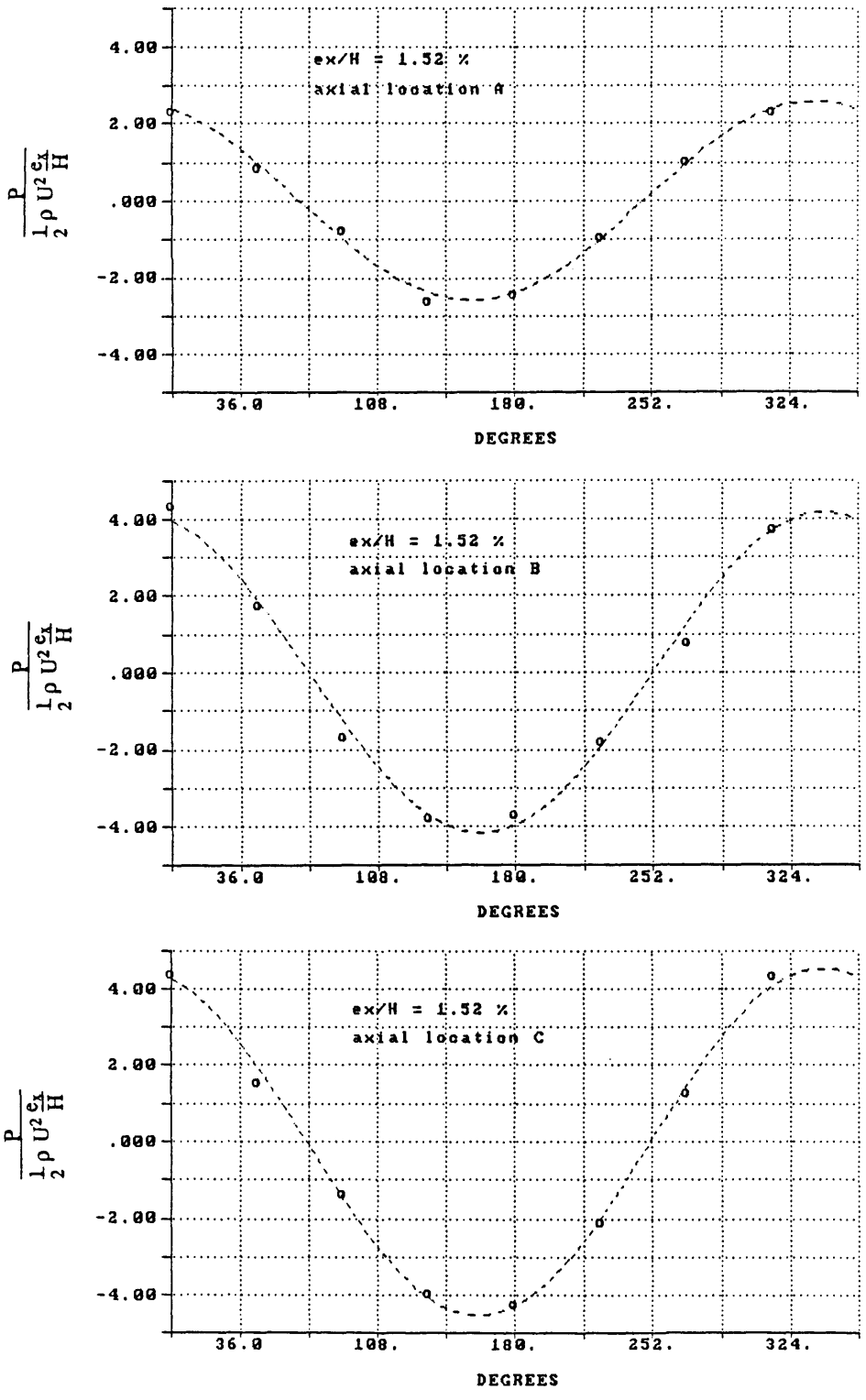

Fig. 5.16 Static wall pressure vs. angle, θ, $e_x / H = 1.52\%$. (i) axial location A (st. 5), (ii) axial location B (st. 6), (iii) axial location C (st. 7)

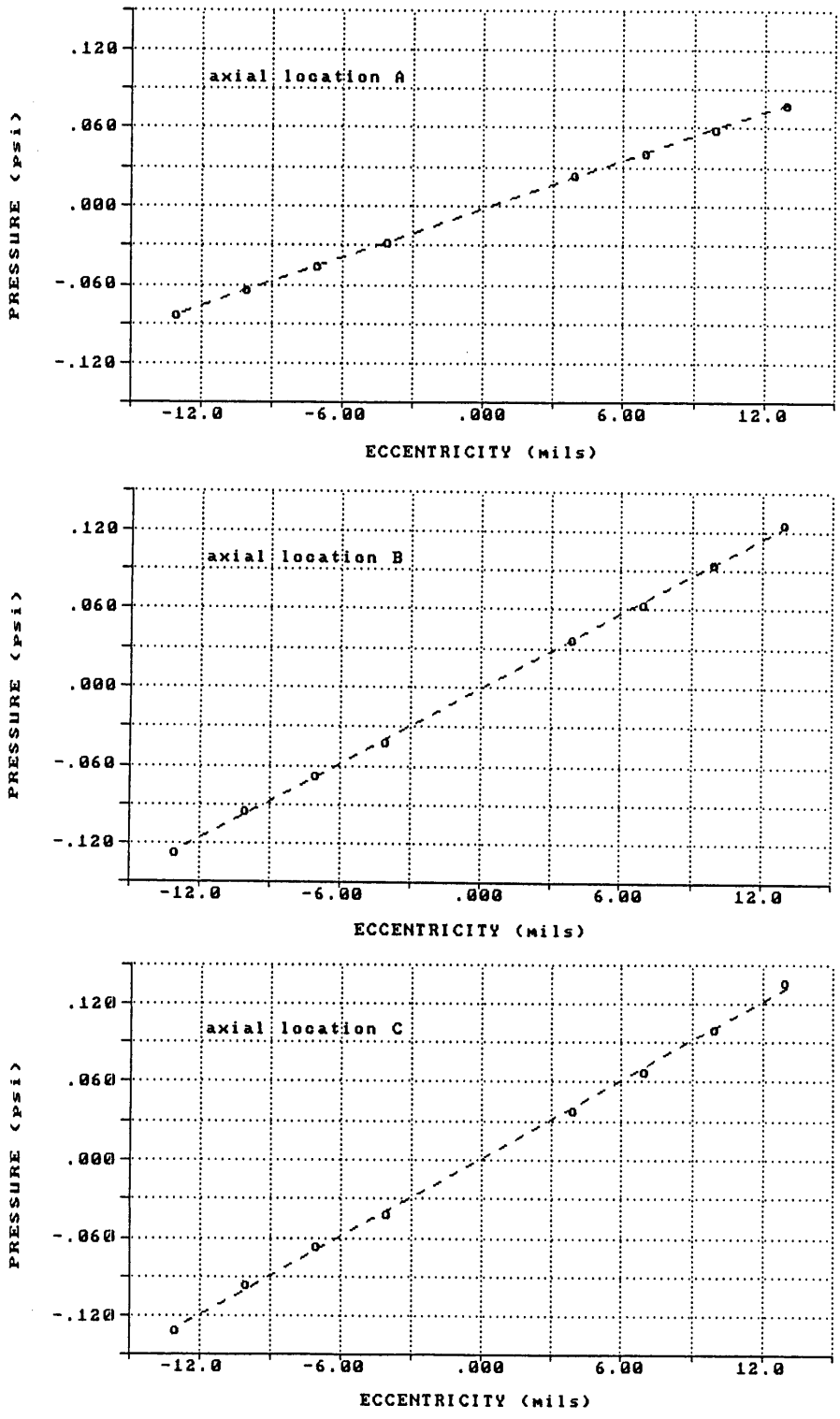

Fig. 5.17 Static wall pressure amplitude vs. eccentricity. axial location A (st. 5), (ii) axial location B (st. 6), (iii) axial location C (st. 7)

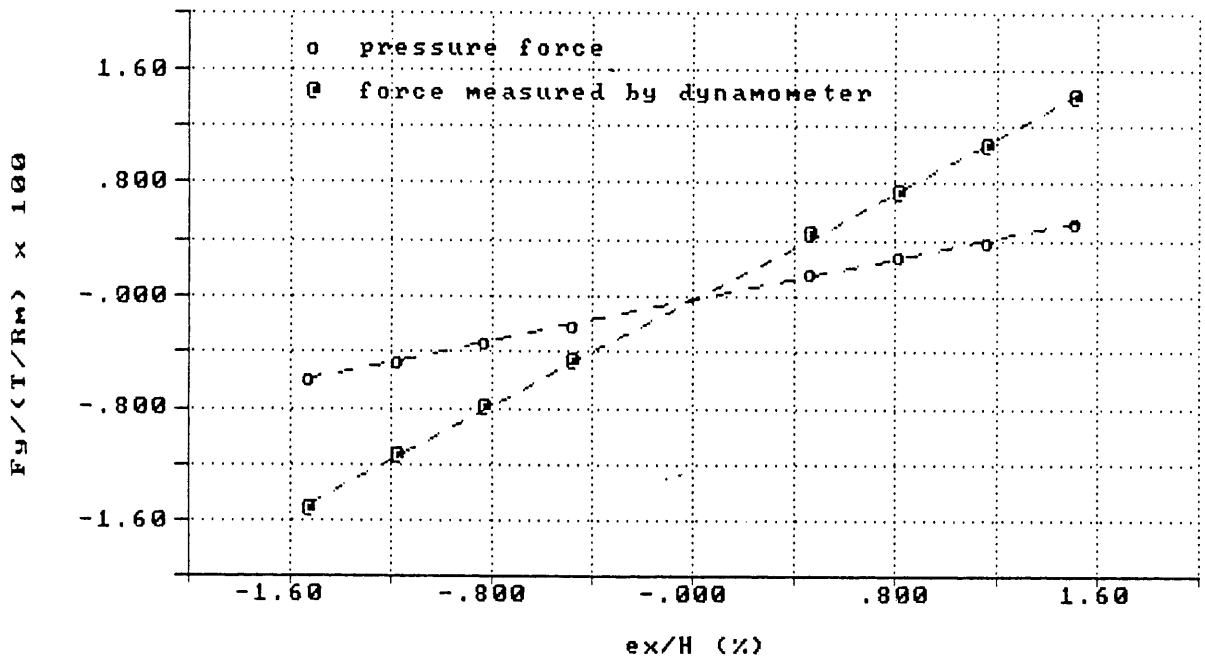

Fig. 5.18 Cross force due to azimuthal static pressure variation vs.eccentricity assuming the pressure acts on the rotor hub area

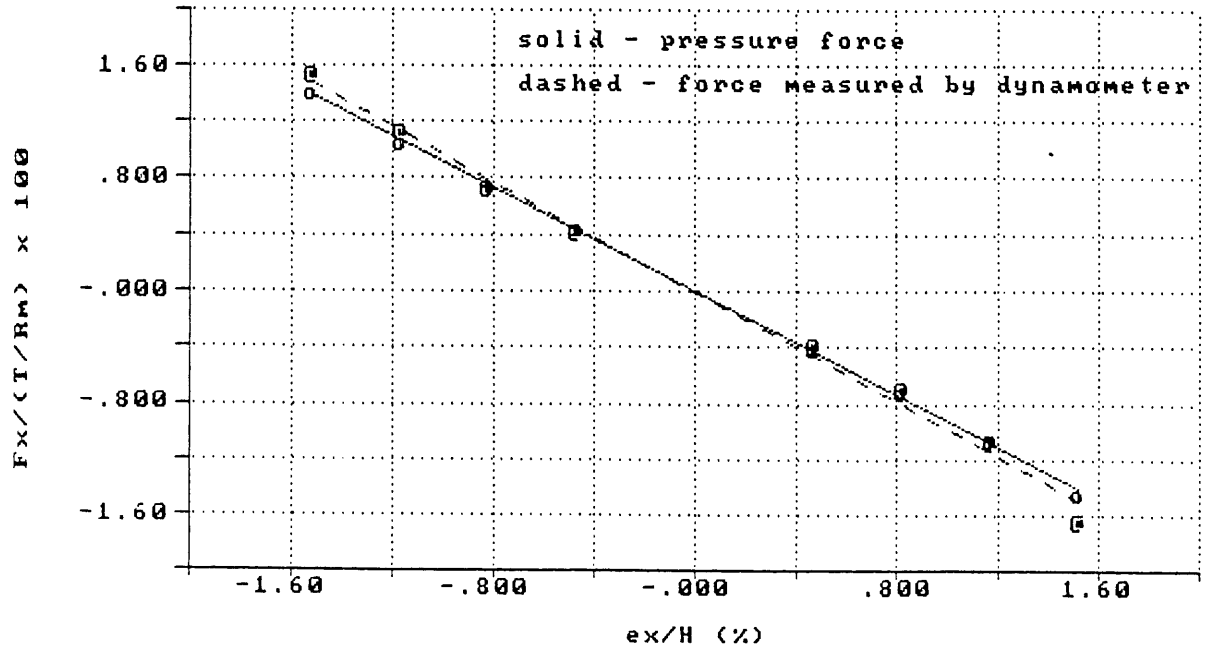

Fig. 5.19 Direct force due to azimuthal static pressure variation vs. eccentricity assuming the pressure acts on the rotor hub area

CHAPTER 6

CONCLUSIONS AND RECOMMENDATIONS

6.1 Conclusions

It was shown that the trend of high power density in modern high performance turbomachines leads to increased problems of rotordynamic instabilities in the form of rotor whirl. The case of the Space Shuttle main engine fuel turbopump instability problem demonstrates this. Several mechanisms which can lead to rotordynamic instabilities were briefly reviewed. A model to predict the effects on stability of lateral rotor displacements was reviewed and it was shown that without sufficient damping cross-coupled forces will cause rotordynamic instabilities.

The work of H. J. Thomas [17] and J. S. Alford [1] on rotor clearance excitation forces was reviewed. Three experimental investigations aimed at quantifying clearance excitation forces was also reviewed and it was shown that in general the data base for this destabilizing mechanism is lacking.

An experimental facility to study turbine blade-tip excitation forces has been designed and constructed. The test section of the facility consists of a single stage turbine which realistically models modern high performance turbomachines. The facility is designed so that the turbine rotor may be laterally offset while the turbine casing remains stationary. Accurate measurement of all force and moment components acting on the rotor is possible through the use of a unique rotating dynamometer. The facility has several other measurement capabilities including detailed flow measurements upstream and downstream of the turbine as well as in the rotor blade-tip region

Various preliminary tests of the facility were successfully completed. A turbine performance map was generated and is presented. The flow velocity at the turbine inlet was measured in order to determine the inlet velocity profile and it is also presented.

The facility was used to measure the forces acting on the rotor due to lateral rotor offset at several operating conditions and the data presented. The linearity of the cross force with both eccentricity and rotor torque, which is predicted by theory, was verified.

The azimuthal pressure distribution at the rotor blade-tips was measured for various rotor eccentricities. It was found to be sinusoidal with the peak pressure occurring near the point of minimum rotor blade-tip clearance.

6.2 Recommendations for Further Work

The experimental measurements presented in this thesis, although significant, just scratch the surface of the measurement capabilities of this facility.

Testing with static rotor offset should continue with more operating conditions tested. The azimuthal efficiency distribution should be measured in order to check the basis of Alford's argument. The effects of stator-to-rotor clearance should be quantified. Finally, Reynolds number effects should also be investigated.

Because actual operating situations of turbomachinery are dynamic, the effects of dynamic rotor offsets should be investigated. Damping is believed to play an important role and this should be quantified.

Finally, a different rotor configuration, such as a shrouded rotor for example, should be tested. Other mechanisms which are less prevalent in an unshrouded rotor configuration, such as azimuthal pressure variations, can become very important when the rotor is shrouded. Testing with a shrouded rotor configuration would enable more detailed study of these.

REFERENCES

[1] Alford, J.S., "Protecting Turbomachinery From Self-Excited Rotor Whirl," Journal of Engineering for Power, Oct. 1965, pp. 333-344.

[2] Benckert, H., and Wachter, J., "Flow-Induced Spring Coefficients of Labyrinth Seals for Application in Rotordynamics," NASA CP 2133, May 1980.

[3] Childs, D., "Rotordynamic Characteristics of the HPOTP (High Pressure Oxygen Turbopump) of the SSME (Space Shuttle Main Engine)," Turbomachinery Laboratories Report under NASA contract NAS8-34505, Texas A&M University, Jan. 30, 1984.

[4] Childs, D. "The Space Shuttle Main Engine High Pressure Fuel Turbopump Instability Problem," ASME Trans. Journal of Engineering for Power, Jan. 1978, pp. 48-57.

[5] Ehrich, F., and Childs, S. D., "Self-Excited Vibrations in High-Performance Turbomachinery," Mechanical Engineering, May 1984, pp. 66-79.

[6] Hartog, J.P., Mechanical Vibrations, 4th ed., McGraw-Hill Book Company, Inc., 1956.

[7] Hill, G., and Peterson, C., Mechanics and Thermodynamics of Propulsion, Addison-Wesley Publishing Company, Inc., 1965, pp.305-307.

[8] Jery, B., "Experimental Study of Unsteady Hydrodynamic Force Matrices on Whirling Centrifugal Pump Impellers," Ph.D. Dissertation, California Institute of Technology, 1987.

[9] Jery, B., Qiu, Y., Martinez-Sanchez, M., and Greitzer, E., "A Facility to Study Turbine Rotor and Seal Clearance Forces," NASA conference publication no. 2436, Advanced Earth-to-Orbit Propulsion Technology, Vol. 1, 1986.

[10] Kimball, A.L., Jr., "Internal Friction Theory of Shaft Whirling," General Electric Review, Vol. 27, April 1924, pp. 244-251.

[11] Martinez-Sanchez, M., and Greitzer, E.M., "Turbine Blade-tip Clearance Excitation Forces," Final Report on NASA contract no. NAS8-35018, June 7, 1985.

[12] Millsaps, K.T., "Analysis of Aero-Elastic Forces in Labyrinth Seals and the Design of an Experimental Facility to Measure Them," S.M. Thesis, Massachusetts Institute of Technology, August, 1986.

[13] Newkirk, B.L., "Shaft Whipping," General Electric Review, Vol. 27, March 1924, pp. 169-178.

[14] Newkirk, B.L., and Taylor, H.D., "Shaft Whipping Due to Oil Action in Journal Bearing, General Electric Review, Vol. 28, 1925, pp. 559-568.

[15] Pollman, E., et. al., "Flow-Excited Vibrations in High Pressure Turbines," Turbomachinery Developments in Steam and Gas Turbines, ASME, Nov.-Dec., 1977.

[16] Qiu, Y., and Martinez-Sanchez, M., "The Prediction of Destabilizing Blade Tip Forces for Shrouded and Unshrouded Turbines," Presented at the Symposium on Instability in Rotating Machinery, June, 1985.

[17] Thomas, H.J., "Unstable Oscillations of Turbine Rotors Due to Steam Leakage in the Clearance of the Sealing Glands and the Buckets," Bulletin Scientifique, A.J.M., Vol. 71, 1958.

[18] Urlichs, K., "Durch Spaltstromungen Hervorgerufene Querkrafte und den Laeufern Thermischer Turbomaschinen," Dissertation, Technical University of Munich, 1975. Translated as NASA TM 77293, "Clearance Flow Generated Traverse Forces at the Rotors of Thermal Turbomachines," Oct., 1983.

[19] Vance, J.M., Rotordynamics of Turbomachinery, John Wiley & Sons, 1988, pp. 22-26.

[20] Vance, J.M., and Laudadio, F.J., "Experimental Measurement of Alford's Force in Axial Flow Turbomachinery," ASME paper 84-GT-140, June, 1984.

[21] Wohlrab, R., Experimentelle Ermittlung Spaltstromungsbedingter Drafte am Turbinenstuffen und Deren Einfluss auf die Laufstablitat Einfacher Rotoren," Dissertation, Technical University of Munich, 1975. Translated as NASA TM 77293, "Experimental Determination of Gap-Flow Conditioned Forces at Turbine Stages, and Their Effect on the Running Stability of Simple Rotors," Oct. 1983.

APPENDIX A

INLET VELOCITY PROFILE

To determine if any inlet distortions are present, the velocity profile of the turbine inlet was measured with a Pitot-static probe. Because inlet distortions could have significant effects on the rotor forces, it is important to determine if any exist. Several flow straighteners are provided upstream from the turbine in an effort to remove any distortions, however it is still necessary to check the flatness of the inlet profile.

The measurements were done at axial station 0 (see instrumentation map, fig. 4.9). The probe was traversed across the inlet in 1.3 cm (0.5 in) increments, except within the first 1.3 cm (0.5 in) of the wall were the traversing was incremented by 0.16 cm (0.06 in). Traversing was done along both the X and Y axis (see fig. 5.3).

The data which were taken was total and static pressure (P_t, P_s) and temperature (T). The velocity at each point was then calculated from the simple relation,

$$V = \sqrt{\frac{2\,(P_t - P_s)}{\rho}}$$

where ρ is the fluid density found from the ideal gas relation,

$$\rho = \frac{P_s}{R\,T}$$

where the gas constant, R, for Freon-12 is 68.76 J/kg K. The average velocity of each traverse was calculated and then used to normalize each point in the traverse. All

measurements were done two times and the results for both trials are plotted in figures A.1 and A.2.

The profile in both directions shows that the flow velocity is increased by at most 10% within the first 5 cm (2 in) near the wall. This is most likely due to the acceleration of the flow as it nears the ogive and enters the turbine flowpath. The Y-axis profile is quite symmetric while the X-axis profile is slightly less symmetric. The non-symmetry of the X-axis profile could be due to rotating flow generated at the 90° bend upstream of the turbine inlet.

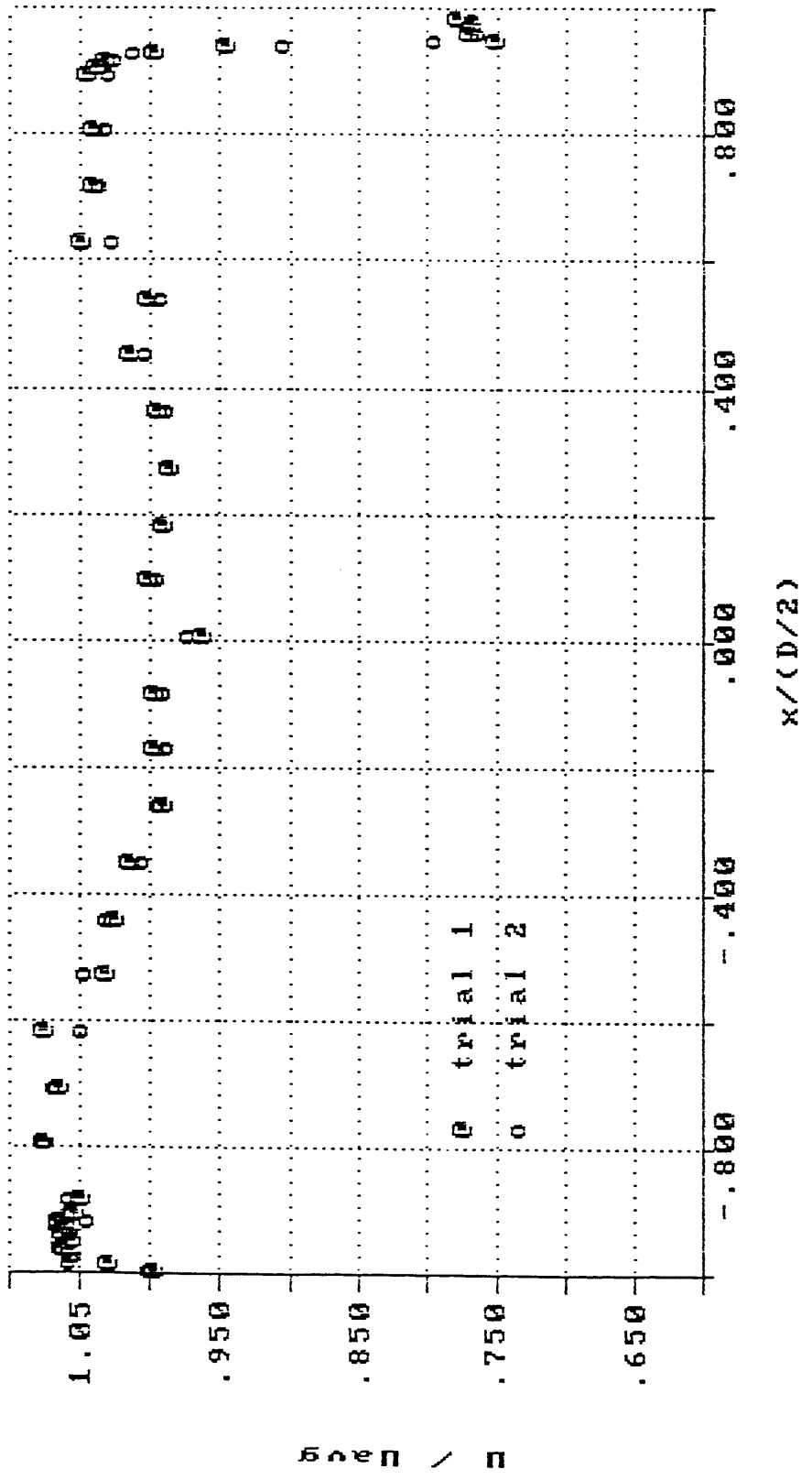

Fig. A.1 Inlet velocity profile, X-axis

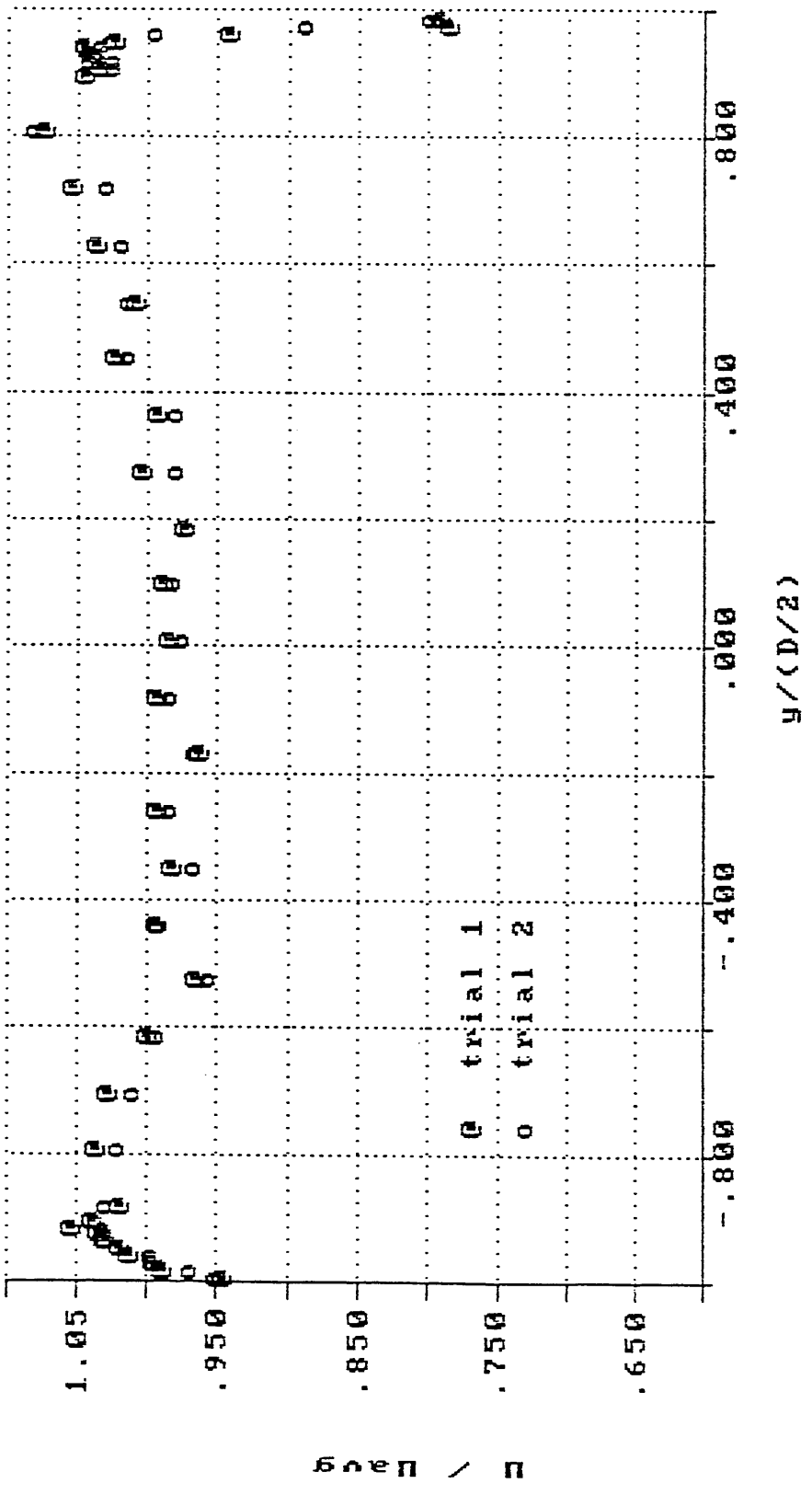

Fig. A.2 Inlet velocity profile, Y-axis

APPENDIX B

TURBINE PERFORMANCE MAP

Flow measurements were made to map the performance of the Alford force test facility turbine. The measurements made were as follows: (i) mass flow by means of a Venturi meter, (ii) inlet total pressure and stage pressure drop with 3-hole pressure probes located at the mean radius at axial instrumentation stations 1 and 8 (see fig. 4.11) and (iii) rotation rate with the optical encoder. Other measurements included station 0 (see fig. 4.11) temperature and rotor torque with the lower torque strain gauge bridge (see fig. 3.5, item 14).

The turbine was run in Freon in its concentric position. Data were taken at 9 to 12 different mass flows at four different speeds; 2200, 2600, 3000 and 3440 rpm. The mass flow was varied by the downstream throttle valve (see fig.3.1) while the rotor speed was held constant by adjusting the DC generator field voltage. The dimensional performance map is shown in figure B.1.

It is desired to non-dimensionalize the performance map so that it is valid at any inlet temperature and pressure. According to the analysis in Hill and Peterson [ ] at sufficiently high Reynolds number, greater than 2×10^5 based on mean velocity and blade chord, the turbine pressure ratio, $P_{t,in}/P_{t,out}$, is a function of two non-dimensional groups only,

$$\frac{P_{t,in}}{P_{t,out}} = f\left(\frac{\dot{m}\sqrt{R\,T_{t,in}}}{P_{t,in}\,D^2}, \frac{\omega_r D}{\sqrt{\gamma R\,T_{t,in}}}\right)$$

where R is the gas constant (R = 68.76 J/kg K for Freon-12), D is a scale factor, ω_r is the rotor speed (in rad/s), γ is the specific heat ratio (γ = 1.12 for Freon-12) and $P_{t,in}$ and $T_{t,in}$ are the inlet total pressure and total temperature, respectively. Because the test turbine operates at

Reynolds no. greater than $2x10^5$ (see discussion in Chapter 3), these non-dimensional groups are valid.

Using the rotor outer diameter for the scale factor D ($D = 2R_o = 28.01$ cm) the performance map was non-dimensionalized and the results are plotted in figure B.2.

The final step in achieving a turbine performance map was to curve-fit the acquired data points. A third-order polynomial curve fit was used and the parameters are as follows,

	$\frac{\omega_r D}{\sqrt{\gamma R T_{t,in}}}$			
COEFFICIENT	0.425	0.502	0.579	0.664
C_0	0.7826	0.6165	0.3413	0.4747
C_1	26.67	41.78	65.91	50.84
C_2	-961.1	-1404	-2114	-1595
C_3	14560	18980	26270	20920
R^2	0.9995	0.9998	0.9995	0.9997

where R^2 is the correlation coefficient. The curve-fit turbine performance map is shown in figure B.3.

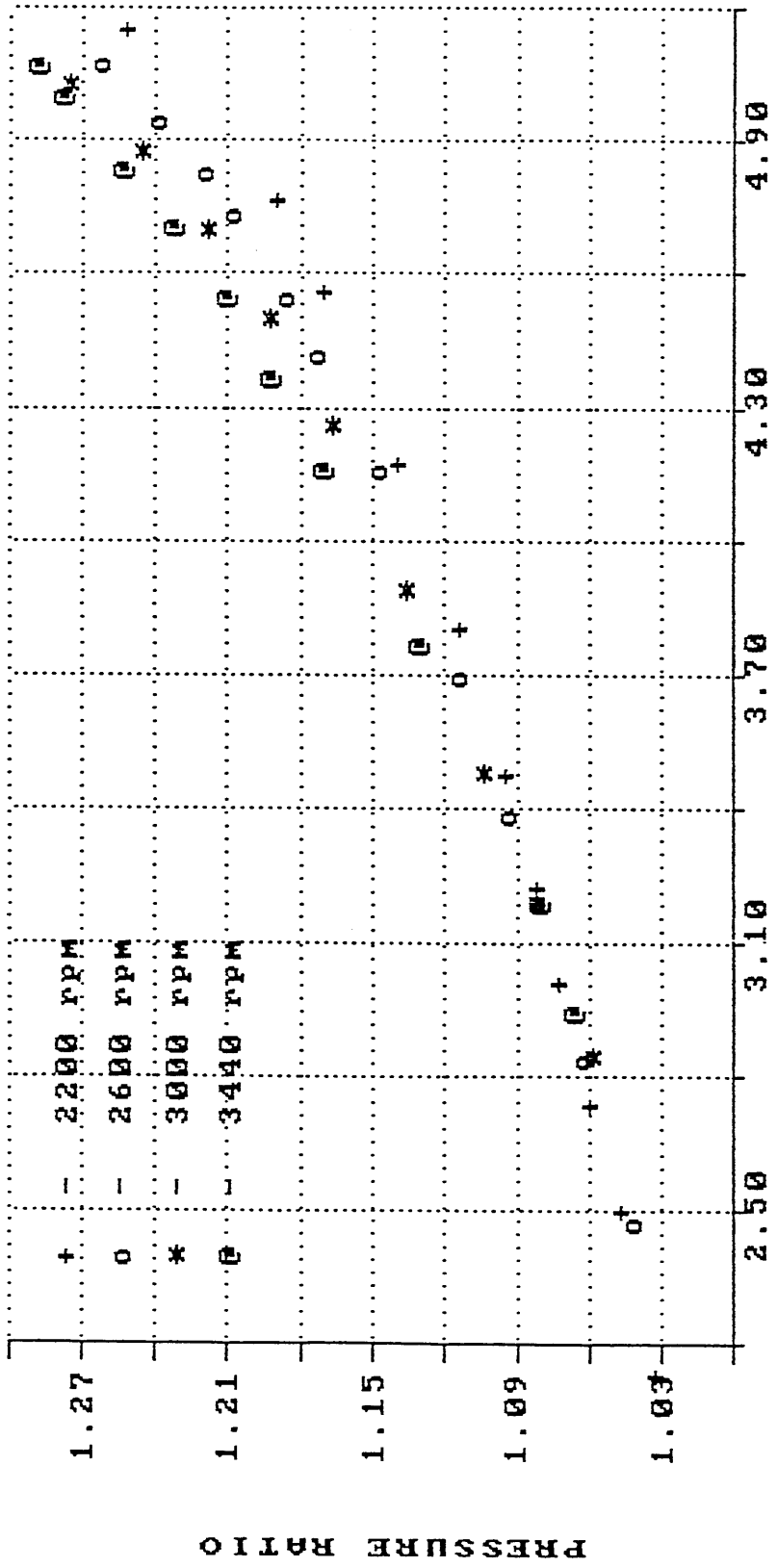

Fig. B.1 Alford force test facility test turbine dimensional performance map

$P_{t,\,inlet}$ = 224 kPa (32.5 psia), $T_{t,\,inlet}$ = 300 K (79° F)

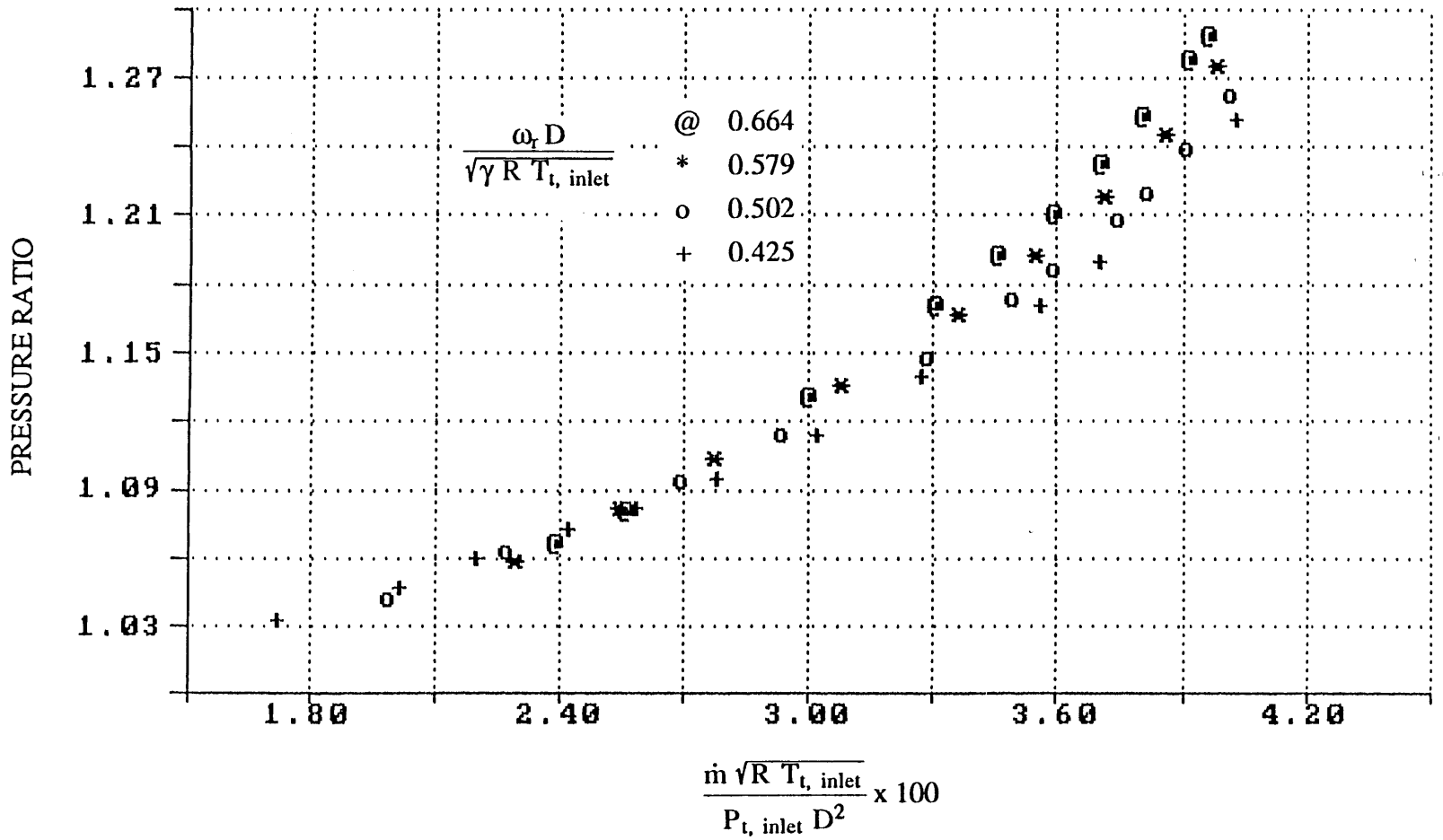

Fig. B.2 Alford force test facility test turbine non-dimensional performance map

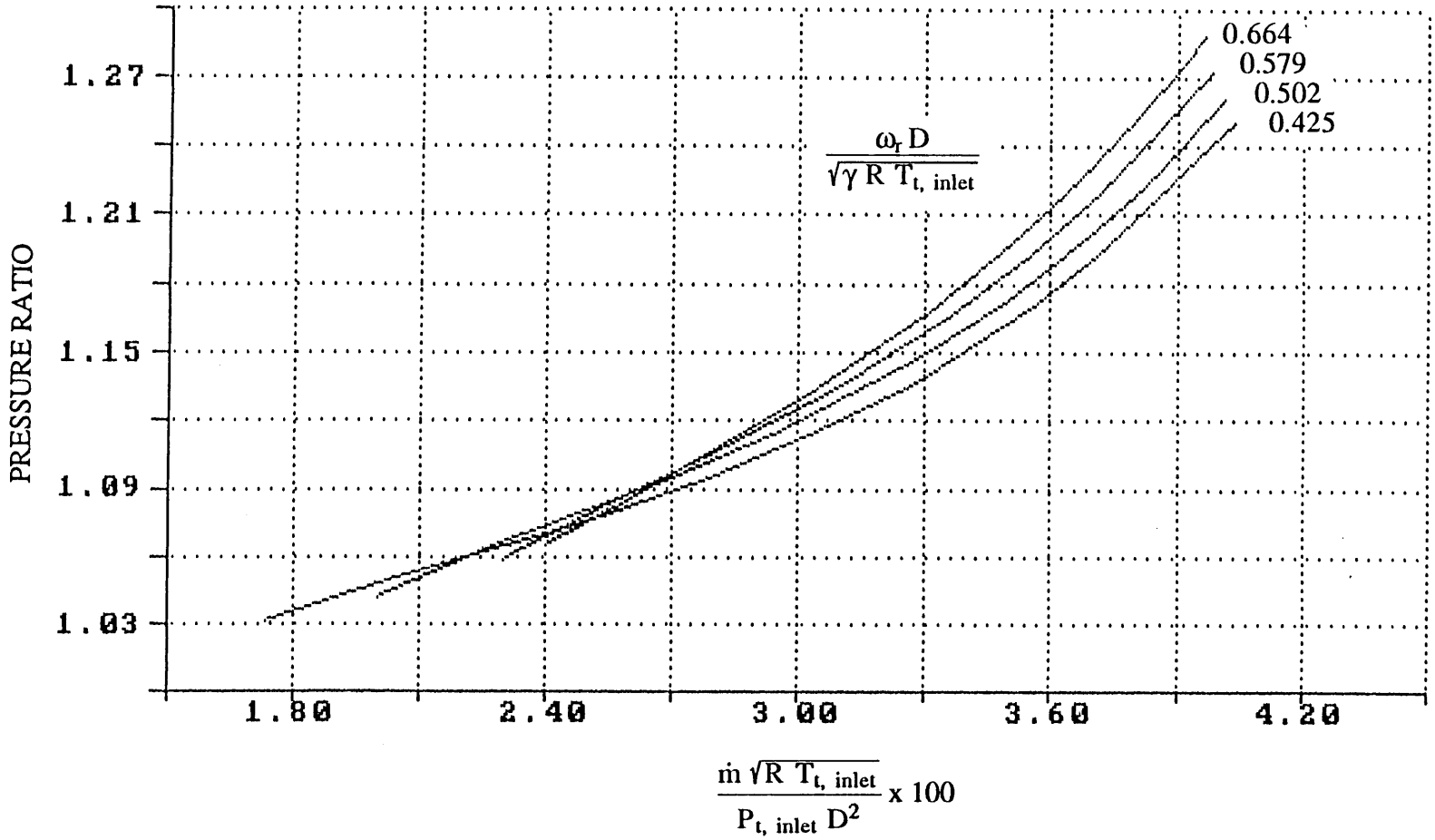

Fig. B.3 Alford force test facility turbine performance map

APPENDIX C

DATA TABLES

Table C.1 Lateral force data at different eccentricities, 3 trials

Rotor Speed - 2200 rpm

Mass Flow - 4.73 kg/s (0.324 slug/s)

Rotor Torque - 70.2 Nm (621 in lb)

Stage Pressure Ratio - 1.213

ECCENTRICITY, mm (mils)	CROSS FORCE, N (lbf)	DIRECT FORCE, N (lbf)	RESULTANT, N (lbf), O
+0.33 (+13.0)	8.37 (1.88)	-8.23 (-1.85)	11.7 (2.64), 134.6
	8.37 (1.88)	-8.28 (-1.86)	11.7 (2.64), 134.7
	8.32 (1.87)	-8.28 (-1.86)	11.7 (2.64), 134.8
+0.25 (+10.0)	6.81 (1.53)	-6.45 (-1.45)	9.39 (2.11), 133.4
	6.81 (1.53)	-6.41 (-1.44)	9.35 (2.10), 133.2
	6.81 (1.53)	-6.41 (-1.44)	9.35 (2.10), 133.2
+0.18 (+7.0)	5.12 (1.15)	-4.36 (-0.98)	6.72 (1.51), 130.5
	5.16 (1.16)	-4.41 (-0.99)	6.76 (1.52), 130.4
	5.12 (1.15)	-4.41 (-0.99)	6.76 (1.52), 130.6
+0.10 (+4.0)	3.65 (0.82)	-2.71 (-0.61)	4.54 (1.02), 126.8
	3.60 (0.81)	-2.67 (-0.60)	4.49 (1.01), 126.4
	3.60 (0.81)	-2.67 (-0.60)	4.49 (1.01), 126.7
0.00 (0.0)	1.42 (0.32)	-0.76 (-0.17)	1.65 (0.37), 118.0
	1.51 (0.34)	-0.80 (-0.18)	1.69 (0.38), 117.6
	1.47 (0.33)	-0.76 (-0.17)	1.65 (0.37), 117.6
-0.10 (-4.0)	-0.67 (-0.15)	1.20 (0.27)	1.38 (0.31), -27.9
	-0.62 (-0.14)	1.25 (0.28)	1.38 (0.31), -26.8
	-0.62 (-0.14)	1.25 (0.28)	1.38 (0.31), -27.0
-0.18 (-7.0)	-2.23 (-0.50)	2.58 (0.58)	3.43 (0.77), -40.9
	-2.23 (-0.50)	2.63 (0.59)	3.43 (0.77), -40.4
	-2.23 (-0.50)	2.63 (0.59)	3.43 (0.77), -40.3
-0.25 (-10.0)	-3.92 (-0.88)	4.32 (0.97)	5.83 (1.31), -42.2
	-3.92 (-0.88)	4.23 (0.95)	5.79 (1.30), -42.9
	-4.01 (-0.90)	4.32 (0.97)	5.87 (1.32), -42.7
-0.33 (-13.0)	-5.61 (-1.26)	6.32 (1.42)	8.46 (1.90), -41.7
	-5.70 (-1.28)	6.36 (1.43)	8.54 (1.92), -41.8
	-5.61 (-1.26)	6.32 (1.42)	8.46 (1.90), -41.7

Table C.2 Lateral force data at different eccentricities, 3 trials

Concentric turbine values subtracted

Rotor Speed - 2600 rpm
Mass Flow - 4.70 kg/s (0.322 slug/s)
Rotor Torque - 65.1 Nm (576 in lb)
Stage Pressure Ratio - 1.226

ECCENTRICITY, mm (mils)	CROSS FORCE, N (lbf)	DIRECT FORCE, N (lbf)	RESULTANT, N (lbf), O)
+0.33 (+13.0)	6.90 (1.55)	-7.48 (-1.68)	10.2 (2.29), 137.3
	6.85 (1.54)	-7.48 (-1.68)	10.1 (2.28), 137.5
	6.90 (1.55)	-7.52 (-1.69)	10.2 (2.29), 137.5
+0.25 (+10.0)	5.38 (1.21)	-5.70 (-1.28)	7.83 (1.76), 136.6
	5.30 (1.19)	-5.61 (-1.26)	7.70 (1.73), 136.6
	5.34 (1.20)	-5.65 (-1.27)	7.79 (1.75), 136.6
+0.18 (+7.0)	3.65 (0.82)	-3.60 (-0.81)	5.12 (1.15), 134.6
	3.65 (0.82)	-3.60 (-0.81)	5.12 (1.15), 134.6
	3.69 (0.83)	-3.65 (-0.82)	5.21 (1.17), 134.7
+0.10 (+4.0)	2.18 (0.49)	-1.96 (-0.44)	2.94 (0.66), 131.9
	2.14 (0.48)	-1.87 (-0.42)	2.85 (0.64), 131.2
	2.14 (0.48)	-1.91 (-0.43)	2.85 (0.64), 131.9
-0.10 (-4.0)	-2.09 (-0.47)	2.00 (0.45)	2.89 (0.65), -46.2
	-2.14 (-0.48)	2.00 (0.45)	2.94 (0.66), -46.8
	-2.09 (-0.47)	2.00 (0.45)	2.89 (0.65), -46.2
-0.18 (-7.0)	-3.69 (-0.83)	3.38 (0.76)	5.03 (1.13), -47.5
	-3.74 (-0.84)	3.38 (0.76)	5.03 (1.13), -47.9
	-3.69 (-0.83)	3.38 (0.76)	5.03 (1.13), -47.5
-0.25 (-10.0)	-5.38 (-1.21)	5.07 (1.14)	7.39 (1.66), -46.7
	-5.43 (-1.22)	5.03 (1.13)	7.39 (1.66), -47.2
	-5.43 (-1.22)	5.07 (1.14)	7.43 (1.67), -46.9
-0.33 (-13.0)	-7.08 (-1.59)	7.08 (1.59)	10.0 (2.25), -45.0
	-7.21 (-1.62)	7.16 (1.61)	10.1 (2.28), -45.2
	-7.08 (-1.59)	7.08 (1.59)	10.0 (2.25), -45.0

Table C.3 Lateral force data at different eccentricities

Rotor Speed - 2200 rpm
Mass Flow - 4.73 kg/s (0.324 slug/s)
Rotor Torque - 70.2 Nm (621 in lb)
Stage Pressure Ratio - 1.213

ECCENTRICITY, mm (mils)	CROSS FORCE, N (lbf)	DIRECT FORCE, N (lbf)	RESULTANT, N (lbf), O
+0.33 (+13.0)	8.10 (1.82)	-7.61 (-1.71)	11.1 (2.50), 133.2
+0.25 (+10.0)	6.85 (1.54)	-5.30 (-1.19)	8.68 (1.95), 127.6
+0.18 (+7.0)	5.43 (1.22)	-3.52 (-0.79)	6.50 (1.46), 123.1
+0.10 (+4.0)	4.18 (0.94)	-2.23 (-0.50)	4.72 (1.06), 117.8
0.00 (0.0)	1.96 (0.44)	-0.40 (-0.09)	2.00 (0.45), 101.3
-0.10 (-4.0)	0.18 (0.04)	0.71 (0.16)	0.76 (0.17), 14.2
-0.18 (-7.0)	-1.25 (-0.28)	2.00 (0.45)	2.36 (0.53), -31.8
-0.25 (-10.0)	-2.67 (-0.60)	3.47 (0.78)	4.41 (0.99), -37.5
-0.33 (-13.0)	-4.27 (-0.96)	5.25 (1.18)	6.76 (1.52), -39.1

Table C.4 Lateral force data at different eccentricities

Rotor Speed - 2600 rpm
Mass Flow - 4.70 kg/s (0.322 slug/s)
Rotor Torque - 65.1 Nm (576 in lb)
Stage Pressure Ratio - 1.226

ECCENTRICITY, mm (mils)	CROSS FORCE, N (lbf)	DIRECT FORCE, N (lbf)	RESULTANT, N (lbf), O
+0.33 (+13.0)	9.03 (2.03)	-7.66 (-1.70)	11.8 (2.65), 130.0
+0.25 (+10.0)	7.39 (1.66)	-5.21 (-1.17)	9.03 (2.03), 125.2
+0.18 (+7.0)	5.87 (1.32)	-3.52 (-0.79)	6.85 (1.54), 121.0
+0.10 (+4.0)	4.45 (1.00)	-2.27 (-0.51)	4.98 (1.12), 116.8
0.00 (0.0)	2.18 (0.49)	-0.58 (-0.13)	2.27 (0.51), 105.0
-0.10 (-4.0)	0.18 (0.04)	0.62 (0.14)	0.62 (0.14), 17.3
-0.18 (-7.0)	-1.38 (-0.31)	1.78 (0.40)	2.27 (0.51), -37.4
-0.25 (-10.0)	-2.94 9-0.66)	3.38 (0.76)	4.49 (1.01), -41.0
-0.33 (-13.0)	-4.85 (-1.09)	5.30 (1.19)	7.21 (1.62), -42.5

Table C.5 Lateral force data at different eccentricities

Rotor Speed - 3000 rpm
Mass Flow - 4.65 kg/s (0.319 slug/s)
Rotor Torque - 59.8 Nm (529 in lb)
Stage Pressure Ratio - 1.234

ECCENTRICITY, mm (mils)	CROSS FORCE, N (lbf)	DIRECT FORCE, N (lbf)	RESULTANT, N (lbf), O
+0.33 (+13.0)	7.83 (1.76)	-7.74 (-1.74)	11.0 (2.48), 134.6
+0.25 (+10.0)	6.32 91.42)	-5.43 (-1.22)	8.32 (1.87), 130.7
+0.18 (+7.0)	4.85 (1.09)	-3.78 (-0.85)	6.14 (1.38), 127.8
+0.10 (+4.0)	3.52 90.79)	-2.49 (-0.56)	4.32 (0.97), 125.0
0.00 (0.0)	1.47 (0.33)	-0.80 (-0.18)	1.69 (0.38), 118.8
-0.10 (-4.0)	-0.49 (-0.11)	0.71 (0.16)	0.85 (0.19), -34.0
-0.18 (-7.0)	-2.00 (-0.45)	2.14 (0.48)	2.94 (0.66), -42.8
-0.25 (-10.0)	-3.56 (-0.80)	3.69 (0.83)	5.12 (1.15), -43.7
-0.33 (-13.0)	-5.34 (-1.20)	5.56 (1.25)	7.70 (1.73), -43.9

Table C.6 Lateral force data at different eccentricities

Rotor Speed - 3440 rpm
Mass Flow - 4.62 kg/s (0.317 slug/s)
Rotor Torque - 53.9 Nm (477 in lb)
Stage Pressure Ratio - 1.244

ECCENTRICITY, mm (mils)	CROSS FORCE, N (lbf)	DIRECT FORCE, N (lbf)	RESULTANT, N (lbf), O
+0.33 (+13.0)	7.79 (1.75)	-7.30 (-1.64)	10.7 (2.40), 133.1
+0.25 (+10.0)	6.32 (1.42)	-4.94 (-1.11)	8.01 (1.80), 128.2
+0.18 (+7.0)	4.98 (1.12)	-3.34 (-0.75)	6.01 (1.35), 123.9
+0.10 (+4.0)	3.74 (0.84)	-2.09 (-0.47)	4.27 (0.96), 119.1
0.00 (0.0)	1.87 (0.42)	-0.40 (-0.09)	1.91 (0.43), 102.2
-0.10 (-4.0)	-0.04 (-0.01)	1.29 (0.29)	1.29 (0.29), -2.7
-0.18 (-7.0)	-1.47 (-0.33)	2.63 (0.59)	3.03 (0.68), -28.9
-0.25 (-10.0)	-2.85 (-0.64)	4.27 (0.96)	5.12 (1.15), -33.9
-0.33 (-13.0)	-4.45 (-1.00)	6.01 (1.35)	7.43 (1.67), -36.5

Table C.7 Lateral force data at different eccentricities

Concentric turbine values subtracted

Rotor Speed - 2200 rpm
Mass Flow - 4.73 kg/s (0.324 slug/s)
Rotor Torque - 70.2 Nm (621 in lb)
Stage Pressure Ratio - 1.213

ECCENTRICITY, mm (mils)	CROSS FORCE, N (lbf)	DIRECT FORCE, N (lbf)	RESULTANT, N (lbf), O
+0.33 (+13.0)	6.14 (1.38)	-7.21 (-1.62)	9.48 (2.13), 139.6
+0.25 (+10.0)	4.90 (1.10)	-4.90 (-1.10)	6.94 (1.56), 135.0
+0.18 (+7.0)	3.47 (0.78)	-3.12 (-0.70)	4.12 (1.06), 132.2
+0.10 (+4.0)	2.23 (0.50)	-1.82 (-0.41)	2.85 (0.64), 129.3
-0.10 (-4.0)	-1.78 (-0.40)	1.11 (0.25)	2.09 (0.47), -57.7
-0.18 (-7.0)	-3.20 (-0.72)	2.40 (0.54)	4.01 (0.90), -53.2
-0.25 (-10.0)	-4.63 (-1.04)	3.87 (0.87)	6.05 (1.36), -50.1
-0.33 (-13.0)	-6.23 (-1.40)	5.65 (1.27)	8.41 (1.89), -47.8

Table C.8 Lateral force data at different eccentricities

Concentric turbine values subtracted

Rotor Speed - 2600 rpm
Mass Flow - 4.70 kg/s (0.322 slug/s)
Rotor Torque - 65.1 Nm (576 in lb)
Stage Pressure Ratio - 1.226

ECCENTRICITY, mm (mils)	CROSS FORCE, N (lbf)	DIRECT FORCE, N (lbf)	RESULTANT, N (lbf), O
+0.33 (+13.0)	6.85 (1.54)	-6.99 (-1.57)	9.79 (2.20), 135.6
+0.25 (+10.0)	5.21 (1.17)	-4.63 (-1.04)	6.94 (1.56), 131.7
+0.18 (+7.0)	3.69 (0.83)	-2.94 (-0.66)	4.72 (1.06), 128.6
+0.10 (+4.0)	2.27 (0.51)	-1.69 (-0.38)	2.80 (0.63), 126.3
-0.10 (-4.0)	-2.00 (-0.45)	1.20 (0.27)	2.31 (0.52), -59.5
-0.18 (-7.0)	-3.56 (-0.80)	2.36 (0.53)	4.32 (0.97), -56.2
-0.25 (-10.0)	-5.12 (-1.15)	3.96 (0.89)	6.50 (1.46), -52.3
-0.33 (-13.0)	-7.03 (-1.58)	5.87 (1.32)	9.21 (2.07), -50.1

Table C.9 Lateral force data at different eccentricities

Concentric turbine values subtracted

Rotor Speed - 3000 rpm
Mass Flow - 4.65 kg/s (0.319 slug/s)
Rotor Torque - 59.8 Nm (529 in lb)
Stage Pressure Ratio - 1.234

ECCENTRICITY, mm (mils)	CROSS FORCE, N (lbf)	DIRECT FORCE, N (lbf)	RESULTANT, N (lbf), O
+0.33 (+13.0)	6.36 (1.43)	-6.94 (-1.56)	9.43 (2.12), 137.4
+0.25 (+10.0)	4.85 (1.09)	-4.63 (-1.04)	6.68 (1.50), 133.7
+0.18 (+7.0)	3.38 (0.76)	-2.98 (-0.67)	4.49 (1.01), 131.2
+0.10 (+4.0)	2.05 (0.46)	-4.67 (-0.38)	2.63 (0.59), 129.0
-0.10 (-4.0)	-1.96 (-0.44)	1.51 (0.34)	2.49 (0.56), -52.2
-0.18 (-7.0)	-3.47 (-0.78)	2.94 (0.66)	4.58 (1.03), -49.5
-0.25 (-10.0)	-5.03 (-1.13)	4.49 (1.01)	6.76 (1.52), -48.0
-0.33 (-13.0)	-6.81 (-1.53)	6.36 (1.43)	9.35 (2.10), -47.0

Table C.10 Lateral force data at different eccentricities

Concentric turbine values subtracted

Rotor Speed - 3440 rpm
Mass Flow - 4.62 kg/s (0.317 slug/s)
Rotor Torque - 53.9 Nm (477 in lb)
Stage Pressure Ratio - 1.244

ECCENTRICITY, mm (mils)	CROSS FORCE, N (lbf)	DIRECT FORCE, N (lbf)	RESULTANT, N (lbf), O
+0.33 (+13.0)	5.92 (1.33)	-6.90 (-1.55)	9.08 (2.04), 139.3
+0.25 (+10.0)	4.45 (1.00)	-4.54 (-1.02)	6.36 (1.43), 135.8
+0.18 (+7.0)	3.12 (0.70)	-2.94 (-0.66)	4.27 (0.96), 133.4
+0.10 (+4.0)	1.87 (0.42)	-1.69 (-0.38)	2.49 (0.56), 131.9
-0.10 (-4.0)	-1.91 (-0.43)	1.69 (0.38)	2.58 (0.58), -48.8
-0.18 (-7.0)	-3.34 (-0.75)	3.03 (0.68)	4.54 (1.02), -47.5
-0.25 (-10.0)	-4.72 (-1.06)	4.67 (1.05)	6.63 (1.49), -45.4
-0.33 (-13.0)	-6.32 (-1.42)	6.41 (1.44)	8.94 (2.01), -44.6

Table C.11 Cross force data at different rotor torques

Rotor Speed - 3440 rpm

All cross force values in N (lbf)

TORQUE, N m (in lb)	ECCENTRICITY, mm (mils) 0.00 (0.0)	+0.18 (+7.0)	+0.33 (+13.0)
60.2 (533)	1.91 (0.43)	5.56 (1.25)	8.86 (1.99)
51.2 (453)	1.42 (0.32)	4.49 (1.01)	7.16 (1.61)
44.5 (394)	1.11 (0.25)	3.74 (0.84)	6.23 (1.40)
37.1 (328)	0.93 (0.21)	3.34 (0.75)	5.43 (1.22)
30.2 (267)	0.67 (0.15)	2.76 (0.62)	4.58 (1.03)
24.1 (213)	0.62 (0.14)	2.36 (0.53)	4.01 (0.90)
17.3 (153)	0.40 (0.09)	1.82 (0.41)	2.00 (0.45)
10.0 (88.5)	0.67 (0.15)	1.07 (0.24)	1.69 (0.38)
5.1 (44.7)	0.53 (0.12)	0.53 (0.12)	0.49 (0.11)

Table C.12 Direct force data at different rotor torques

Rotor Speed - 3440 rpm

All direct force values in N (lbf)

TORQUE, N m (in lb)	ECCENTRICITY, mm (mils) 0.00 (0.0)	+0.18 (+7.0)	+0.33 (+13.0)
60.2 (533)	-0.22 (-0.05)	-3.65 (-0.82)	-8.23 (-1.85)
51.2 (453)	0.00 (0.00)	-2.98 (-0.67)	-6.99 (-1.57)
44.5 (394)	0.00 (0.00)	-2.67 (-0.60)	-5.65 (-1.27)
37.1 (328)	-0.04 (-0.01)	-2.49 (-0.56)	-5.21 (-1.17)
30.2 (267)	-0.18 (-0.04)	-2.40 (-0.54)	-4.67 (-1.05)
24.1 (213)	-0.04 (-0.01)	-2.05 (-0.46)	-4.09 (-0.92)
17.3 (153)	0.27 (0.06)	-1.42 (-0.32)	-2.31 (-0.52)
10.0 (88.5)	0.89 (0.20)	-0.22 (-0.05)	-1.74 (-0.39)
5.1 (44.7)	0.45 (0.10)	-0.67 (-0.15)	-1.56 (-0.35)

Table C.13 Cross force data at different rotor torques

Concentric turbine values subtracted

Rotor Speed - 3440 rpm

All cross force values in N (lbf)

TORQUE N m (in lb)	ECCENTRICITY mm (mils) +0.18 (+7.0)	+0.33 (+13.0)
60.2 (533)	3.65 (0.82)	6.94 (1.56)
51.2 (453)	3.07 (0.69)	5.74 (1.29)
44.5 (394)	2.63 (0.59)	5.12 (1.15)
37.1 (328)	2.40 (0.54)	4.49 (1.01)
30.2 (267)	2.09 (0.47)	3.92 (0.88)
24.1 (213)	1.74 (0.39)	3.38 (0.76)
17.3 (153)	1.42 (0.32)	1.60 (0.36)
10.0 (88.5)	0.40 (0.09)	1.02 (0.23)
5.1 (44.7)	0.00 (0.00)	-0.04 (-0.01)

Table C.14 Direct force data at different rotor torques

Concentric turbine values subtracted

Rotor Speed - 3440 rpm

All direct force values in N (lbf)

TORQUE N m (in lb)	ECCENTRICITY mm (mils) +0.18 (+7.0)	+0.33 (+13.0)
60.2 (533)	-3.43 (-0.77)	-8.01 (-1.80)
51.2 (453)	-2.98 (-0.67)	-6.99 (-1.57)
44.5 (394)	-2.67 (-0.60)	-5.65 (-1.27)
37.1 (328)	-2.45 (-0.55)	-5.16 (-1.16)
30.2 (267)	-2.23 (-0.50)	-4.49 (-1.01)
24.1 (213)	-2.00 (-0.45)	-4.05 (-0.91)
17.3 (153)	-1.69 (-0.38)	-2.58 (-0.58)
10.0 (88.5)	-1.11 (-0.25)	-2.63 (-0.59)
5.1 (44.7)	-1.11 (-0.25)	-2.00 (-0.45)

Table C.15 Calculated rotor cross force due to azimuthal static pressure variation

Concentric turbine values subtracted

Rotor speed - 3440 rpm
Mass flow - 4.72 kg/s (0.323 slug/s)
Rotor torque - 57.6 Nm (510 in lb)
Stage pressure ratio - 1.264

All force values in N (lbf)

ECCENTRICITY mm (mils)	AXIAL LOCATION 1	2	3	TOTAL FORCE
+0.33 (+13.0)	0.74 (0.166)	0.52 (0.116)	1.10 (0.248)	2.36 (0.530)
+0.25 (+10.0)	0.56 (0.126)	0.39 (0.087)	0.82 (0.185)	1.77 (0.398)
+0.18 (+7.0)	0.41 (0.093)	0.27 (0.061)	0.61 (0.137)	1.29 (0.291)
+0.10 (+4.0)	0.21 (0.047)	0.17 (0.039)	0.37 (0.083)	0.75 (0.169)
-0.10 (-4.0)	-0.29 (-0.065)	-0.20 (-0.044)	-0.42 9-0.094)	-0.90 (-0.203)
-0.18 (-7.0)	-0.46 (-0.103)	-0.32 9-0.072)	-0.70 (-0.157)	-1.47 (-0.332)
-0.25 (-10.0)	-0.66 (-0.148)	-0.45 (-0.101)	-0.93 (-0.210)	-2.04 (-0.459)
-0.33 (-13.0)	-0.83 (-0.187)	-0.59 (-0.133)	-1.23 (-0.277)	-2.66 (-0.597)

Table C.16 Calculated rotor direct force due to azimuthal static pressure variation

Concentric turbine values subtracted

Rotor speed - 3440 rpm
Mass flow - 4.72 kg/s (0.323 slug/s)
Rotor torque - 57.6 Nm (510 in lb)
Stage pressure ratio - 1.264

All values in N (lbf)

ECCENTRICITY mm (mils)	AXIAL LOCATION 1	2	3	TOTAL FORCE
+0.33 (+13.0)	-1.75 (-0.394)	-1.55 (-0.349)	-3.15 (-0.707)	-6.45 (-1.450)
+0.25 (+10.0)	-1.33 (-0.299)	-1.17 (-0.262)	-2.31 (-0.519)	-4.81 (-1.080)
+0.18 (+7.0)	-0.92 (-0.206)	-0.78 (-0.176)	-1.55 (-0.349)	-3.25 (-0.731)
+0.10 (+4.0)	-0.57 (-0.128)	-0.46 (-0.103)	-0.86 (-0.193)	-1.89 (-0.424)
-0.10 (-4.0)	0.60 (0.135)	0.49 (0.111)	0.91 (0.205)	2.01 (0.451)
-0.18 (-7.0)	0.99 (0.222)	0.81 (0.182)	1.45 (0.325)	3.24 (0.729)
-0.25 (-10.0)	1.40 (0.315)	1.14 (0.256)	2.14 (0.481)	4.68 (1.052)
-0.33 (-13.0)	1.82 (0.409)	1.53 (0.344)	2.94 (0.660)	6.29 (1.413)